Imaging Biomolecules using Frequency Modulation Atomic Force Microscopy in Liquids

Zermina Khan

University College London

London Centre for Nanotechnology

Department of Physics and Astronomy

A thesis submitted in partial fulfillment for the degree of

Doctor of Philosophy

in Physics/Nanotechnology

I, Zermina Khan confirm that the work presented in this thesis is my own. Where information has been derived from other sources, I confirm that this has been indicated in the thesis.

Zermina Khan

December 2012

Abstract

Atomic force microscopy is an advanced imaging technique for viewing biological structures and dynamic biological mechanisms at the nanometre scale. This thesis describes a high-resolution atomic force microscope designed for imaging biological samples in physiological solution. This microscope includes a highly sensitive interferometric cantilever detector, along with a home-built frequency/phase and amplitude detector. The initial chapters of this thesis begin with a description of the experimental set-up, as well as various tests carried out to characterise the fast frequency detector. Following this is a description of the interferometric cantilever detector, which possess a noise floor at a mere 5 fm/$\sqrt{\text{Hz}}$, making it particularly suited for detecting cantilevers in liquids. Results chapters then go on to demonstrate the capability of this instrument to image at nanometre and atomic-scale resolution. Images of the atomic structure of muscovite mica in buffer solution are presented. Images of chaperonin protein GroEL were also acquired, which contain features of the protein's apical domain. Most importantly, for the first time AFM was used to track the pore-formation of pore forming protein pneumolysin in buffer solution. Supported lipid bilayers were prepared and images were captured of the proteins oligomerising on their surface. The initial stage of pore-formation was investigated by comparing the height of pneumolysin before and after pores were formed. Details of the monomers making up the structure of the protein were also imaged, as well as pores created within the supported lipid bilayers.

Dedicated to my parents, husband and my angel Ayza.

"Energy and persistence conquer all things"

- Benjamin Franklin

Acknowledgements

First and foremost, I would like to express my sincere gratitude to my supervisor Dr Bart Hoogenboom for his generous support throughout the course of my research. I'd like to thank him for his patience, motivation and useful discussions without which I could not have gained such a fruitful understanding of this most exciting area of research. I would like to acknowledge Helen Saibil's group and in particular Natasha Lukoyanova at Birkbeck University for providing us with the biological samples required for the experimental work described in this thesis. I wish to express gratitude to Laurent Bozec, Carl Leung and Nitya Gosvami for their kind help and guidance. Also, I would like to say thank you to Benjamin Bircher, Bilal Tahir for their contribution to the atomic force microscope set-up and I wish to recognise the kindness and support from my group members Rosie Paxman and Alice Pyne. I would also like to convey my appreciation to Richard Thorogate for always being so helpful in the laboratory. I thank the administration staff from the London Centre for Nanotechnology and the Department of Physics and Astronomy at UCL for all their help and hard work. I would like to acknowledge the funding received from the EPSRC. I would like to thank my husband for his support and great patience at all times and my parents for taking care of my baby Ayza so that I could complete this work. I am indebted to my wonderful family and friends for their unconditional support and encouragement.

Publications

Z. Khan, C. Leung, B. A Tahir, and B. W. Hoogenboom. (2010). Digitally tunable, wide-band amplitude, phase and frequency detection for atomic-resolution scanning force microscopy. Rev. Sci. Instrum. 81, 073704.

R. R. Gruter, Z. Khan, R. Paxman, J. W. Ndieyira, B. Dueck, B. A. Bircher, J. L. Yang, U. Drechsler, M. Despont, R. A. McKendry and B. W. Hoogenboom. (2010) Disentangling mechanical and mass effects on nanomechanical resonators. Applied Physics Letters. 96, 023113.

Contents

List of Figures

Part I.

Introduction and Experimental Methods

1. Introduction

1.1. Context of thesis

Intricate biomolecular machinery underlies life, along with how diseases and cures for diseases work. These mechanisms can be studied at nanoscale resolution using methods such as electron microscopy, X-ray crystallography or nuclear magnetic resonance imaging. However, these techniques are not able to visualise dynamic biological processes in action. Atomic force microscopy (AFM) is a versatile instrument that allows biomolecules to be imaged in physiological solution. To acquire an image, AFM uses a sharp tip on the end of cantilever to trace the contours of the sample surface. It is critical to image at sufficient force to achieve contrast but not distort the sample. Hence, obtaining nanometre and sub-nanometre resolution of delicate biomolecules in liquid requires sophisticated instrumentation.

This thesis describes a frequency modulation atomic force microscopy (FM AFM) developed and optimised for high resolution imaging in liquids. This FM AFM includes a highly sensitive interferometric cantilever detector, capable of detecting sub-nanometre oscillations of reduced dimension cantilevers. The aim of this research was to use this imaging technique to provide a detailed visualisation of the structures of operating biomolecules in liquids. The initial chapters begin with a description of the electronic components of our FM AFM. Following this is a description of tests carried out to characterise the bandwidth of frequency and phase detection and the step response of the frequency detector. Results chapters are then presented which consist of the images acquired by the FM AFM on various surfaces. The first set of results are atomic resolution images of muscovite

mica's crystal lattice in buffer solution. Next, images of a model biological sample named chaperonin GroEL are presented, which include details of its surface structure. Next, for the first time AFM was used to image the pore-formation process of a pore forming protein named pneumolysin on supported lipid bilayers (SLB). This final results chapter includes a description of the protocol used to create SLBs onto which the proteins could adsorb. Images of the pneumolysin oligomerising and forming pores on SLBs are presented, alongside a description of salient features.

2. Atomic force microscopy for imaging biomolecules in liquids

2.1. Introduction

Atomic force microscopy (AFM) is versatile instrument with the ability to assess the surface topography of a sample at sub-nanometre resolution. For example, the surface of polymers, fibres, metals, minerals or ceramics can be imaged to assess surface roughness or for structural analysis. AFM can also be used to image biological samples such as cells, nucleic acids, proteins or lipids. More importantly, these biomolecular structures can be imaged whilst they remain functional in their native physiological environments, which techniques such as electron microscopy and X-ray crystallography cannot achieve.

This chapter begins with a description of the principles of atomic force microscopy and its main operational modes; contact mode and dynamic modes: amplitude modulation AFM (AM AFM) and frequency modulation AFM (FM AFM). Following this is a description of how AFM can be applied in liquids to image biological samples. Finally, a literature review outlines how the resolution of the images obtained in liquids has been optimised through the development of highly

sensitive AFM instrumentation and techniques, with a focus on FM AFM.

2.2. Techniques used to image biological specimens at nanometre resolution

The development of the atomic force microscope enables functional biomolecules to be imaged at nano and sub-nanometre resolution. X-ray crystallography, transmission electron microscopy (TEM), cryo-electron microscopy (cryo-EM) and nuclear magnetic resonance (NMR) are techniques which are also used to analyse the structures of biomolecules. However, they each have specific requirements which limit how these microscopic structures may be viewed.

2.2.1. X-ray crystallography and free-electron lasers

X-ray crystallography is the principle technique used to reveal detailed three-dimensional atomic models of biomolecules, such as proteins. To achieve this, the proteins are crystallised into a lattice, through which the X-rays can then diffract. The protein crystal is mounted at specific orientations and exposed to a beam of X-rays. The atoms in the crystal scatter the X-rays which are recorded on film in the form of dots called a diffraction pattern. The strength of scattering is proportional to number of the electrons in an atom. Therefore, the individual atoms can eventually be identified. The X-ray diffraction patterns are interpreted by computer. This produces a contour map of electron densities at particular planes through the crystal. Several electron density maps at varying planes through the protein crystal are assembled together to produce a three dimensional electron density, which is then interpreted in terms of biomolecular structure.

The X-ray free-electron laser (XFEL) is a recently developed tool for analysing the atomic architecture of molecules, such as biomolecules, using small crystals of a few micrometers to hundreds of nanometres in size. This technique uses ultra-short, high intensity X-ray pulses (lasting for a few femtoseconds) which are targeted onto the small crystal structures. Because of the short duration of the pulse, diffraction information can be recorded before the sample is destroyed

because of their high intensity [28].

Although, X-ray crystallography can create detailed structural models of biomolecules, the samples must be crystallised and are not imaged in their native environments.

2.2.2. Transmission electron and cryo-electron microscopy

In transmission electron microscopy (TEM), a sample is placed under vacuum conditions and targeted with an electron beam. The sample must have a density low enough to allow the electrons to travel through. The electrons transmitted through the specimen hit a fluorescent screen, where a black and white contrast image of the sample structure is formed. The samples can also be stained to enhance contrast. A similar process is used in cryo-EM, except that the sample is imaged under cryogenic temperatures ($<$ -150°C), freezing and preserving its structure. In both cases we cannot image dynamic processes occurring in real time.

2.2.3. Nuclear magnetic resonance (NMR)

Nuclear magnetic resonance (NMR) can be used to image the three-dimensional structure of biological specimens such as proteins or nucleic acids. This technique utilises the fact that nuclei possess angular momentum, therefore have a spin. A sample is placed in an external magnetic field, causing the nuclear spins to either line up with (low energy state) or against the field (high energy state). The nuclei are then exposed to radio frequency waves of varying frequencies. This leads to the excitation of nuclear spin-states making them go from a low energy state to a higher energy state. When the nucleus returns to its relaxed state, energy is given out at a particular frequency. A Fourier transform of the frequencies detected produces a spectrum of the resonances against intensity, which is referred to as an NMR spectrum. Since each nucleus gives out its own unique frequency, the elements making up the structure can be identified as well as the estimated distances between specific pairs of atoms. This data is then used to model the three-dimensional structure of the molecule.

In NMR, the sample is immersed in solution and does not require crystallisation. However, the disadvantage of NMR is that it can only determine the relative dis-

tances between spins, making it difficult to deduce the three-dimensional structure if the molecule is large. Therefore NMR is limited to small proteins (less than 150 residues [29]).

2.2.4. Scanning tunnelling microscopy (STM)

Scanning tunnelling microscopy (STM), invented by Binnig and Rohrer in 1981 [30], allows the surface of a sample to be imaged at the nanoscale [31]. The sample is traced with a sharp tip, whilst a voltage is applied between the cantilever and conductive sample. Electrons tunnel from the tip to the surface, producing a tunnelling current and variations in the current are translated into an image. The limitation of this technique is that the surfaces being analysed must be conductive. Therefore, to resolve the structures of biological samples, they are placed on conductive substrates or coated in a conductive material which can induce structural artefacts. The invention of the STM led to the development of the atomic force microscope (AFM) which is not limited to conductive samples.

2.3. Principles of atomic force microscopy

The atomic force microscope is an instrument that detects the force between a sensor and a sample in order to deduce the three-dimensional contours of the samples surface down to the atomic-scale (see Figure 2.1). The sensor is a sharp tip attached to the end of a flexible cantilever. Cantilevers are available in varying sizes. To detect the position of the cantilever, most commercial AFMs utilize laser beam detection. In this system, a laser is focused on the back of the cantilever and reflected on to the centre of a four-quadrant photodetector. The back of the cantilever can also be coated with a highly reflective metal, such as gold, to increase the intensity of the reflected laser spot. Slight variations in the vertical deflection of the cantilever, due to tip-sample interactions, are measured as displacements of the laser spot on the photodetector. A z-piezo scanner, along with a computer-controlled feedback circuit, controls the vertical motion of the cantilever and maintains a constant tip-sample distance. The piezoelectric material in the scanner expands or contracts upon a change in voltage. Two additional piezo-scanners are used to move the cantilever in the x and y planes producing

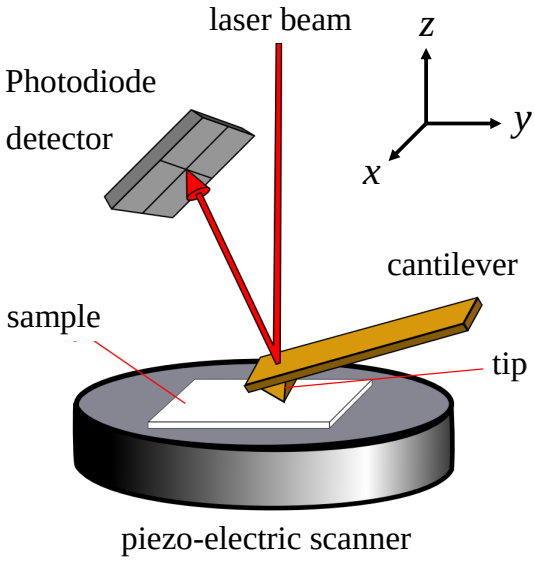

Figure 2.1.: Schematic of atomic force microscope using laser beam detection to detect cantilever position. Image adapted from [1].

line-by-line scans of the sample surface. The variations in the cantilevers position, due to tip-sample interactions, are corrected by the feedback loop and the topographic image is generated from the feedback output (z) as a function of the x-y position.

AFM can be carried out in a vacuum, air or liquid. In liquid environment the cantilever is mounted in a fluid cell and is completely submerged in the solution along with the sample. The fluid cell contains channels for adding or exchanging liquids. In the case of biomolecules, the liquid is usually a buffer solution comprised of salt ions, mimicking a specific physiological solution (further explained in section 2.4).

2.3.1. Operational modes of atomic force microscopy

The two most common AFM operational modes are contact and dynamic mode. Each mode has features which make them suited for use on particular samples.

2.3.1.1. Contact mode AFM

In contact mode (also referred to as static mode), the cantilever is traced along the

sample surface and the contact force induces bending in the cantilever (Figure 2.2 (a)). The cantilever height, with respect to the sample, is kept constant ($\leq$0.5 nm) and the magnitude of cantilever deflection is tracked to deduce the topography of the sample surface. Similarly, a constant force can be maintained whilst changes in the cantilever height can be used to create an image of the surface topography.

Due to the high lateral frictional forces being applied in this mode, loosely bound molecules or the delicate structures, like biomolecules, are prone to becoming damaged or distorted by the tip. Optimum resolution can be acquired if the molecules are densely packed or strongly adhered to the substrate [32]. Contact mode can also be used to deliberately dissect a biological sample, if required [33]. Overall, contact mode is best suited for imaging flat surfaces or samples which are not easily damaged.

2.3.1.2. Dynamic mode

The two most popular versions of dynamic mode are amplitude modulation AFM (AM AFM), also known as tapping mode and frequency modulation AFM (FM AFM) [34].

Amplitude modulation AFM

In AM AFM, the cantilever is made to oscillate at an amplitude (A) and at a fixed frequency near its resonance frequency (f_0) and intermittently taps the sample

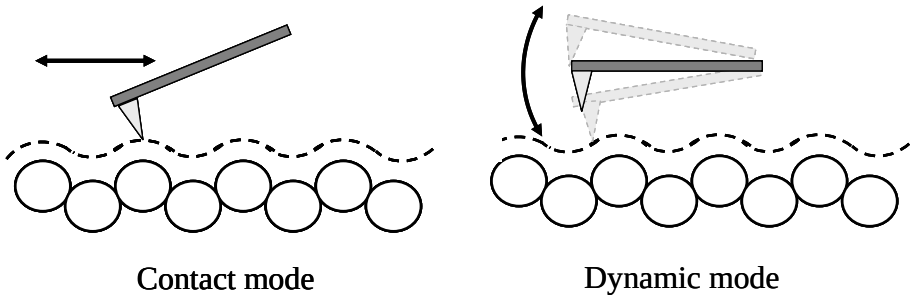

Figure 2.2.: Modes of AFM: (a) Contact mode. (b) Dynamic mode. Image adapted from [2].

surface (Figure 2.2 (b)). Tip-sample interactions are detected via changes in the cantilever oscillation amplitude which are used as the signal for the z feedback. The tapping reduces the lateral frictional forces applied on the sample, allowing individual or weakly bound samples to be imaged.

Frequency modulation AFM

In FM AFM, the cantilever is oscillated at its resonance frequency and its amplitude is kept constant. Figure 2.3 shows a typical plot of a cantilever resonance. The sharpness or finesse of the resonance curve is referred to as the quality factor (Q), which can be defined as:

$$Q = \frac{f_0}{\Delta f} = \frac{2\pi W_0}{\triangle W} \tag{2.1}$$

where f_0 is the cantilever resonance frequency, Δf is the width of the resonance curve at amplitude A/$\sqrt{2}$, W_0 is the stored energy and $\triangle W$ is the total energy loss per oscillation. In vacuum conditions $Q > 1000$, in air $Q > 100$ and in liquid $Q < 10$. As the tip traces the sample surface, tip-sample interactions cause the cantilevers resonance frequency to instantaneously shift from f_0 to $f_0 + \Delta f$ (see Figure 2.3). The cantilever resonance frequency can decrease or increase depending on whether an attractive or repulsive force acts on it (forces are explained in subsection 2.3.3). In FM AFM in liquids, imaging is usually carried out in the repulsive range, where the frequency of the cantilever increases as a result of the repulsive forces that act between the tip and sample (shown in Figure 2.5). These frequency shifts are monitored by a frequency detector and are used to regulate the tip-sample distance. The frequency shifts are a direct measure of the (elastic) tip-sample interactions and determine the contrast of the AFM image. In addition to frequency shifts, dissipative interactions reduce the cantilever oscillation amplitude and therefore reduce the Q of the resonance peak. An amplitude controller is used to maintain a constant cantilever oscillation amplitude, in which the amount of drive energy required to keep the cantilever amplitude constant,

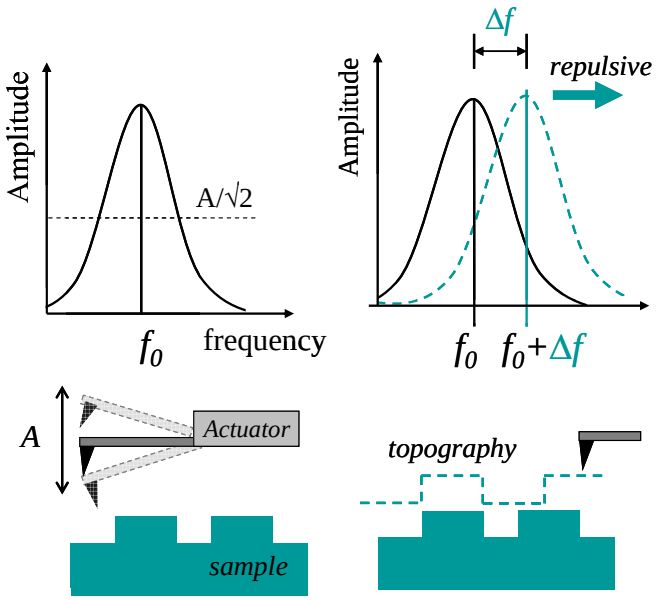

Figure 2.3.: Schematic depicting principle of FM AFM. The shift in resonance frequency is used as feedback to regulate z-piezo distance.

is a measure of dissipated energy. As a result, the FM AFM has the advantage of being able to independently measure elastic and dissipative interactions [35]. This is in contrast to AM AFM, where the shifts in cantilever amplitude (imaging signal) contains a mixture of information of these interactions [36].

2.3.2. Cantilevers and tips

Cantilevers are usually made of silicon or silicon nitride and are commercially available in various sizes. The flexibility of an AFM cantilevers is governed by its spring constant k. In simple terms, since the tip-sample interactions cause a deflection, x, of the cantilever, the resulting force (F) can be described using Hooke's Law:

$$F = -kx \tag{2.2}$$

For standard rectangular cantilevers the spring constant is related to its dimensions by:

$$k = \frac{Et^3w}{4l^3} \tag{2.3}$$

where l, w and t are the cantilever length, width and thickness, respectively, and E is the Young's modulus [36]. Softer cantilevers with $k = 0.01$ - 1 N/m have the advantage of a high force sensitivity. These are suited for contact mode imaging since the cantilever must be flexible enough to withstand high load forces. Stiffer cantilevers with $k = 10$ - 100 N/m, generally have a higher Q in water, which can facilitate dynamic mode operation.

2.3.2.1. Sharp tips and tip convolution

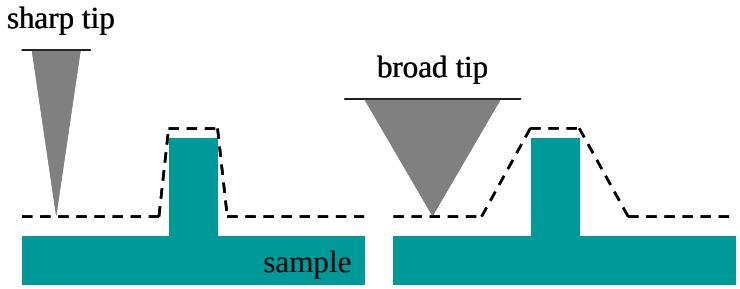

Figure 2.4.: Schematic to show the effect of tip shape on surface topography. Image adapted from [3].

Standard commercial cantilever tips typically have 10 - 50 nm radius, electron beam deposited (EBD) tips ~ 5 nm and super sharp silicon (SSS) cantilever tips ~ 2 - 5 nm. The spatial resolution of an AFM image is ultimately dependent on the sharpness of the cantilever tip. As illustrated in Figure 2.4, if the tip radius is greater than the size of the feature being traced, the edges of the tip interact with it first, making the feature appear broader than its actual size. This is called the 'tip broadening affect'. Another common occurrence is a 'tip-change'. This is when shape of the tip end alters while scanning, e.g by pick-up of particles from

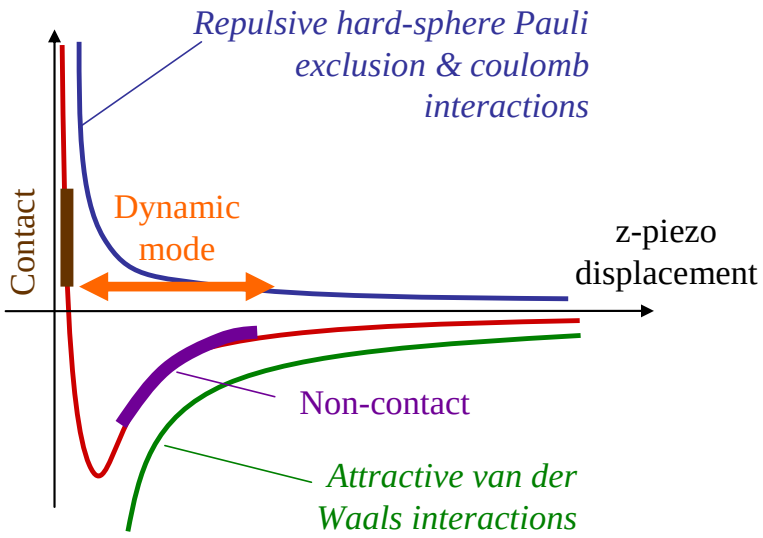

Figure 2.5.: Force versus z-piezo displacement graph depicting the forces acting on the cantilever during its approach towards the sample surface (see text).

the sample surface. After a tip-change, the features in the topographic image may appear to change in contrast, become shadowed or else repeated over the surface.

In principle, a sharp tip will aid in acquiring high spatial resolution however, the force applied must also be carefully controlled to prevent damage to tip or sample, particularly in the case of soft biological samples. If excessive forces are applied on the sample, the sample can also appear compressed.

2.3.3. Forces

The tip-sample interaction forces can be mapped as a function of z-piezo displacement, to produce a 'force curve'[1]. Figure 2.5 depicts an example of a force curve produced when a cantilever is approached towards a sample surface (shown by red curve). During the approach two forces begin to take effect [4, 37].

[1]It is important to note that the x-axis is a measure of the z-piezo displacement and not the tip-to-sample distance

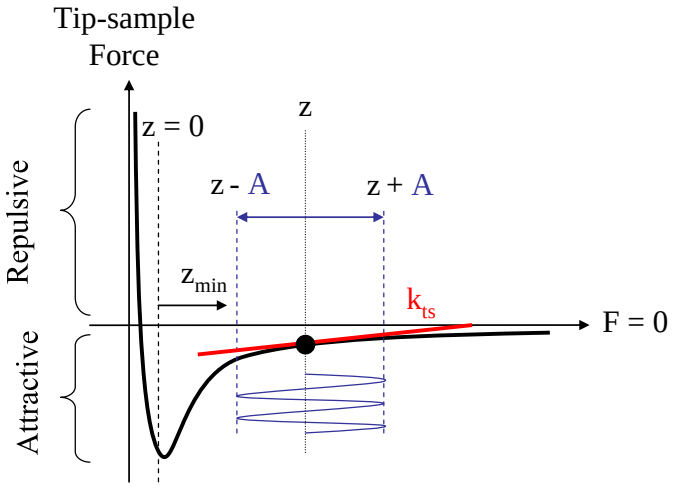

Figure 2.6.: Tip-sample force versus z-piezo displacement curve of a cantilever with amplitude A, where distance of closest approach between tip and sample is noted as z_{min} (see text).

One of these forces is the attractive van der Waals force, which arises from temporary fluctuating dipoles (shown by green curve in Figure 2.5). This force can act over many tens of nanometres and the magnitude of attraction increases as the tip becomes closer the surface. When in close proximity to the sample, short-range, hard-sphere interactions arising from the Pauli exclusion principle begin to take effect. In addition long-range electrostatic forces may be present (blue curve in Figure 2.5).

When imaging in air, atmospheric humidity can cause a small meniscus of water to form between the tip and the sample. As a result, capillary forces (which act can over many nanometres) cause an excessive attraction between the tip and sample. This increases the tip-sample contact area, reducing resolution as well as adding an undesirable pressure that can damage the sample. This effect is particularly apparent when the cantilever is retracted, since the adhesion makes it difficult to separate it from the surface. One advantage of imaging in liquid is that these capillary forces do not exist.

In FM AFM, elastic (conservative) tip-sample interaction force gradients are measured as frequency shifts of the cantilever against z-piezo displacement. It is

important to be able to quantify the corresponding tip-sample interaction force given by the instantaneous frequency shifts (Δf) of the cantilever. A paper by Sader and Jarvis et al [38] accurately derives the formula required to convert measurements of frequency shift to tip-sample interaction force. The interaction force can be expressed in terms of frequency shift by:

$$F(z_{min}) = 2k \int_{z_{min}}^{\infty} \left(1 + \frac{a^{1/2}}{8\sqrt{\pi(z - z_{min})}}\right) \Omega(\xi) - \frac{a^{3/2}}{\sqrt{2(z - z_{min})}} \frac{d\Omega(z)}{dz} dz \quad (2.4)$$

where k is the spring constant of the cantilever, a is the oscillation amplitude and z_{min} is the distance of closest approach between tip and sample (see Figure 2.6). Ω is the frequency shift with respect to tip-sample distance z and is given by:

$$\Omega(z) = \triangle f(z)/f_0 \quad (2.5)$$

in which Δf is the change in resonance frequency and f_0 is the unperturbed resonance frequency of the cantilever. As described above, interaction forces can occur over varying length scales. Therefore, if the cantilever is oscillated at large amplitudes, the range of forces that the tip experiences differs from when the amplitude is small. Hence, Sader and Jarvis's formula contains 3 terms which correspond to small and large oscillation amplitudes and a interpolation term between them. For small amplitudes of oscillation a cantilever can be modelled as mass (m) on a spring with a spring constant k, where its behaviour can be expressed by the equation of motion:

$$m\ddot{z} = kz \quad (2.6)$$

and its resonant frequency is simply:

$$f_0 = \sqrt{\frac{k}{m}} \quad (2.7)$$

As illustrated by Figure 2.7, if the cantilever is bought close to a sample surface, it can be displaced from its equilibrium position by an attractive interaction force.

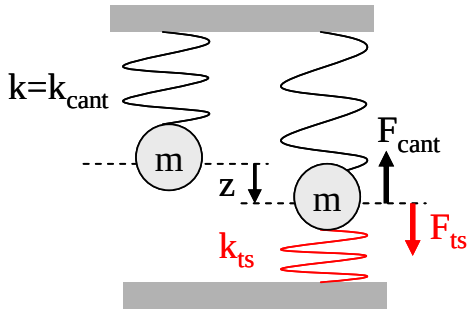

Figure 2.7.: A schematic representing a cantilever as a mass on a spring with spring constant k, where the frequency shift in the cantilever resonance is governed by the effective tip-sample spring constant k_{ts} (further explained in text).

This interactive tip-sample force can be represented by a second spring with a effective tip-sample spring constant k_{ts}. This alters equations (2.6) and (2.7) to:

$$m\ddot{z} = -kz + k_{ts}z = -(k - k_{ts})z \tag{2.8}$$

$$f = \sqrt{\frac{k - k_{ts}}{m}} = \sqrt{\frac{k}{m}\left(1 - \frac{k_{ts}}{k}\right)} \simeq f_0\left(1 - \frac{1}{2}\frac{k_{ts}}{k}\right) \tag{2.9}$$

Therefore, the frequency shift $\Delta f(z)$ of the cantilever can be expressed as:

$$\triangle f(z) = f - f_0 = -\frac{f_0}{2k}k_{ts} \tag{2.10}$$

where the spring constant of the tip-sample interaction is equal to the derivative of the force ($dF_{ts}(z)/dz$) with respect to the position z (shown as the gradient of the slope in Figure 2.6). Therefore, equation (2.10) equals:

$$\triangle f(z) = -\frac{f_0}{2k}\frac{dF_{ts}(z)}{dz}$$

$$\therefore F_{ts}(z) = -2k \int_{z_{min}}^{\infty} \frac{\triangle f}{f_o} dz \tag{2.11}$$

In this example, the attractive tip-sample interaction force implies a negative frequency shift. In the repulsive range, the frequency of the cantilever increases as a result of the repulsive forces acting between the tip and sample. Hence, as shown by the first term in (2.4), for small amplitude oscillations the force is equal to $2k \int \Omega dz$. This illustrates that, in the limit of small amplitudes, the measured frequency shift corresponds to the gradient of the tip-sample force.

Sader and Jarvis et al [39] have also mathematically analysed the behaviour of the frequency shifts as a function of amplitude for large oscillation amplitudes. It has been shown that in the large amplitude limit, the frequency shift is proportional to the half fractional integral of the force [39]. This is represented by the term $\frac{a^{3/2}}{\sqrt{2(z-z_{min})}} \frac{d\Omega(z)}{dz} dz$ in equation (2.4). Finally $\left(\frac{a^{1/2}}{8\sqrt{\pi(t-z)}}\right) \Omega(z)$ refers to the interpolation term which allows the transition from small amplitudes to large amplitudes.

In summary, this formula quantifies the magnitude of tip sample interaction in terms of frequency shift and can be used regardless of the nature of the force measured or the size of cantilever oscillation. As long the amplitude of oscillation and the spring constant of the cantilever are known, the frequency shift versus tip-sample distance curve can be complied in a basic Mathematica program in which Sader and Jarvis' formula is used to convert frequency shift (Hz) into force (N) with respect to varying tip-sample distances (z).

Similarly, the same parameters can be used to determine the interaction energy if desired, which is given by:

$$U(z_{min}) = 2k \int \Omega(z) \left((z - z_{min}) + \frac{a^{1/2}}{4} \sqrt{\frac{z - z_{min}}{\pi}} + \frac{a^{3/2}}{\sqrt{2(z - z_{min})}} \right) dz \tag{2.12}$$

2.4. AFM imaging in liquids

2.4.1. Tuning resolution in liquids

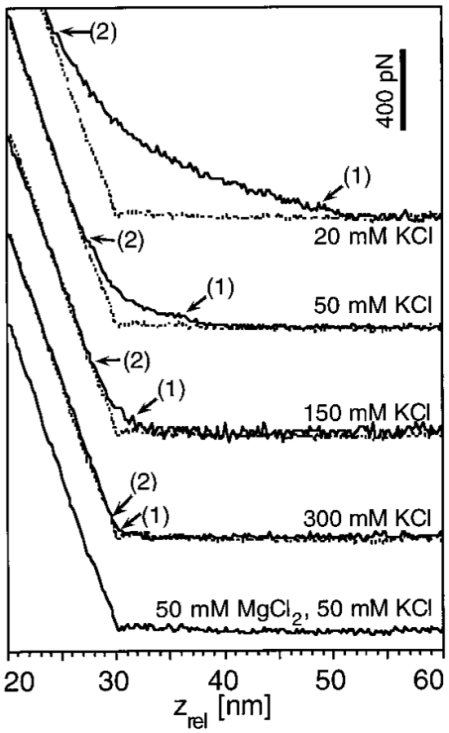

Figure 2.8.: Force versus z-piezo displacement plots of a cantilever approaching the outer surface of a HP1 layer, as shown by Muller et al [4]. Resulting force curves correspond to varying concentrations of electrolytes in buffer solution (with constant pH) to demonstrate the effect of reducing debye lengths (see text).

Other than the tip sharpness, the resolution ability of the AFM also depends on the tip-sample interaction range. To obtain optimum resolution, it is important to detect the short-range forces between the tip and the sample. The longer-range electrostatic repulsion between the tip and sample can make it difficult to detect the detailed surface features and therefore impairs resolution. The distance over

which this force decays is defined as the Debye length (κ^{-1}):

$$\kappa^{-1} = \sqrt{\frac{\varepsilon_0 \varepsilon_b k_B T}{2e^2 I}} \tag{2.13}$$

where ε_0 and ε_b are the permittivity of a vacuum and bulk solution respectively, k_B is Boltzmann's constant, T is temperature, I is ionic concentration and e is the electronic charge. An advantage of working in liquids is that these tip-sample interactions forces can be carefully tuned by the use of an imaging buffer. The imaging buffer is made up of electrolytes of varying concentrations and specific pH levels and is used to balance the undesired attractive or repulsive forces between the tip and sample. Minimal forces can therefore be applied to the surface of delicate samples and the short-range forces between tip and sample can be detected.

The effectiveness of buffer concentration has been well demonstrated by Muller et al [4]. The authors used varying electrolyte concentrations in the imaging buffer and recorded the resulting force versus z-piezo displacement (z_{ref}) curves, during the cantilevers approach to the surface (shown in Figure 2.8). Arrow (1) in the figure indicates the point of measurable electrostatic repulsion and arrow (2) marks the point when the tip and sample made contact. It can be seen that with a low buffer concentrations Debye lengths were long. As the concentration was increased, Debye lengths became effectively reduced, therefore the distance between the onset of repulsion and point of contact becomes reduced. The final force curve shows the buffer which most effectively reduced this long-range repulsion, thereby yielding images of high resolution.

2.4.2. Imaging biological samples

Another crucial factor that influences the resolution of an AFM image, is the sample preparation. The sample must be sufficiently immobilised on the substrate to prevent the lateral motion of the cantilever from causing damage to its structure or dislodging it off the surface. To achieve this, most biomolecules are

physically adsorbed, o*r physisorped,* on a substrate such as muscovite mica, glass, silicon, high oriented pyrolitic graphite (HOPG) or gold. Physisorption is based on an electrostatic and/or van der Waals interactions between the biomolecule and the substrate. Since it is a non-permanent interaction it is less likely to cause physical changes to the biomolecular structure.

Successful adsorption is achieved with the use of specific electrolytes in the liquid referred to as an adsorption buffer. The pH and electrolytes in buffer solution also replicate the native environment in a living cell, to ensure the biomolecule remains functional. For example, most proteins remain positively charged if the pH of the liquid buffer is below their specific isoelectric point (pI)[2]. Therefore, buffers with this specific pH would assist the protein in adsorbing to mica [40]. The mica surface charge also depends on the pH of the buffer. Dependent on the desired coverage, X concentration of a protein is allowed to adsorb on the substrate in adsorption buffer, for x amount of time. After adsorption, the sample is thoroughly rinsed to remove any unbound proteins. Protocols for biological samples such as proteins, liposomes or DNA, can be found in literature. However if unknown, it is essential that the sample preparation is perfected to ensure optimum image resolution [41]. If the sample is not bound well enough the image can appear streaky or smeared. If bound too well, this can cause structural changes to the bound molecule.

Chemical fixation, or *chemisorption,* can also be used in which a chemical reaction forms a covalent-bond between the sample molecules and the substrate. Although this provides a strong attachment to the surface, chemical fixation has the disadvantage of potentially damaging the structure and the functionality of the biomolecule.

Muscovite mica is most commonly used as a substrate for biological imaging due to its atomically flat surface and the fact that the sample is not influenced by its surface [20] (further explained in chapter 5). It is hydrophillic and negatively charged (-0.0025 C m^{-2}, at neutral pH) and can even be altered to become positively charged if required. Thin sheets of this relatively inexpensive mineral may be cut into any desired shape or size and since the mineral is composed of several

[2]pI is the pH at which it the protein is electrically neutral.

layers, it can be cleaved with tape to leave a clean surface to adsorb onto.

2.5. Literature Review: FM AFM for achieving high resolution images in liquid

Contact mode AFM is commonly used to acquire high resolution image of samples in liquids. In fact, the highest resolution image obtained using AFM, was acquired by Ohnesorge et al [42] who used contact mode to capture atomic resolution images of calcite in water. This image had lateral resolution of $\leq$ 1 Å and vertical resolution a few picometers. True atomic resolution has now also been obtained using FM AFM in liquid, for example by Hoogenboom et al [16] and Fukuma et al [7], who have acquired true atomic resolution of muscovite mica (further discussed in chapter 5). This has been achieved through the development of highly sensitive instrumentation and techniques which are outlined below.

2.5.1. Advances in instrumentation for FM AFM imaging in liquids

Frequency modulation atomic force microscopy was first introduced in 1991 by T. R. Albrecht et al [43], who described a FM demodulation technique to carry out fast measurements of frequency shift in ultra high vacuum (UHV). From this historical beginning, FM AFM imaging has been traditionally carried out in ultra high vacuum. In such conditions, the cantilever poses a very high quality factor (Q $>$ 1000), resulting in high signal-to-noise ratios (SNR). As a result, FM AFM in UHV has been used to acquire atomic scale images of various solid surfaces [44, 45, 46, 47, 48, 49]. This was first demonstrated by Giessibl et al [50] in 1995, who imaged the (111)-(7x7) surface of silicon at atomic resolution. In 1997, Durig and Loppacher et al [47, 51] were the first to introduce a phase locked loop technique (explained further in subsection 3.2.3). The cantilever was resonated in an active feedback circuit and a phase-controlled oscillator method of detecting tip-sample interactions was first implemented.

It was not until 2000 that the first application of FM in liquid was initiated

by Javis et al [5]. With the use of a carbon-nano-tube tip and magnetic actuation, this group was successful in imaging the periodic striped phase of a hydrophilic self-assembled monolayer of COOH(CH2)10-SH on Au(111) (Figure 2.9 (a)). Javis et al [52] then combined frequency detection with spectroscopy, which included a custom-built PLL circuit, to detect solvation shell structures in octamethylcyclotetrasiloxane (OMCTS) and water. Since then, at Kyoto University in Japan, a research group have been able to successfully image the surface of Au (111) in liquid, using a FM AFM which is comprised of a highly sensitive home-built PLL circuit in conjunction with piezoelectric cantilever actuation [53]. Okajima et al [54] has also described that with the use of a self-oscillation circuit with a commercial AFM, they were able to image sputtered Au thin film in water. An early example of FM AFM being applied to imaging a biological samples, was demonstrated by Sekiguichi et al [55]. The authors imaged fibrillary tau proteins, which are a key component in the cause for Alzheimer's disease, using FM feedback in liquid with a self-oscillation technique in physiological conditions.

2.5.1.1. Low-noise cantilever detectors

When the cantilever is oscillated in liquid, the amplitude of its resonance frequency becomes damped and Qs become exceptionally low (< 10). If the cantilever detector possesses a high noise floor (near 100 fm/$\sqrt{\text{Hz}}$), this low Q cantilever signal becomes very difficult to single out from the background noise. In addition to this, piezo-actuation is typically used to actuate the cantilever, which involves mechanically driving the back of the cantilever support chip (further explained in subsection 3.2.4). The cantilever resonance may thus be obscured by the other sharper mechanical resonances. Therefore, low-noise detectors ($<$ 10 fm/$\sqrt{\text{Hz}}$) are crucial for ensuring low Q cantilever signals can be detected in liquid (further explained in subsection 4.4.1).

Research groups have been developing low-noise cantilever detection sensors in order to enhance the signal-to-noise ratio (SNR) of the cantilever's resonance signal. Advances in these detectors allow the thermal noise of the cantilever to be measured and cantilever amplitudes down to an Angstrom (10^{-10}) to be

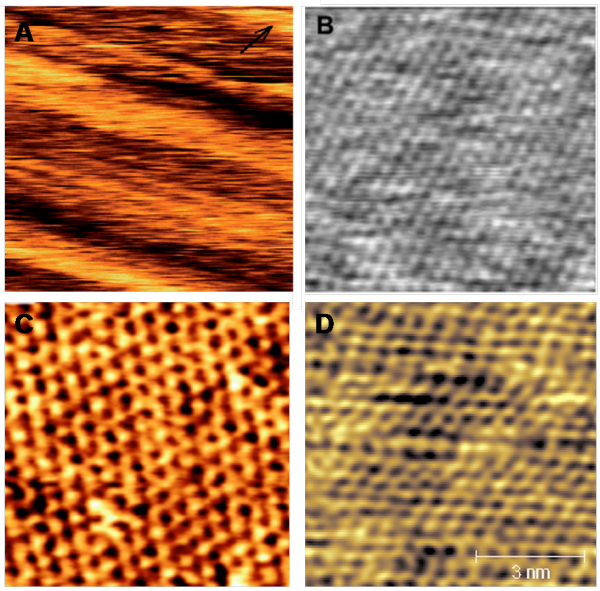

Figure 2.9.: (a) FM AFM image of a 12 x 12 nm area of striped phase of a hydrophilic self-assembled monolayer of COOH(CH2)10-SH on Au(111) as acquired by Javis et al [5]. Arrow points to the location of solvation shells. (b) 10 x 10 nm image showing individual head-groups of lipid molecules hexagonally packed with an intermolecular distance of 0.51 nm. Image obtained from Higgins et al [6] (c) 7 x 7 nm FM AFM image of (001) the cleaved surface of muscovite mica in water, obtained by Fukuma et al [7]. (d) True atomic resolution FM AFM image of muscovite mica acquired by Rasool et al [8] in pure 18.2 MΩ water (8 nm x 8 nm).

detected. For example, a group led by Takeshi Fukuma at Kanazawa University in Japan, have developed a highly sensitive FM AFM that includes a low noise optical beam deflection (OBD) sensor, for use in air, liquid and UHV. When this system was first implemented, the sensor possessed a noise floor of 40 fm/√Hz in liquid. By refining the optical design, it has been considerably reduced down to 4.7 fm/√Hz over the past 8 years [7, 56, 57, 58, 59], with a corresponding increase in image resolution. Using this FM AFM in liquid, this group have imaged true atomic resolution of the hexagonal lattice of a cleaved muscovite mica surface in water [7] (Figure 2.9 (c)), bacteriorhodopsin protein molecules in purple membrane and isolated chaperonin protein GroEL [60], individual head-groups of hexagonally packed lipid molecules [6] (Figure 2.9 (b)), α-synuclein

protofibrils on mica in water [61], lipid ion network formation [62] and hydration layers on lipid bilayers at (Å) angstrom resolution [63].

Hoogenboom et al [14] and the group at the University of Basel, Switzerland have developed a Fabry–Perot interferometer particularly suited for detecting the deflection of reduced dimension cantilevers [9]. This highly sensitive cantilever detector yields a noise floor of a mere 1 fm/$\sqrt{\text{Hz}}$ at 1 MHz and has been used with FM AFM to image the cleaved surface structure of muscovite mica in buffer at true atomic resolution (see chapter 5). Furthermore, the set up has been used to image the bending of a peptide loop connecting transmembrane helices of the membrane protein bacteriorhodopsin [16]. Voltage-dependent anion channels (VDAC) in the outer mitochondrial membrane taken from potato tubers have also been imaged [64] with 20 Å lateral resolution. Hoogenboom et al [65] and his group at University College London, have set up a modified version of this detector, which utilises optical actuation to oscillate the cantilever. This FM AFM is able to detect the thermal noise of reduced size cantilevers which are oscillated at < 1 nm amplitudes in liquid. Using this set up our group have recently acquired images of the two polynucleotide strands in the DNA double helix in physiological conditions. A periodicity of 3.5 ± 0.4 nm can be seen along the helix as well as 0.1 nm grooves which separate each turn.

Rasool et al [8] has developed an all-fibre low-noise Fabry-Perot interferometer, used to detect the cantilever for high resolution FM AFM imaging in liquids. In this publication, the authors demonstrated the profound effect of reducing the detector noise on the resolution of imaging. By ensuring maximum laser reflectivity within the interferometer, this set up has been measured to possess a noise floor as low as 2 fm/$\sqrt{\text{Hz}}$ (origins of noise are further explained in subsection 4.4.2). The ability of this microscope was then demonstrated by acquiring an atomic-scale resolution image of mica (Figure 2.9 (d)), using commercial cantilevers that were oscillated at an amplitude of 0.275 nm.

A low-noise hetrodyne laser doppler interferometer cantilever sensor has also been described by Kawakatsu et al [66], where the cantilever is excited via photothermal excitation. This involves using the effects of bi-metallic heating to cause excitation of the cantilever. In order to increase spatial resolution, higher modes

from the fundamental frequency of the cantilever were detected and used to oscillate the cantilever in liquid at small amplitudes. Using dynamic force microscopy (DFM), the authors demonstrated the ability of using small amplitudes with this detector by imaging atomic-scale resolution of mica in water [67].

2.5.1.2. Small cantilevers and fast frequency detectors

To increase resolution it is important to detect the very small (< nN) tip-sample interactions. In the case of FM AFM, these small forces would cause very small frequency shifts in the cantilever. Therefore, the resolution depends on the minimal detectable frequency shifts. The force noise resulting from thermal fluctuations of the cantilever is given by:

$$F_{th} = \sqrt{\frac{2kk_BTB}{\pi f_0 Q}} \tag{2.14}$$

where k is the spring constant, k_B is Boltzmann's constant, B is bandwidth, T is temperature and Q the quality factor [9]. This sets the lower limit of the minimal detectable force. Therefore, to increase force sensitivity, F_{th} should be reduced, which would therefore require a cantilever with high resonance frequency f_0 and low spring constant k [9]. If the cantilever is modelled as a mass on a spring, the relationship between its f_0, k and mass m is:

$$f = \frac{1}{2\pi}\sqrt{\frac{k}{m}} \tag{2.15}$$

Therefore, to obtain a combination of high f_0 and low k, the cantilevers mass must be decreased. To achieve this, the dimensions of the cantilever can be reduced. Reduced sized cantilevers are referred to as 'small cantilevers' and have typical dimensions of 25 x 4 x 0.2 μm^3 [9, 14]. By oscillating these cantilevers at small amplitudes (0.1 - 3 nm), resolution is increased through increased sensitivity to

small shorter range tip-sample interactions. However, these cantilevers can have MHz resonant frequencies in air. To successfully measure these high resonant frequencies, frequency detectors (FD) with the ability to measure frequencies in the MHz range are required. Until recently commercial AFM frequency detectors were not capable of tracking frequencies in this range, so research groups have fabricated small cantilevers and constructed home-built FDs or customised commercial FDs, in order to detect them. For example, Hoogenboom and co-workers in Basel, Switzerland have developed small probes [9], for which the set-up described in this thesis is designed to detect. Hoogenboom and Leung et al [65] have recently demonstrated the ability of using small cantilevers with FM AFM to reveal structural conformations of a DNA double helix. Fukuma and co workers have also further improved the resolution of their FM AFM by using of small cantilevers [57, 58].

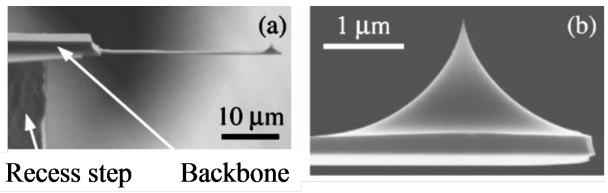

Figure 2.10.: (a) Scanning electron microscope image of a small cantilever of dimensions 25 x 4 x 0.2 μm^3. (b) Close-up of a small cantilever tip with a 10 nm diameter [9].

Small high resonance frequency cantilevers and high speed frequency detectors also allow for increased imaging speeds [68]. The development of fast-scanning AFMs have the potential to allow the complex dynamics of biological mechanisms to be videoed in real time, rather than being captured as a static image. This has been most convincingly shown by Ando et al [69], where he and his co-workers developed a high-speed AFM, which uses small cantilevers for fast scanning of biological macromolecules in liquid [69]. This AFM is capable of capturing a 100 x 100 pixel image in 80 ms, in comparison to commercial AFMs which take minutes. The group have applied this to image myosin V changing orientation on mica, at a scan rate of 1.25 kHz, corresponding to a tip speed of 0.6 mm/s.

Walters et al. [70] have also produced small cantilevers of lengths 23 to 203 μm and Viani and his co-workers have fabricated [71] and used small cantilevers [72] with AFM for fast imaging [73], to image a chaperonin protein GroES binding and dissociating from chaperone protein GroEL [74] (further discussed in chapter 6).

2.6. Conclusion

AFM for imaging biomolecules in liquid

In summary, to obtain high resolution images of biological sample using FM AFM in liquids, the following are required:

- The correct sample preparation (adsorption buffer, adsorption time and substrate type) in order to sufficiently bind the sample to substrate for stable scanning.
- A carefully selected imaging buffer to balance the net force between tip and sample, where the Debye length must be sufficiently reduced to minimize long range electrostatic forces.
- Carefully control the load force of the cantilever to ensure minimal forces are applied to the delicate structures.
- Use a sharp tip with dimensions smaller than the contours of the surface of the sample to be image. In principle, the sharper the tip the higher the spatial resolution of the AFM image is.
- Use a highly sensitive cantilever detector for the detection of small range interaction forces and small oscillation amplitudes. This would enhance the sensitivity to short range interactions that are necessary for obtaining true atomic resolution images.
- Ensure high cantilever signal-to-noise ratios are obtained even in liquids. This can be achieved with a cantilever detector that possesses a low enough noise floor to ensure low-Q cantilever resonances can still be detected in liquids.

- Use a fast frequency detector with a fast feedback system with the ability to successfully track cantilevers frequencies up to MHz range.

Limitations of AFM

Although AFM has several advantages over other imaging techniques, there are a few limitations to its technique and ability:

- Only the topography of the samples surface can be imaged, in comparison to X-ray crystallography where the samples are imaged in three dimensions.
- The resolution of the image is limited by the cantilever tip. The definition of sample features are the outcome of the sharpness of the tip and can also be affected by tip convolution effects.
- AFM is an invasive technique. The force exerted by tip must be controlled well, in order to cause minimal damage to the sample, particularly when imaging soft biological samples.
- The scanning speed is limited, which restricts the imaging of dynamic biological processes in real time. Fast scanning is an area that is still being developed.

3. Frequency Modulation Atomic Force Microscopy

3.1. Introduction

Frequency modulation atomic force microscopy (FM AFM) was first introduced in 1991 by T. R. Albrecht et al [43] and since then it has been used to image atomic structures of solid surfaces in ultra high vacuum [7, 75, 16, 60, 76]. The application of this method to observe biological samples in liquids has only recently become more common.

This chapter begins with a detailed description of the electronical set-up for our FM AFM, which is tailored to the use of small cantilevers with MHz frequencies in air and liquids. When this set-up was first developed (2009), it clearly outperformed all commercially available bench-top frequency detectors in the frequency range appropriate for small cantilever AFM. Next is a description of various tests that were carried out to characterize its frequency range, its modulation bandwidth for amplitude/phase and its step-response.

3.2. Frequency modulation atomic force microscopy experimental set-up

3.2.1. Overview of set-up

Figure 3.1 shows a schematic diagram of our overall FM AFM set-up. The cantilever is mounted above the sample and the tip-sample distance is adjusted using

a z-piezo scanner on which the sample is attached. The cantilever position is detected by an interferometric cantilever detector (further explained in Chapter 4). A home-built lock-in amplifier, a phase locked loop (PLL) and an excitation circuit make up the frequency/phase and amplitude detector (each component is explained in detail in the following sections of this chapter).

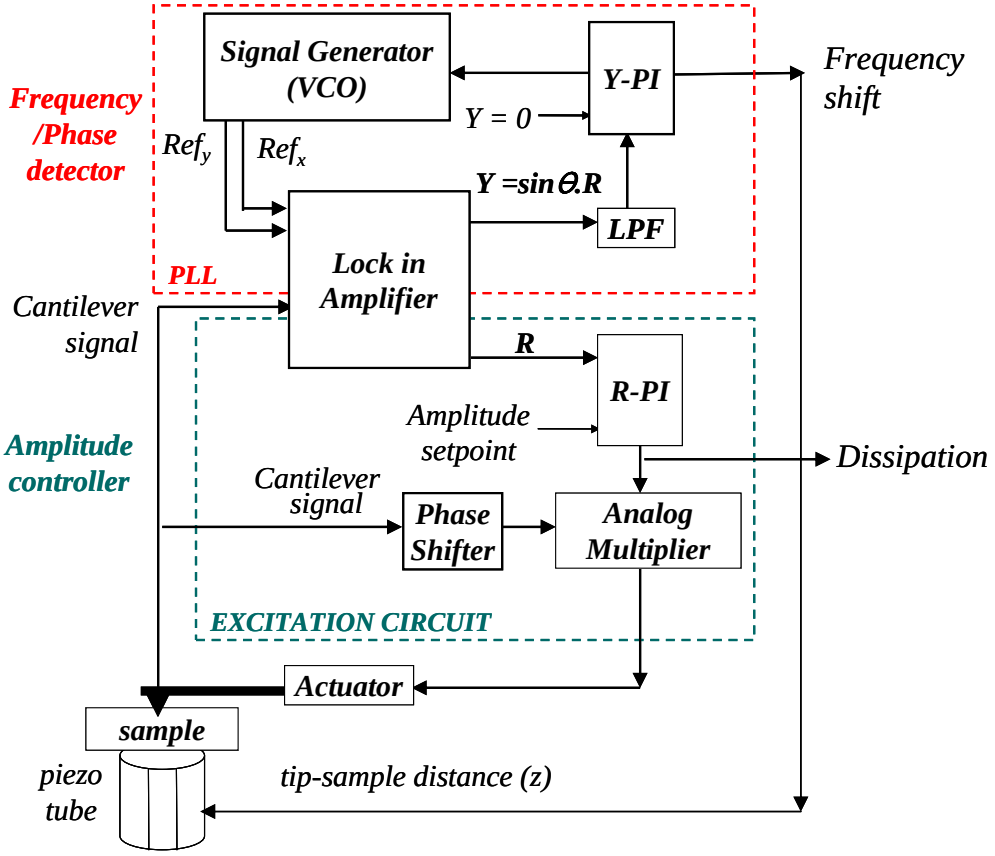

Figure 3.1.: A block diagram of the FM AFM, displaying the cantilever above the sample, the excitation circuit used to control cantilever amplitude and the phase locked loop (PLL) making up the frequency/phase detector. The feedback units are indicated by the *Y-PI* (for phase feedback) and *R-PI* (for amplitude feedback).

During imaging, the tip-sample interaction is detected as a shift (Δf) in the cantilever resonance frequency. The signal corresponding to this frequency shift is fed through a P-I (proportional-integral) feedback controller. The feedback adjusts the position of the z-piezo to regulate a constant tip-sample distance by

keeping the frequency shift constant. The amplitude signal (R) is fed to a separate feedback loop which is used to maintain the amplitude of the cantilever oscillation constant. The cantilever signal is also used to *drive* the cantilever. This is referred to as self-excitation mode. As shown in Figure 3.1, the cantilever signal is phase shifted by 90^{o} through the use of a phase shifter. It is then multiplied with the output of the amplitude P-I feedback (which is determined by the difference between the cantilevers actual oscillation amplitude and a user-defined amplitude). This signal is passed to an actuator on which the cantilever support chip is attached. Thus the actuator either increases or reduces the oscillation amplitude to reach a user-defined amplitude set-point.

The resulting set-up detects the cantilever amplitude, which is kept constant, and frequency (at constant phase), which is used as AFM imaging feedback to create a topographic image of the sample.

3.2.2. Amplitude and phase detector

A lock-in amplifier detects the amplitude and phase of the signal using a reference provided by a voltage controlled oscillator (VCO). Figure 3.2 shows an example of how this is achieved. In Figure 3.2 (a), the input signal is a signal from a cantilever with resonance frequency (f) and amplitude *(*A). The second is a reference signal with the same f and fixed A. In this case, there is no phase difference between the two signals. The lock-in amplifier multiplies the two signals to produce an output signal that has a frequency twice that of the reference and signal inputs (*2f*, AC component) and a positive mean value (DC component). The lock-in amplifier outputs a signal with an amplitude that corresponds to the product of the signal and reference amplitudes. If the cantilever signal is phase shifted by 90^{o} (Figure 3.2 (b)), then upon multiplying it with the reference signal, the resulting output frequency becomes *2f*, however the DC component becomes 0. In general, the DC component of the output signal is proportional to the amplitude of the product of the two signals and directly related to the phase difference between them. In order to measure the DC signal alone, the *2f* AC component is removed by passing the signal through an external low pass filter. In our set-up a

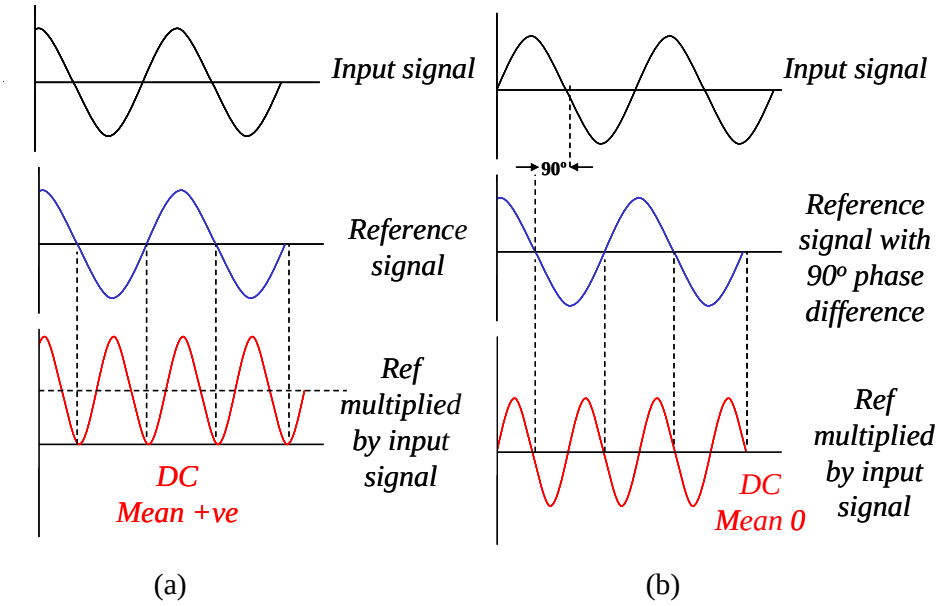

Figure 3.2.: (a) An example of identical input and reference signals, which when mixed, results in a positive DC component. (b) A 90º phase shifted reference signal mixed with a input signal, resulting in a zero DC output (image adapted from [10]).

dual-phase lock in amplifier is used in order to measure the change in phase and amplitude independently. This produces two outputs X and Y, using reference signals that are 90° out of phase.

Figure 3.3 shows the block diagram of the electronics of our home-built dual phase lock-in amplifier. The raw cantilever signal is first fed into a transformer (T1-6-X65+, frequency range: 10 kHz–150 MHz), which prevents ground loops, then into the lock-in amplifier. The signal is then split by a 50 Ω four-way splitter (PSC-4-6+, 10 kHz–40 MHz). One signal is fed to the amplitude controller (further explain in subsection 3.2.4) and the second to an oscilloscope to monitor the cantilever oscillation. The final two signals are multiplied by reference signals via mixers (SRA-6+, 3 kHz–100 MHz) within the lock-in amplifier (shown in Figure 3.3). Two reference signals with a 90º phase difference between them are provided by the function generator, where Ref_x is a sinusoidal output and Ref_y which is a cosine wave. The frequency generator allows the reference frequency,

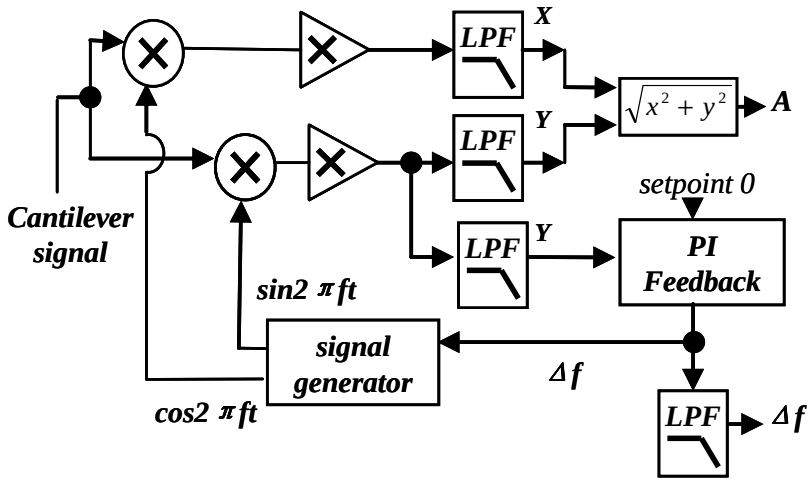

Figure 3.3.: Block diagram of the home-built dual phase lock in amplifier electronics.

amplitude or phase to be modulated up to a modulation bandwidth of 70 kHz [12]. The frequencies of both reference signals are set with a value equal to the cantilever resonance frequency. This is entered as a centre frequency in a user-designed LabVIEW program[1] along with a frequency span. Each reference signal is then multiplied by the cantilever signal.

Ref_x is multiplied by the cantilever signal and produces a DC signal that corresponds to the projections of the signal on the X (real, cos2πft) axis of the complex plane:

$$X = V_{sig} cos\theta = V_{sig} cos\,(2\pi f t) \tag{3.1}$$

where V_{sig} is the cantilever input signal and θ = $(\theta_{sig}$- $\theta_{refx})$ is the phase difference between this signal and reference signal Ref_x [10]. When Ref_x is in phase with the cantilever i.e. θ equals 0, this implies $cos(0) = 1$. This leaves X to be proportional to V_{sig}. If θ equals 90°, this would result in a output of zero. Therefore, to eliminate this phase dependency the second reference signal Ref_y is

[1]This was designed and created by MSc student B. Tahir [77].

used.

When Ref_y is multiplied by the cantilever signal this results in a signal Y (imaginary, sin2πft) axis of the complex plane.

$$Y = V_{sig} sin\theta = V_{sig} sin\left(2\pi ft\right) \tag{3.2}$$

These two components represent the cantilever signal as a vector quantity, with respect to the two orthogonal phased reference signals (shown in Figure 3.4). X and Y are then fed into 25 kHz low pass filters (LPF), rectifiers (AD822) and most importantly a logarithmic vectorial sum amplifier (AD538), where the vectorial sum is calculated (see Figure 3.3):

$$R = \sqrt{X^2 + Y^2} = V_{sig} \tag{3.3}$$

This computes a signal R. It can be seen that when $Y = 0$, this implies $\theta = 0$. Therefore, the X component of the signal becomes equal to the R (Figure 3.3). As a result, R is a measure of the changes in cantilever amplitude and not affected by the changes in phase.

The phase difference (θ_{error}) between the cantilever signal and reference can be computed by:

$$\theta_{error} = sin^{-1}\left(\frac{Y}{R}\right) \tag{3.4}$$

$$\approx \frac{Y}{R} \text{ for } \theta \ll 1$$

In conclusion, as shown by the block diagram in Figure 3.5, the lock-in amplifier uses the cantilever and reference signals to output a signal R which corresponds

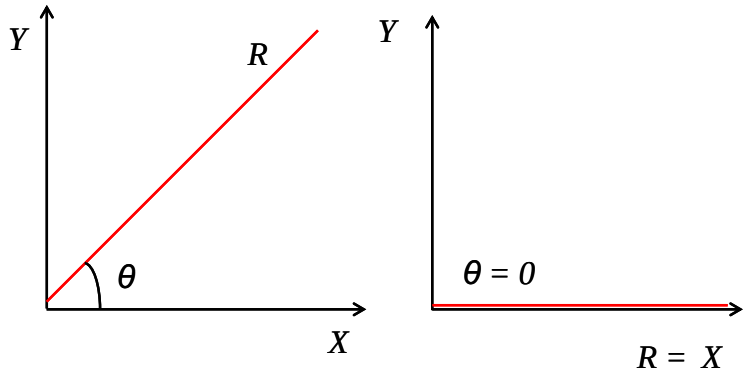

Figure 3.4.: Vector representation of X and Y components of the cantilever signal. When phase difference $(\theta) = 0$, Y equates to 0 as X equates to R.

to the cantilever signal amplitude. This signal is used in the amplitude controller (further explained subsection 3.2.4). Secondly, the lock-in amplifier outputs a signal Y which is used in a phase locked loop (PLL) to maintain a phase difference of 0 in the frequency detector.

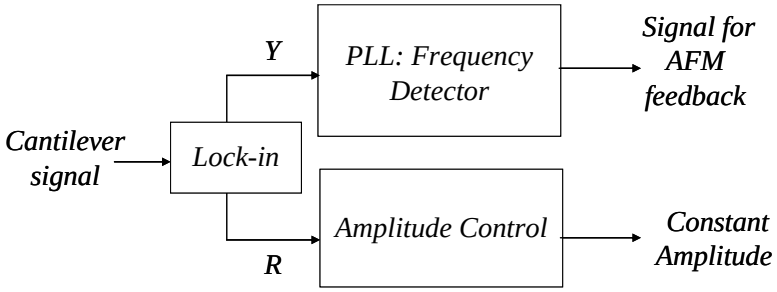

Figure 3.5.: Block diagram of the Y and R outputs of the lock-in amplifier used in the frequency detector and amplitude controller respectively.

3.2.3. Phase locked loop/Frequency Detector

The phase difference between two signals can only be continuously zero if their frequencies are equal. The frequency detector tracks the frequency signal by means of a phase locked loop (PLL). A PLL is used to adjust the frequency of a reference signal to that of the signal, thus keeping the phase difference zero.

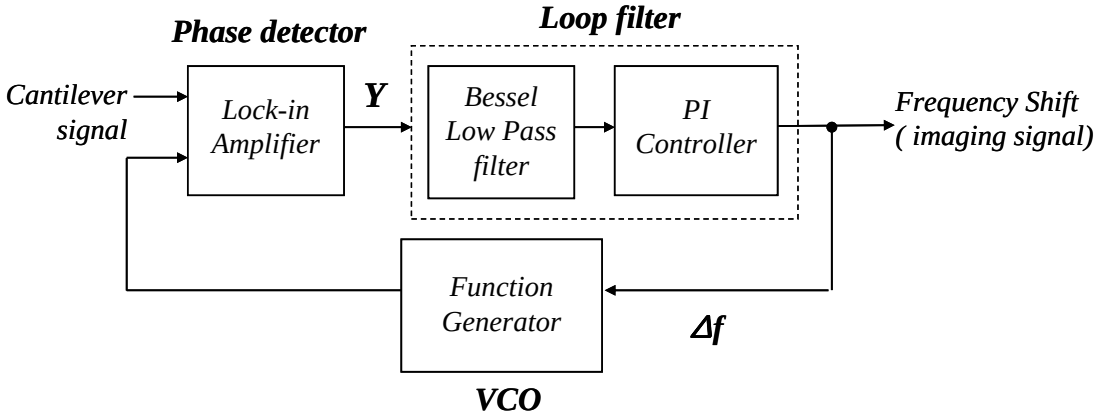

Figure 3.6.: Block diagram of the basic components of the phase lock loop in our FM AFM.

The basic components that make up a PLL are a phase detector, loop filter and a voltage controlled oscillator. A phase detector determines the phase difference between the input signal and a reference oscillation that is generated by a voltage-controlled oscillator (VCO). A loop filter is used to remove any unwanted higher-frequency components that result from this mixing. After filtering, the measured phase difference is passed to a VCO to nullify the error by adjusting the frequency of the reference signal. Therefore, this feedback loop keeps the phase difference between the input and reference signals constantly zero, which is referred to as being 'in lock'.

Figure 3.6 shows the PLL in our experimental set-up. The VCO is a function generator (Yokogawa FG220/R1, 1 μ Hz–15 MHz). The phase detector is our home-built lock-in amplifier. The loop filter is composed of a Bessel low pass

filter (SRS SIM965) and a proportional-integral (P-I) controller (SRS SIM960, with internal set point 0).

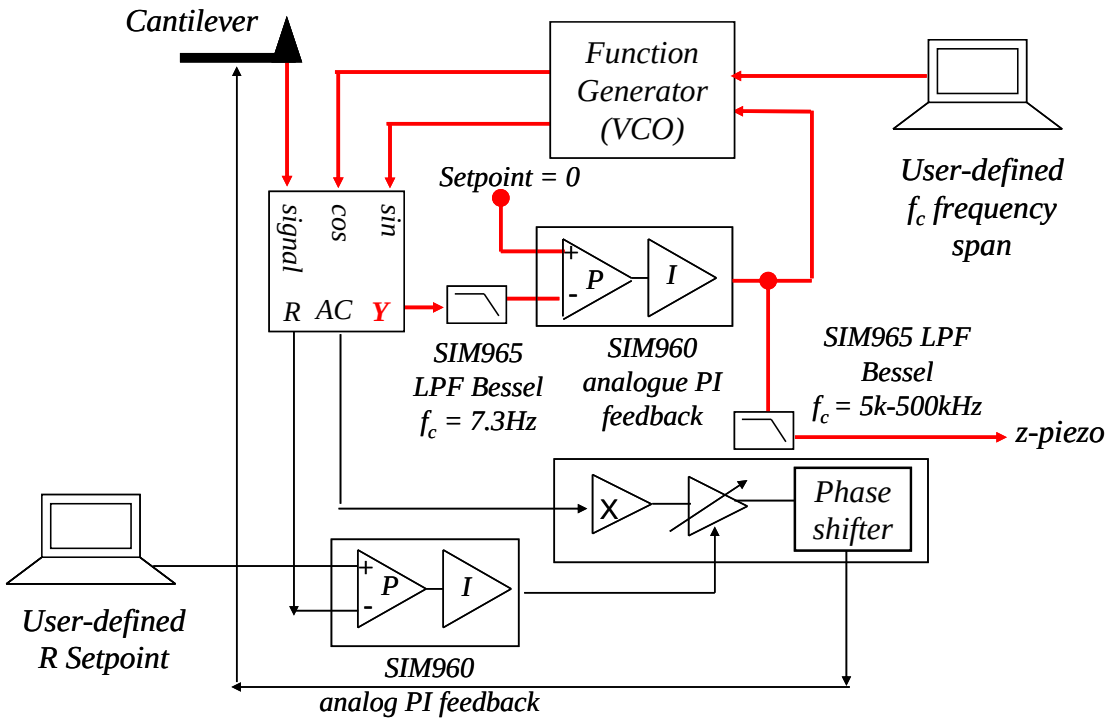

Figure 3.7.: Detailed circuit diagram of frequency detector and amplitude controller.

This PLL is the frequency detector (shown by red path in Figure 3.7) in our experimental set-up. Signal Y from the lock-in amplifier is passed through an external second order Bessel low pass filter (LPF) with maximum characteristic frequency $f_s = 500$ kHz (further explained in subsection 3.3.4). This leaves the required DC component of the signal which is proportional to the difference between the reference signal frequency and cantilevers shifted frequency ($f_0 + \Delta f$). The filtered Y output is passed through a digital proportional-integral (Y-PI) feedback control (SRS SIM960, Sunnyvale, CA). This Y-PI control station is set with an internal set-point of 0. As mentioned in subsection 3.2.3, when $Y = 0$, $X = R$, hence any shift in the cantilever resonance frequency (Δf) results in Y

output voltage $\neq 0$. This error signal passes to the function generator (VCO) which converts the error from a DC voltage into the corresponding Δf in Hz. This is achieved by inputting a centre frequency that corresponds to cantilever f_0, into a user-made PLL LabVIEW interface. Along with this, a frequency span (usually ± 5 kHz) is also defined, which corresponds to the ± 10 V limits of the P-I feedback controller (Y-PI). The Y-PI displays the frequency shift in volts and the PLL LabVIEW interface translates the corresponding number of volts per hertz, since the voltage equivalent of the frequency span is ± 10 V. This calibration can also be used to convert the volts against z-piezo displacement (z) graph produced during the cantilever-sample approach, into a frequency shift against z-piezo displacement graph. Frequency shift (Hz) can then be translated into force (N) using formulas derived by Sader et al [38].

This Δf is also fed to the z-piezo, which is used as the AFM feedback signal. In this set-up, a commercial Multimode microscope base (Bruker AXS Corp., Santa Barbara, USA) is used with a Nanoscope III controller. The Δf signal is connected through a signal access module (SAM) to regulate tip-sample distance via the z-piezo scanner.

3.2.4. Amplitude controller

As mentioned, signal R of the lock-in amplifier is used in an amplitude controller in order to maintain a constant cantilever oscillation amplitude. As shown in Figure 3.7, signal R is fed into a PI feedback loop (R-PI) and customised LabVIEW software is used to input the desired amplitude set-point (in nm). This sets the internal set-point of the R-PI. If the cantilever amplitude differs from the user defined set-point amplitude, the resulting difference/error signal (in volts) is passed to a home-built excitation circuit. The cantilever signal from the lock-in amplifier (see Figure 3.7) is also passed into the excitation circuit, where it is 90^{o} phase shifted then multiplied by the error signal via an analog multiplier. A phase-shifter dial on the excitation circuit is used to ensure a 90^{o} phase difference between the actuator and the cantilever signal. This 90^{o} phase shift implies that

the actuator provides a push at the point when the cantilever is at the point of maximum velocity. This phase shift can be manually adjusted by monitoring the amplitude of the cantilever oscillation until the maximum value is found at the cantilevers resonance frequency.

The output of the excitation circuit (referred to as the drive voltage) is then passed to the cantilever actuator. In this set up, piezo-actuation is used to actuate the cantilever. The cantilever is mounted on a piezo-crystal, held in a specially designed cantilever holder[2]. The cantilever is secured into place using a small amount of silver paint (Agar), where the back of the cantilever support chip is in contact with a piezo crystal. The driving voltage causes the piezo crystal to expand or contract. As a result, the actuator adjusts the cantilever oscillation to establish the desired amplitude. This is referred to as self-excitation mode, in which the cantilevers own signal is fed back as an excitation signal and requires no need for an external signal generator. Furthermore, the driving voltage required to keep the oscillation amplitude constant is proportional to dissipation energy. Since it is monitored accurately and independently this signal can also be used as an imaging signal if desired.

A LabVIEW interface is also used to plot the cantilever amplitude against the (user-defined) frequency span. When actuated, other resonances are also detected in the resulting spectrum, which originate from the complicated acoustic spectrum of the fluid cell and can obscure the true cantilever resonance. To remove these unwanted resonances the excitation signal feed to the actuator, is phase shifted by 90º to ensure the cantilever is driven most efficiently. In addition, this signal is band pass filtered around the cantilever resonance. Also, in our set-up it was found that when using PPP-NCH cantilevers, a spurious resonance at 120 kHz was always found. Therefore, cantilevers of resonance greater or less than 120 kHz was used to avoid these perturbing peaks [78].

[2] Instrumentation for cantilever detection is described in Chapter 4

3.2.5. Tuning the loop filter of the PLL[3]

The detection bandwidth of the frequency detector is dependent on the settings on the LPF [12], which are described below. The same procedure can be applied to any PLL with a similar block diagram as that shown in Figure 3.6.

The input and out signals of the PLL can be related by its transfer function $H(s)$ [79]:

$$H(s) = \frac{\phi_{out}}{\phi_{in}} \tag{3.5}$$

A PLL is characterised by its 'order', which is determined by the highest power of the polynomial expression in the denominator of the transfer function. The order of a PLL can also be determined by the order of the loop filters within it. If there is no filter the PLL is classified as a 1st order PLL. In our set-up, a 2nd order LPF filters the *2f* signal from the output of the lock-in amplifier. In addition, there is a first order LPF within the electronics of the frequency/phase detector (shown in Figure 3.3). Therefore, this classes our PLL as a fourth order PLL.

If the external second order LPF is ignored and our PLL is referred to as a second order PLL, the detected frequency shift Δf is defined by [12, 79]:

$$\Delta f(s) = \frac{P}{s}\frac{1 + s\tau_i}{s\tau_i}\theta_{error}(s) \tag{3.6}$$

where θ_{error} is the phase difference, s is the complex frequency $s = i\omega = i2\pi f$, P is the proportional gain and τ the integration time constant of the P-I feedback. The cut-off for detection ($f_{PLL,3dB}$) can be found using the following relationship

[3]The equations in this section were used by my supervisor Dr Bart Hoogenboom to calculate the parameters required for Test 4 in subsection 3.3.4. This was performed whilst I was absent on maternity leave.

[12, 79]:

$$f_{PLL,-3dB} = f_n\sqrt{1+2\zeta^2+\sqrt{(1+2\zeta^2)^2+1}} \tag{3.7}$$

where f_n is the natural frequency and ζ a dimensionless damping coefficient. In order to determine the parameters to input in our P-I controller for the required cut off, the following two equations were used [12, 79]:

$$P = \frac{\pi\zeta f_n}{90} \tag{3.8}$$

$$\tau_i = \frac{\zeta}{\pi f_n} \tag{3.9}$$

If the 2nd LPF is taken into account, this classifies the set-up as a fourth order PLL. Therefore, the proportional (P) and integral time constant (τ_i) parameters required for the frequency detector P-I feedback settings can be determined theoretically using equations Equation 3.10 and Equation 3.11 [79],

$$P = \frac{\pi f_T}{180} \tag{3.10}$$

$$\tau_i = \frac{1}{2\pi f_T} \tag{3.11}$$

where f_T is the transition frequency where the open-loop gain is 1. To determine f_T, the equation for open-loop gain is given by:

$$f(s) = \frac{P}{s} \frac{\omega_s^2}{s^2 + 2s\omega_s\zeta_s + \omega_s^2} \frac{1 + s\tau_i}{s\tau_i} \theta_{error}(s) \tag{3.12}$$

$$f_s = 5f_T \tag{3.13}$$

where $\omega_s = 2\pi f_s$ is the natural frequency and ζ_s the damping coefficient of the second order filter, where quadratic part of the denominator describes the transfer function of a 2nd-order filter. The value of the damping coefficient influences the stability of PLLs response to changes in the frequency signal. The damping coefficients tested in our set-up were; $\zeta = 1/\sqrt{2}$ for a Butterworth-like response, $\zeta = \sqrt{3/2}$ for response of a Bessel filter and $\zeta = 1$ for critical damping [12, 79] and are further discussed in section 3.3.

3.3. Tests

The following describes various tests carried out to characterize the FM AFM frequency range, its modulation bandwidth for amplitude/phase and its step-response.

3.3.1. Test 1: Bandwidth of frequency detection

This FM AFM frequency detector was initially tested to demonstrate its wide bandwidth of frequency detection. Since the set-up is designed for the detection of small cantilevers, the frequency detection range must extend up to the MHz range.

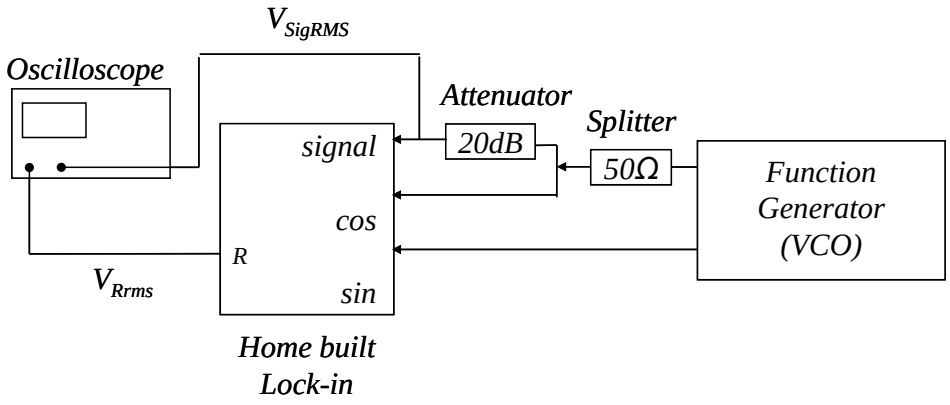

Figure 3.8.: Block diagram of set-up used to measure the amplitude of signal R as a function of frequency.

As illustrated in Figure 3.8, a test input signal, V_{sigRMS}, was provided to the input of the lock-in amplifier to mimic a cantilever signal. To demonstrate the wide bandwidth capability of the frequency detector, the frequency of the input signal was increased and its corresponding amplitude signal (R) was measured. Two reference signals were provided to the input of the lock-in amplifier; a sinusoidal signal of amplitude 1.14 $V_{rms}$and a cosine wave of 2.28 V_{rms}. The second reference signal was split and 20 dB attenuated to be used as the input signal in place of a cantilever. The frequency of the input signal (V_{sig}) was gradually increased and resulting amplitude signal (R) was measured. Within the lock-in amplifier, internal amplifiers multiply the amplitude of the R signal by a gain (a). This can be expressed as follows:

$$R = \alpha V_{sigRMS} \tag{3.14}$$

Therefore, for accurate calibration purposes, this test was also performed to verify this gain. The plot shown in Figure 3.9 demonstrates that our frequency detector can detect oscillations over a frequency range of 40 kHz–15 MHz. This is higher than the range of frequency detectors in most commercial AFM controllers. The lower-frequency cut-off is due to a high-pass filter at the input signal and the

higher-frequency of 15 MHz is limited by the maximum output frequency of the function generator being used. In addition, for calibration purposes these results show that with increasing input frequencies, the gain computes to approximately 15 in the present circuit configuration.

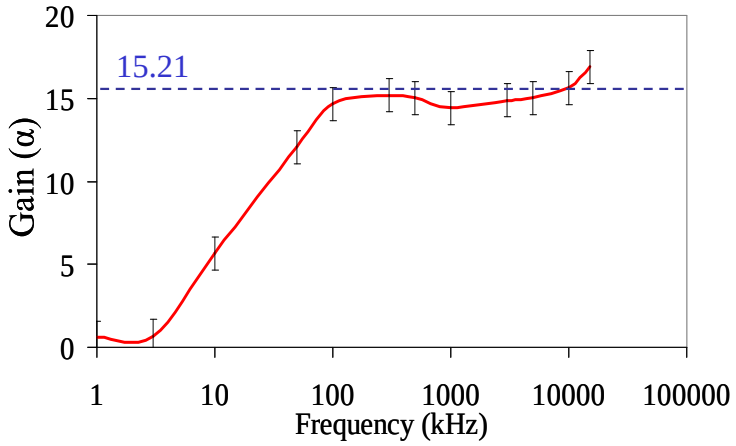

Figure 3.9.: Amplitude signal gain (α) as function of increasing input signal frequency.

3.3.2. Test 2: Bandwidth of phase detection

Figure 3.10 shows the set-up used to measure the bandwidth of phase modulation. The cosine reference signal and input signal were phase-modulated via an external analog modulation input of the function generator, causing a sinusoidal reference signal to effectively become out of phase. Modulation frequencies up to 100 kHz were used.

The Y (Δf) output signal was low pass filtered at natural frequency f_s of the second order Bessel filter at 5 kHz, implying a 3 dB cut-off ($f_{s,-3\ dB}$) of 4 kHz. The corresponding shift in the Y was measured. The constant amplitude of R was also monitored. This was repeated for f_s = 50 kHz and 500 kHz. implying 3 dB cut-offs of the Bessel filter of $f_{s,-3\ dB}$ = 40 Hz, and 400 kHz, respectively.

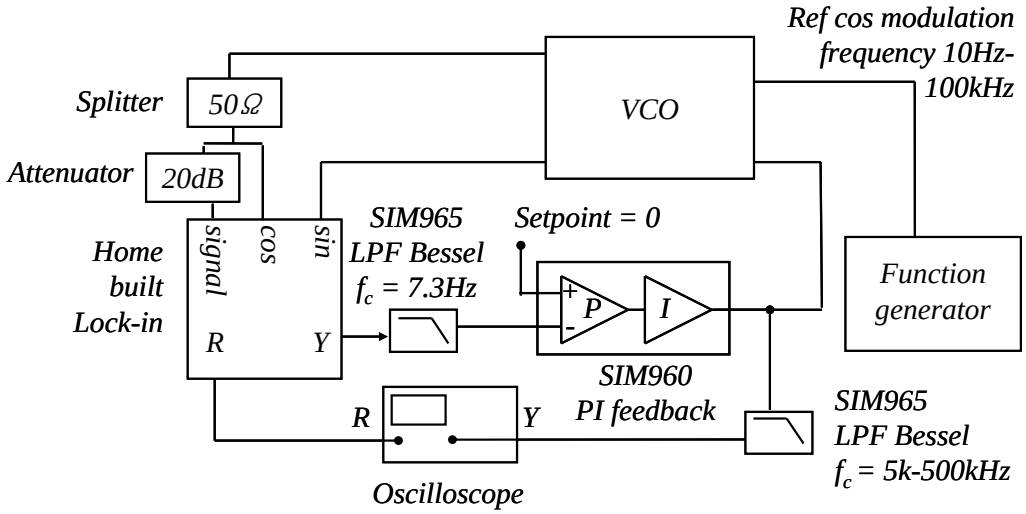

Figure 3.10.: Test 2 Block diagram of set-up used to measure bandwidth of phase modulation.

The results for this test are shown in Figure 3.11, where the Y/R is plotted as a function of increasing modulation frequency. The measured cut-offs for the phase detector were 4, 34, and 68 kHz for the settings which were tested. As shown by the graph, the speed of phase detection is only limited by the time-constant selected in the Bessel LPF, i.e. the phase/amplitude cut-offs corresponds to the f_c set by the LPF. Therefore, for low frequencies up to 40 kHz the modulation bandwidth of phase detection is only dependent on the LPF.

Note the measure at $f_s = 500$ kHz begins to fall off before the expected cut off point. This is due to the 70 kHz cut-off in internal LPF of the function generator. This implies that for higher frequencies, the phase detection is only limited by the modulation bandwidth of the function generator. The phase detection limit could be increased by replacing the current VCO with a function generator with a higher cut off frequency.

3.3.3. Test 3: Centering at cantilever signal

The cantilever input signal will contain a small magnitude of noise that will also be multiplied by the reference signal in the lock-in amplifier. The phase of the incoming noise does not have a relation to the cantilever phase nor does it have

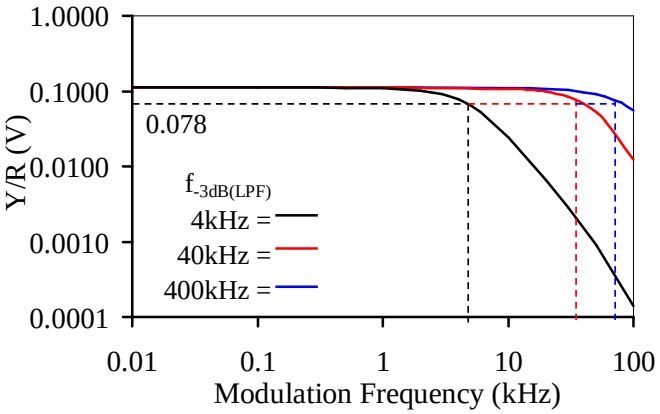

Figure 3.11.: Bandwidth of phase detector for Bessel low pass filters 5 kHz, 50 kHz and 500 kHz

a fixed frequency related to the cantilever. Therefore, in principle it would not affect the mean DC output being measured. Hence, any noise at frequencies near the cantilever resonance can be attenuated via the LPF.

Test 3 demonstrates the ability of the phase detector to single out the cantilever frequency, and measure its amplitude whilst noise at any other frequencies is rejected. Figure 3.12 shows a block diagram of the set-up used for this test. To begin with, the thermal noise signal of a cantilever with resonance frequency 298 kHz was measured. Centre frequencies around the cantilever resonance frequency were inputted whilst

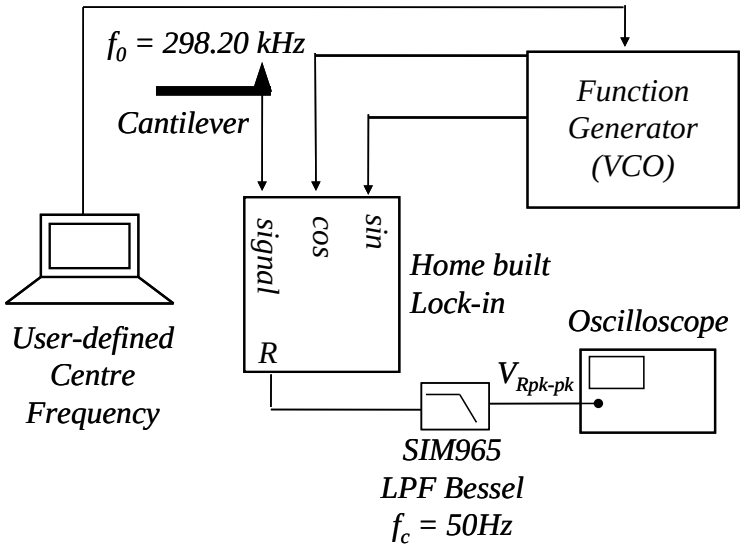

Figure 3.12.: Block diagram of experimental set-up used to measure amplitude of signal R as a function of center frequency

measuring the amplitude of the R signal, with a low pass filter cut-off of $f_c = 50$ Hz. As shown by Figure 3.13, the maximum amplitude of the signal R was found at 298.20 kHz, whilst the amplitudes at other frequencies around the resonance are attenuated to almost zero.

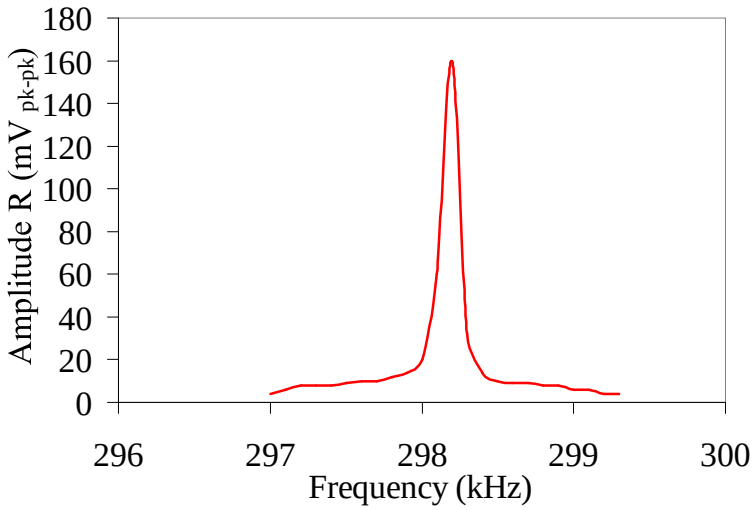

Figure 3.13.: Amplitude of signal R as a function of centre frequency for a cantilever of resonance 298.20 kHz

3.3.4. Step response of frequency detector [4]

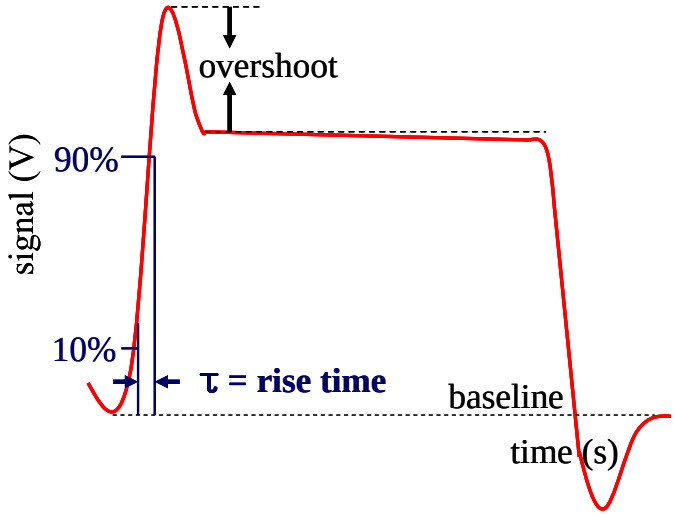

Figure 3.14.: A signal (V) changing from a low value to one higher. Image depicts how the rise time is measured from when the signal rises from 10% to 90% of its value. Image adapted from[11].

When a PLL encounters a frequency shift in the input signal, the speed at which it responds to rectify this change is referred to as the speed of step response. This speed of response is dependent on the settings of the filter within the PLL. As illustrated in Figure 3.14, the speed of step response is determined by the rise time of response, which is defined as the time taken for the signal to go from 10% of its original value to 90%. Albrecht et al [43] demonstrated the rise time of response of the very first FM AFM frequency detector, which was found to be 16 ms. Similarly, the step response of our frequency detector was tested using varying P and I settings on our PLL.

A signal of amplitude 100 mV_{rms} and 100 kHz frequency from a commercial lock-in amplifier (reference channel of an SRS830 lock-in amplifier) was provided to the input of the lock-in amplifier. The signal was set to change in steps of 10 Hz. The proportional (P) and integral time (τ_i) parameters of the PLL were calculated according to the PLL theory described in subsection 3.2.5. Since the

[4]The data described in this test were collected by my supervisor Dr Bart Hoogenboom during my absence on maternity leave.

PLL in this set-up can be described as a fourth order PLL with a second order LPF between the lock-in amplifier and P-I feedback, equations Equation 3.10 and Equation 3.11 were used to find the values of P and τ_i using varying values for the damping coefficients.

	Second order PLL			
	$\zeta = 1$	$\zeta = \sqrt{3/2}$	$\zeta = 1/\sqrt{2}$	Fourth order PLL
P [Hz/deg]	14.1	13.3	12	13.1
τ_i[ms]	0.790	0.628	0.463	0.212
f_s[kHz]	∞^a	∞^a	∞^a	3.76

The calculated P and τ_i parameters are shown in the table above, which were set in a user-made LabVIEW interface. Figure 3.15 displays the resulting step responses for each of the calculated parameters (Figure 3.15). It can be seen that the smaller the value of the damping coefficient, the larger the resulting overshoot. Notice that the vertical axis shows that the overshoot becomes more apparent when 4th order settings were used. For the set-up, it was found that 2nd order parameters produced acceptable step response without instabilities, when $f_s \geq 5f_{PLL,\text{-}3dB}$.

Next the step response was measured and compared to a commercial frequency detector (Nanosurf Easy PLL, Liestal, Switzerland). A signal of 100 mV_{rms} amplitude and 10 MHz frequency from a BK Precision rf signal generator (2005B, Yorba Linda, CA) was provided to the input of our home-built frequency detector. The P-I feedback rise time was measured after applying sudden offsets on its output and is shown in Figure 3.15 (c). The rise time measured was 13 µs in comparison to the commercial Nanosurf frequency detector with a response time of 600 µs.

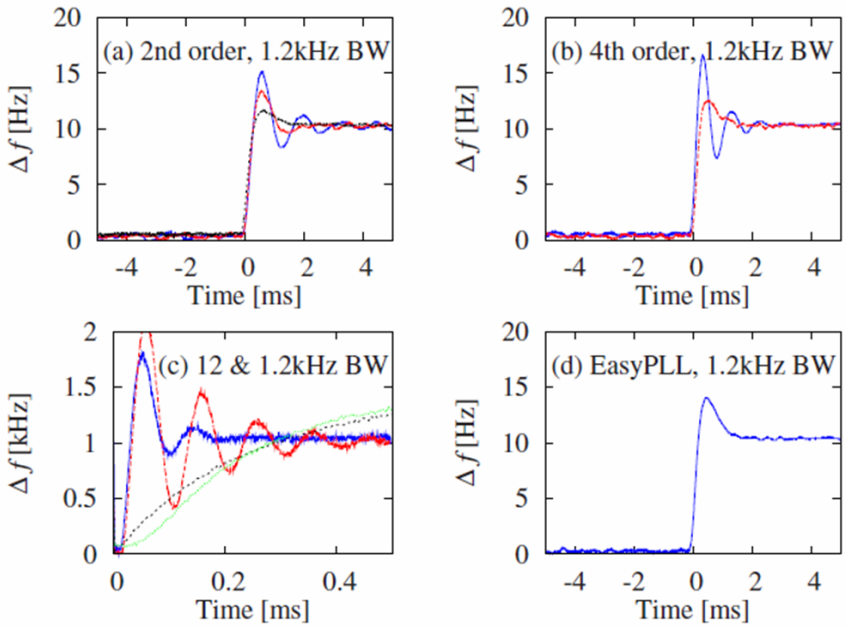

Figure 3.15.: Frequency step-response. (a) Second order PLL with $f_{PLL,-3\ dB}$ = 1.2 kHz, for $\zeta = 0.3$ (solid line), $\zeta = 0.5$ (dashed), $\zeta = \sqrt{3}/2$ (dotted). (b) Fourth order PLL with theoretical settings (solid) and with second-order settings for $\zeta = \sqrt{3}/2$ and $f_s = 5f_{PLL,-3\ dB}$ (dashed). (c) Second order settings for $\zeta = \sqrt{3}/2$ and $f_{PLL,-3\ dB} = 12$ kHz, with $f_s = \infty$ (solid) and $f_s = 5f_{PLL,-3\ dB}$ (dashed), compared to the equivalent $f_{PLL,-3\ dB} = 1.2$ kHz settings (short dash and dotted). (d) Step-response of a commercial frequency detector Nanosurf Easy PLL [12].

3.4. Conclusion

In conclusion the detection range of our FM AFM was tested demonstrating its ability to detect frequencies from 40 kHz to 15 MHz. This upper range is currently only limited by the internal LPF of the function generator, which can easily be upgraded to increase the higher frequency detection range. The fast amplitude and phase detection was tested and proved to be only limited by the modulation bandwidth (70 kHz) of the function generator that provided the test input signal. In addition, the frequency detectors response time to offsets was found to be 13 µs.

4. Fabry-Perot Interferometric Cantilever Detector[1]

4.1. Introduction

Viscous damping of the cantilever oscillations reduces the force sensitivity in liquids. This can be compensated by oscillating the cantilever at small amplitudes (0.1 - 3 nm). This increases sensitivity to short-range forces and hence increased spatial resolution. To achieve this, the small interaction forces causing microscopic displacements of the cantilever must be precisely monitored. These microscopic changes must then be transformed into measurable macroscopic outputs. To achieve this, high cantilever signal-to-noise ratios are required along with a cantilever deflection sensor sensitive to these microscopic displacements.

The following chapter describes the experimental set-up of a low-noise Fabry-Perot interferometric cantilever detector, which yields fm/√Hz sensitivity over a 10 MHz bandwidth [14], making it especially suitable for applications in liquid [16]. This interferometric cantilever detection system is designed for detecting the small amplitudes ($\geq$ 0.1 nm) oscillations of small dimension cantilevers (25 - 35 x 4 x 0.2 μm^3 (l x w x t)) of high resonance frequencies (MHz) as well as standard commercial cantilevers (kHz). It produces a laser spot size of 3 µm and has a safe working distance of 0.9 mm between the optics and the cantilever. It consists of piezo-motors for a three-axis alignment and is $\pm 10°$ tolerant against angular misalignment.

[1] This interferometer is a (slightly modified) copy of a system which was earlier brought to work in Basel, Switzerland. The alignment motor in our interferometer was assembled by B. Bircher [13]. I was then involved in assembling the interferometer optics and testing the stability of the set up. This included testing rf modulation and vibration isolation.

Prior to the results shown in this thesis, the interferometer had not been used for AFM imaging since factors such as mode hopping, mechanical noise and optical interference were creating instabilities in the interferometer signal. To obtain maximum stability, the set-up was isolated against mechanical noise and tests were carried out to measure the effectiveness of insulation. In addition, the parameters of laser diode temperature, laser diode current and radio frequency (rf) modulation were varied to find settings which provided optimum stability in the interferometer signal. Finally, thermal noise spectra of small cantilevers were measured, to aid a project investigating the effects of adsorbate mass on cantilever resonance. A bi-metallic heat effecting effect encountered during these measurements, is also discussed.

4.2. Interferometry versus beam deflection

Several methods can be used to detect the position of the cantilever in AFM. Due to the simplicity of its set-up and ease of use, most commercial AFMs use beam deflection (BD). In this technique, a laser beam is aligned above the cantilever and the reflected laser spot is angled to fall on a four-quadrant photodiode via an adjustable mirror. As the cantilever becomes deflected due to tip-sample interactions, the spot shifts position with respect to the four quadrants and the cantilever position can therefore be tracked. To achieve this, first the laser-spot is aligned onto the cantilever tip. Following this, the reflected laser-spot must then be accurately aligned onto the centre of the four-quadrant photodiode. Therefore, the cantilever deflection is a measure of an angle. Although, BD can be used to track the position of commercial cantilevers, it is not suitable for detecting small amplitudes of reduced dimension cantilevers. To use BD with small cantilevers, the laser spot diameter must also be reduced and focused on to a narrow 3 μm width cantilever. This reduced spot size would result in a large reflected optical opening angle off the cantilever onto the photodiode detector. Hence, this would reduce the sensitivity of any changes in the angle of the deflected beam [16, 80].

Fibre-optic interferometry was first implemented with AFM in 1989 by Rugar et al [81] and since then the technique has been developed to detect microscopic cantilever deflections with high precision. Interferometric cantilever detection

(ICD) has several advantages over BD. To begin with, the cantilever position only requires one alignment step to position the laser optics above the cantilever. It is a quick and accurate aligning method that relies on the intensity of the reflected laser signal to ensure precise alignment (further explained in section 4.4). This is in comparison to beam deflection where the alignment of the laser-spot is judged by eye. For small cantilevers, the lens system is designed to focus the laser spot down to a diameter of 3 µm and small amplitude oscillations (down to 0.1 nm) can be tracked.

A disadvantage of the ICD method is that it has a limited linear range and it is complicated to set-up since it consists of delicate optics which require intense care and stabilising. For this reason, ICD is not yet commercially available.

4.3. Principle of Fabry-Perot interferometry

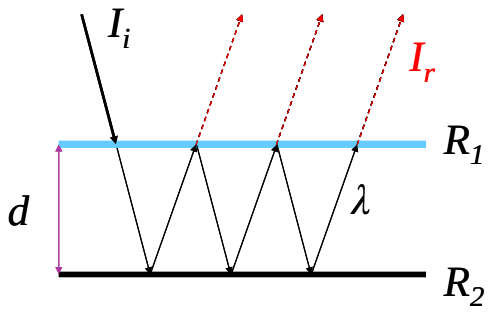

Figure 4.1.: Schematic diagram depicting the principle of Fabry-Perot interferometry. The diagram shows two surfaces; one reflective (R_2) and one partially reflective surface (R_2) separated by distance d, between which an incident beam partly reflects and transmits light rays.

The Fabry-Perot interferometer is an optical instrument which uses the multiple reflections between two closely spaced parallel surfaces (separated by a distance d) to produce an interference pattern. One surface (R_2) is reflective and the other partially reflective (R_1). An incident coherent laser beam is partially transmitted each time the light reaches the second surface, resulting in multiple offset beams, which can interfere. This is illustrated in Figure 4.1, where I_i is the incident laser intensity, I_r is the total reflected intensity and λ is the wavelength of the light.

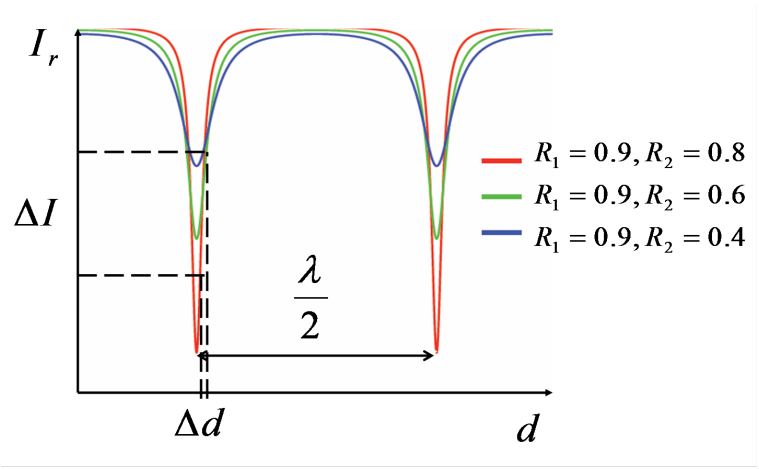

Figure 4.2.: A characteristic interference pattern produced by the interferometer, with peak minima at $\frac{1}{2}\lambda$. The graph shows that by varying magnitudes of reflectivity of surface R_2, this produces peaks of varying finesse. (Image adapted from [13]).

After every reflection, a part of the light exits the cavity and part is reflected back.

Figure 4.2 is a plot of I_r against distance d, which produces an interference pattern consisting of minima peaks at points of destructive interference and maxima at constructive interference, which are both separated by $\lambda/2$. The finesse of these peaks depend on the reflectivity and geometry of the surfaces. If the two reflective plates have similar reflectivities, a higher finesse of the peak minima is produced, where $R_1 = R_2$ would produce the highest finesse.

4.4. Experimental set-up

Figure 4.3 shows a block diagram of the basis of our interferometer set-up. Light from a laser diode (LD) of wavelength 785 nm, is guided through an optical fibre into a 90:10 ratio beam splitter[2]. The LD is operated by a Thorlabs LD controller

[2]Initially, a 50:50 ratio fibre x-coupler was used but it caused severe instabilities in the interfer-

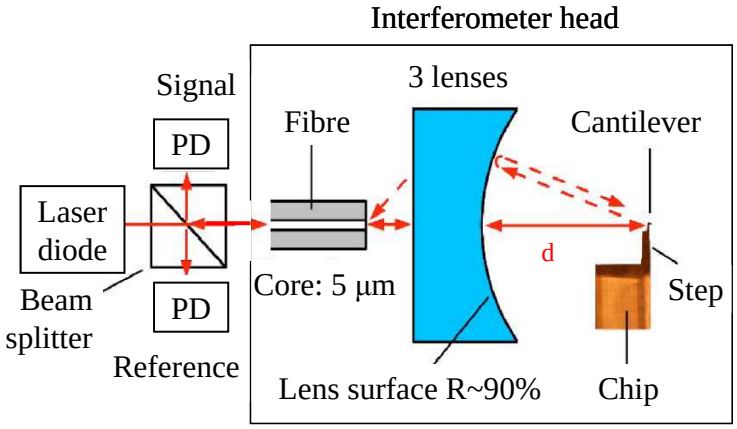

Figure 4.3.: Schematic of Fabry-Perot interferometer optics including the three-lens system and cantilever [14].

capable of producing laser currents up to 100 mA, along with a temperature controller. The beam splitter divides the incident laser light into two branches, where 90% of its intensity is reflected and allowed to pass through to a reference photodiode (PD_{ref}) and 10% is transmitted to the interferometer lens system onto the cantilever. The PD_{ref} is used to monitor the incident intensity.

The Fabry-Perot interferometer head (shown in Figure 4.4) consists of an optical fibre and a three-lens system, designed such that the cantilever acts as one reflective surface (R_2) and a 90% reflective lens is the other (R_1). The curvature of this three lens system has a radius that matches the 0.9 mm perpendicular distance between the lens and the cantilever. This ensures that all light reflected back off the cantilever always follows a path back to the 5 µm fibre core. Furthermore, the laser light is aligned to fall perpendicular to the front lens surface (see Figure 4.3) such that the light does not refract at this interface. Therefore, whilst working in liquid or air, no adjustments in optical alignment are required to account for the change of medium [80]. Reflected light exiting the cavity is guided back through the optical fibre to the beam splitter and on to a signal photodiode (PD_{sig}).

To produce an interference pattern, the interferometer optics are aligned, to ~ 1

ence pattern. This was due to the high amounts of light coupling back into the LD causing mode hopping and optical interference noise. Therefore the set up was reverted back to the set up used in Basel, where a beam splitter is used in place of the fibre x-coupler.

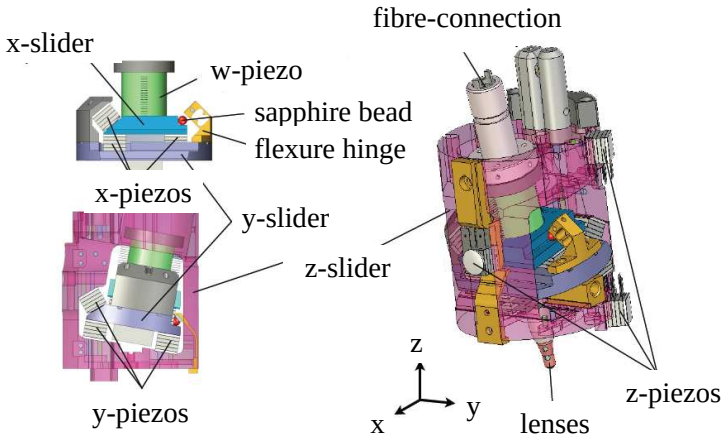

Figure 4.4.: Structure of interferometer head including optics and x, y, z and w-piezos [13].

µm precision, above the cantilever by the use of x, y and z slip-stick motors (see Figure 4.4). An additional piezo stack, referred to as the w-piezo, allows control of the distance between the optics and the cantilever to sub-nanometer accuracy. A sinusoidal signal from the computer is amplified[3] and sent to the w-piezo to vary the distance d between the optics and cantilever over ~ 1.5 times the period of the interference pattern (see Figure 4.5). The reflected intensity I_r , incident on the PD_{sig}, is low pass filtered[4] ($f_c = 2$ kHz) then plotted against this distance d using a user-made Lab-VIEW software. An accurate alignment of the optics is characterised by the presence of a high finesse like that shown in Figure 4.2. In

[3]P-860, Physik Instrumente GmbH Karlsruhe, Germany
[4]SIM965, Stanford Research Systems Inc, CA, USA

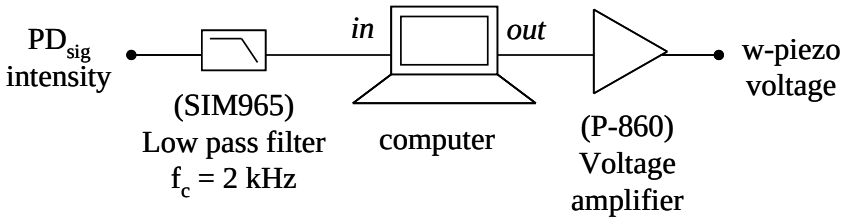

Figure 4.5.: A block diagram of the electronical set up to produce an interference pattern (see text).

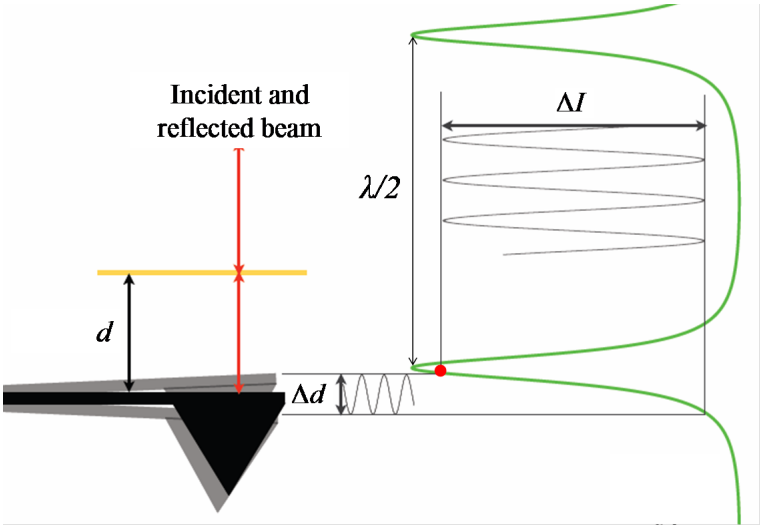

Figure 4.6.: An interference pattern produced by Fabry-Perot interferometer set up with a set-point (red dot) selected on the steepest part of a slope. The image depicts how small changes in distance d result in large changes in the intensity ΔI.

the focal point of the optics, the laser produces a spot size of 3 μm (suitable for small 4 μm wide cantilevers). The optics have been shown to be ±10° tolerant to angular misalignment [14, 80].

In order to measure the thermal noise of cantilever, the PD_{sig} signal is low pass filtered[5] at $f_c = 2.3$ MHz to remove the rf modulation signal and then monitored on an oscilloscope (shown in Figure 4.7). The signal is also fed to a second low pass filter[6] ($f_c = 2$ kHz) before being fed into a PI feed-back loop that is connected to the w-piezo. Using the interference pattern, an intensity set-point is selected on the steepest part of the slope. This is provided as the set-point in a P-I feedback loop via a LabVIEW interface. This feedback maintains the average intensity on the set-point by keeping d constant. Figure 4.6 shows an example of an interference pattern, where small fluctuations in d results in large changes in I_r . Hence, this technique allows picometre variations in the cantilever position to be detected. In addition, when imaging in water, the increased refractive index (1.33) reduces the wavelength to 590 nm, and thus produces a narrower

[5]BLP -1.9+, Mini -Circuits, NY USA
[6]SIM965, Stanford Research Systems Inc, CA, USA

interference pattern with a sharper slope thereby, increasing the sensitivity to small changes in d. The PD_{sig} is then Fourier transformed (FFT) by a digital oscilloscope producing the thermal noise spectrum of the cantilever. This is a plot of noise amplitude versus frequency. Figure 4.8 shows an example of a thermal noise spectra produced by a commercial PPP-NCH silicon cantilever (225 µm x 43 µm x 4 µm (l x w x t)) in air producing a peak resonance frequency of 250 kHz. This signal is referred to as the cantilever signal and can now be applied to set the cantilever into self-excitation mode as described in Chapter 3.

The interference pattern is also used to convert the drive voltage (V) supplied to the actuator (via the amplitude controller) into nm. Since it is known that the interference pattern peak minima are separated by half a wavelength, this distance d can be defined and the corresponding ± 5 V signal from the w-piezo can be calibrated into the number of volts per nanometre (Figure 4.12 (b) shows an example of how the an interference pattern is displayed on the Labview program.).

As shown in Figure 4.9, the ICD head is designed to fit a commercial Bruker AXS Multimode AFM scanner and base. The scanner is controlled via the Bruker AXS Nanoscope III controller, where the frequency shift imaging feedback signal is provided to the input of a signal access module. The fluid cell is designed with channels for inserting fluid, which immerses both the sample and cantilever in the liquid. The cantilever is glued (with silver paint) on a piezo-actuator, where

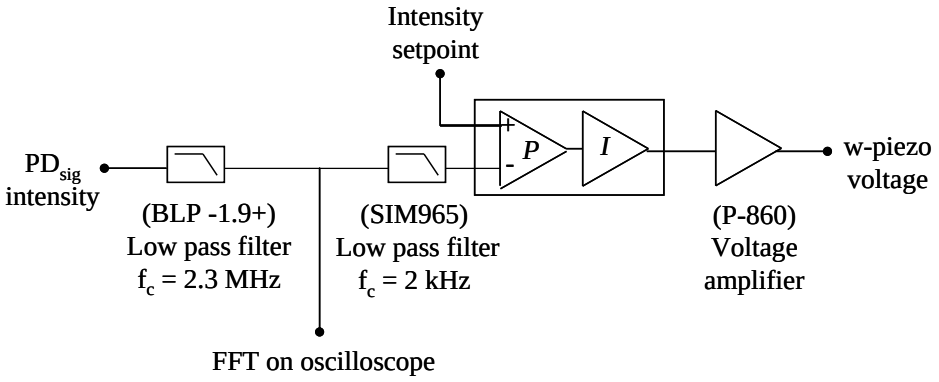

Figure 4.7.: A block diagram of the electronical set up to produce a thermal noise spectrum of cantilever (see text).

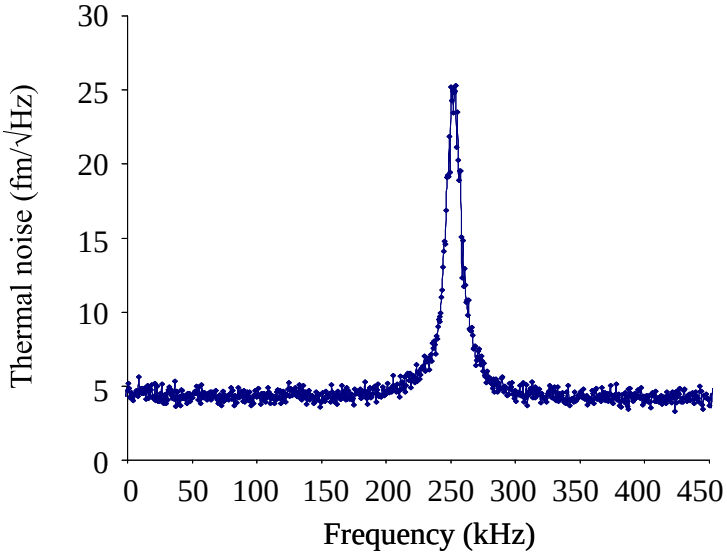

Figure 4.8.: Thermal noise of a PPP-NCH (dimensions 225 µm x 43 µm x 4 µm) 250 kHz cantilever in air, measured using interferometric cantilever detector with a noise floor of 5 fm/√Hz.

the back of the cantilever support chip is in contact with the piezo actuator.

4.4.1. Detecting cantilever deflections in liquid

Thermal noise and quality factors

To achieve high resolution images, high cantilever signal-to-noise ratios (SNR) are required, i.e Q must be high. High Qs can be achieved when the cantilever is operated in ultra high vacuum (UHV) which results in Qs as high as 10^5 compared to 10^2 or 10^3 in air [34]. This increased quality factor narrows the width of the resonance curve resulting in high SNRs. When imaging in liquid, the cantilevers resonance frequency becomes dampened by the viscosity of the surrounding fluid, reducing SNRs. Typically in air, the cantilevers thermal noise peak can be seen clearly above the noise floor of the detector system. If the cantilever detection system has a particularly high noise floor, in liquids the amplitude of a cantilevers thermal noise is so thoroughly reduced that it becomes difficult to decipher at all.

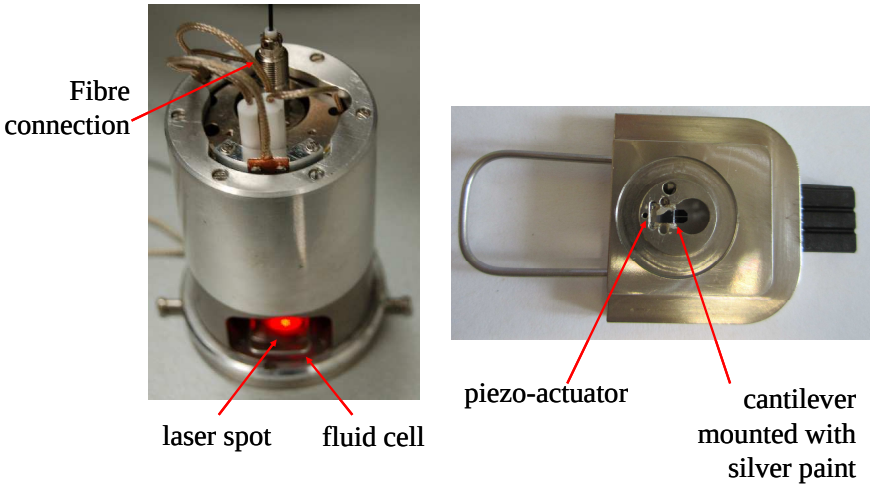

Figure 4.9.: Interferometric cantilever detector head (left) and fluid cell with a mounted cantilever (right).

For example, Figure 4.10 shows the thermal spectra of a standard sized cantilever of resonance 280 kHz (in air), measured using BD in a commercial Bruker AXS Multimode AFM. Commercial AFMs typically possess noise floors from a few 10 to 100 fm/$\sqrt{\text{Hz}}$. As shown in the figure, the noise floor of the Multimode is approximately 100 fm/$\sqrt{\text{Hz}}$, (shown by the base of green line) and the cantilever thermal noise peak is difficult to distinguish even in air. The noise floor of the Fabry-Perot ICD used in this set-up, is also shown in Figure 4.10 (red line). It shows a noise floor of a mere 5 fm/$\sqrt{\text{Hz}}$ at high frequencies (origins of this noise are further explained in subsection 4.4.2). In the Multimode system, once the cantilever is immersed in liquid, the thermal noise of the cantilever becomes entirely hidden, making it very difficult to track. Figure 4.11 shows an example of the thermal noise spectra of the same cantilever of 280 kHz frequency in air and Q of 220 measured using our ICD. When immersed in liquid the cantilever resonance frequency becomes reduced to 136 kHz in water (shown by green curve) and its Q is reduced to 5. However, since the overall noise floor of this ICD system is as low as 5 fm/$\sqrt{\text{Hz}}$, the cantilever peak can clearly be seen, despite the low Q, demonstrating suitability of this technique for use in liquid.

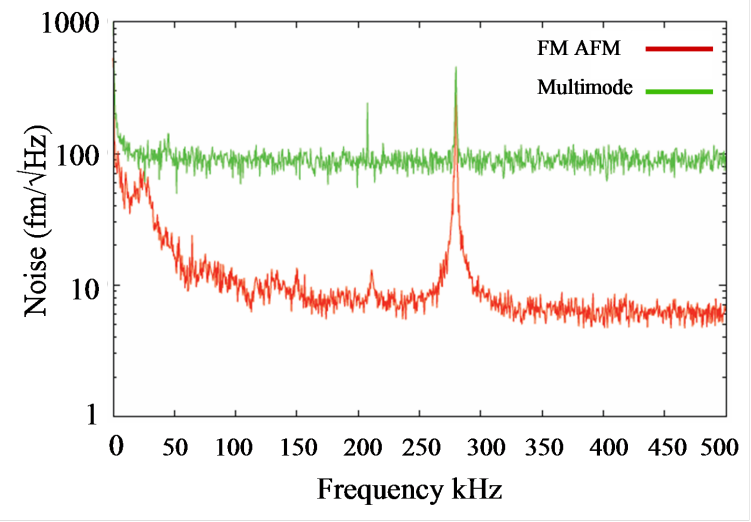

Figure 4.10.: A thermal noise spectra of a standard (129 x 28 x 4μm^3) cantilever measured in air with our FM AFM using interferometric cantilever detector (red) and commercial Multimode AFM (green). The thermal noise floor of the Bruker AXS Multimode AFM is ≈ 100 fm/√Hz compared to the noise floor of the interferometer set-up at 5 fm/√Hz [13].

4.4.2. Origins of noise and noise reduction

The key contributors to the noise in the ICD set-up originate from (a) the laser diode (b) the photodiodes and (c) the optical fibres.

(a) Mode hopping

Laser diodes (LD) under certain conditions can rapidly switch wavelengths. This is known as mode hopping and can occur due to instabilities in temperature and laser current. When mode hopping occurs, many wavelengths are emitted spontaneously. Since a typical plot of the relationship between the temperature (T) and wavelength of the LD output has a characteristic stair-step pattern, a slight deviation in temperature can result in a switch in the emitted wavelength. This can be seen as fluctuations in the output intensity on the PD_{ref} (see Figure 4.12). Mode hopping may be avoided by ensuring the temperature of the LD is controlled. By testing the effect of varying temperatures, the laser diode was found

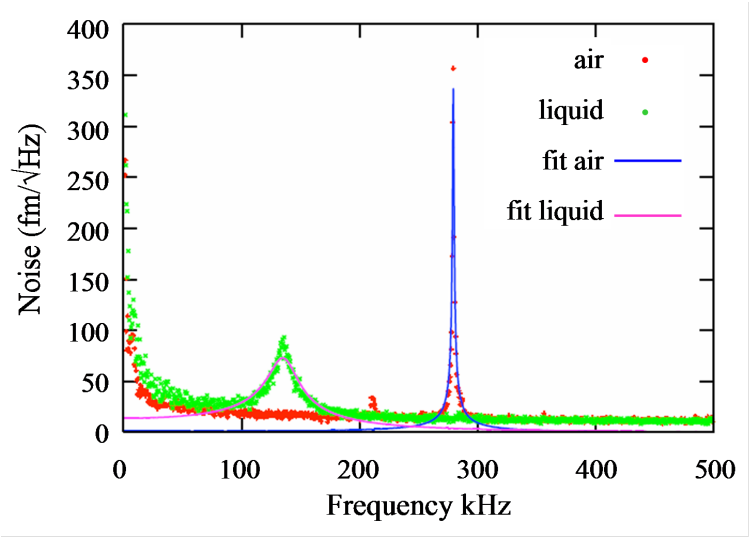

Figure 4.11.: A thermal noise spectra of a standard (129 x 28 x 4μm^3) cantilever measured in air and in liquid. The cantilever resonance frequency in air is 280 kHz and Q: 220 which, when measured in liquid, reduces to 135kHz and 5 respectively. The solid curves correspond to harmonic oscillator motion [13].

to be most stable at temperatures between 24.7 - 25°C at a current of 99 mA.

(b) Optical interference noise

Optical interference noise occurs when scattered or reflected light is coupled back to the optical resonator of the LD. This results in another laser oscillation mode leading to mode hopping. To suppress interference noise, the coherence length of the LD can be shortened by modulating the laser current with a radio frequency (rf) signal. This converts the LD from a single mode to multi-mode, which is less sensitive to effects due to competition for possible laser oscillation modes [56]. After several settings were tested, rf modulation proved effective at 10 MHz at 2 $V_{pk\text{-}pk}$ amplitude. Figure 4.12 depicts an example of a interference pattern with and without the presence of rf modulation.

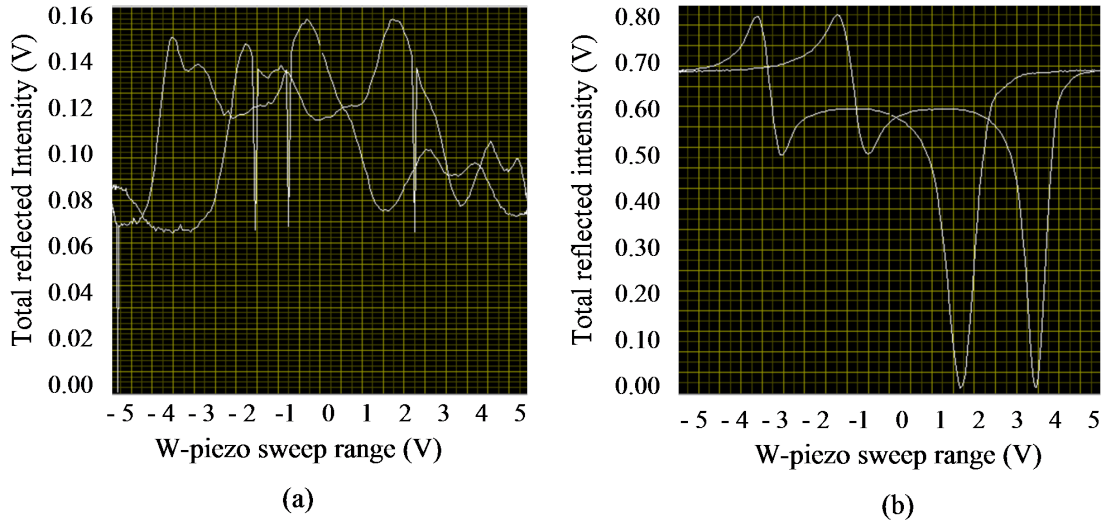

Figure 4.12.: (a) An example of an obscured interference pattern due to mode hopping and optical interference noise. (b) A stable interference pattern produced using rf modulation at f_{mod}: 10 MHz and $V_{pk\text{-}pk}$: 110 mV. Double traces of interference pattern correspond to the forward and back sweeps of the w-piezo.

(c) Johnson and photodiode shot noise

The remaining noise from the photodiodes results in a noise floor of approximately 5 fm/√Hz at high frequencies. Since this noise is intrinsic, it can not be eliminated. This noise is a combination of Johnson noise (I_J) and photodiode shot noise (I_p). Photodiode shot noise arises from random fluctuations in the arrival of electrons at the anode and is defined as:

$$I_p = R\sqrt{2eS_{PI}P_l\triangle f} \tag{4.1}$$

where R is the resistance of the photodiode I-V convertor, e is the electron charge, S_{PI} is the efficiency of the power-to-current conversion, P_l is the incident laser power and Δf the detection bandwidth. Johnson noise is electronic noise created

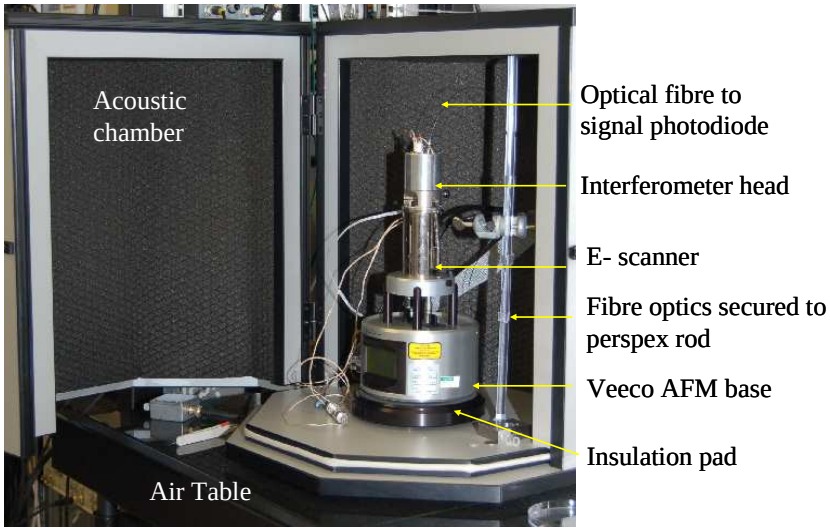

Figure 4.13.: Image of the interferometer set-up mounted on a Bruker AXS Multimode AFM base. The AFM is placed on an insulation pad and air table within an acoustic chamber.

by the thermal agitations that arise from the random motion of electrons in the resistor within the I-V convertor of the photodiode. It is defined as:

$$I_J = \sqrt{4kTR\triangle f} \tag{4.2}$$

where k is Boltzmann's constant and T is temperature. As shown by the equations, I_p is directly proportional to the resistance R of the photodiodes current-voltage converter, and I_J is proportional to $\sqrt{R}$. Therefore, by using a resistor of high R (in this case 22 kΩ), this results in an almost negligible contribution from Johnson noise and the ICD noise floor is mainly dependent on intrinsic photodiode shot noise.

4.4.2.1. Acoustic isolation chamber

It is crucial to prevent external vibrations from passing to the cantilever, as this would affect the image resolution immensely. To eliminate perturbations due to

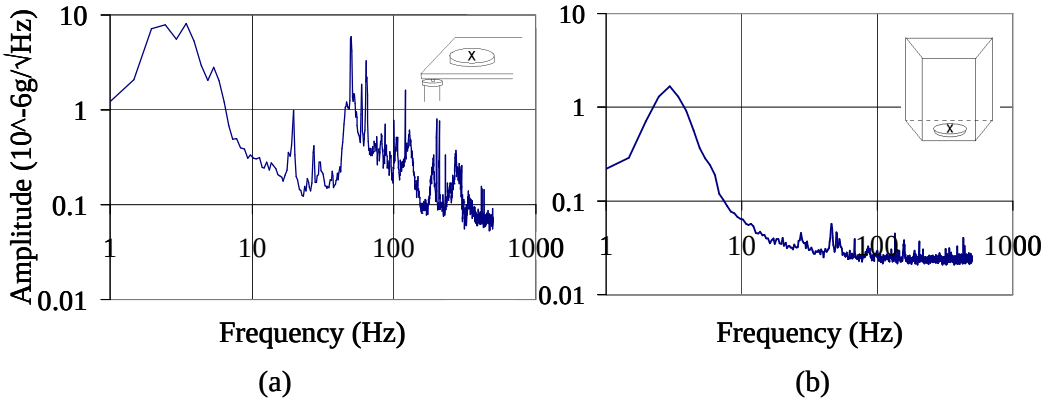

Figure 4.14.: Noise spectra (a) outside chamber on air table (b) inside acoustic chamber. Upon using an acoustic chamber, noise at frequencies larger then 10 Hz were effectively reduced.

mechanical, acoustic noise or fluctuations due to air drafts, the interferometer was enclosed in an acoustic chamber. Noise spectra was measured inside and outside the acoustic chamber via the use of an accelerometer and the results are shown in Figure 4.14. The acoustic insulation proved to be very effective, cutting off frequencies above 10 Hz. All fibres and photodiodes were also enclosed in an aluminum enclosure to shield from electronic interference or possible fluctuations due to air flow. Fibres exiting the acoustic chamber from the ICD head to the beam splitter were carefully clamped using rubber tubing to avoid external motion (shown in Figure 4.13). Finally, the entire set-up was based on a floating air table to dampen the vibrations from the building that the set-up resides in.

4.5. Interferometer measurements

4.5.1. Effect of adsorbate on f_0 on small and large cantilevers

Other then being used for imaging, the interferometer can also be used for *cantilever sensing* in liquid and in air. Micro and nano-mechanical resonators are

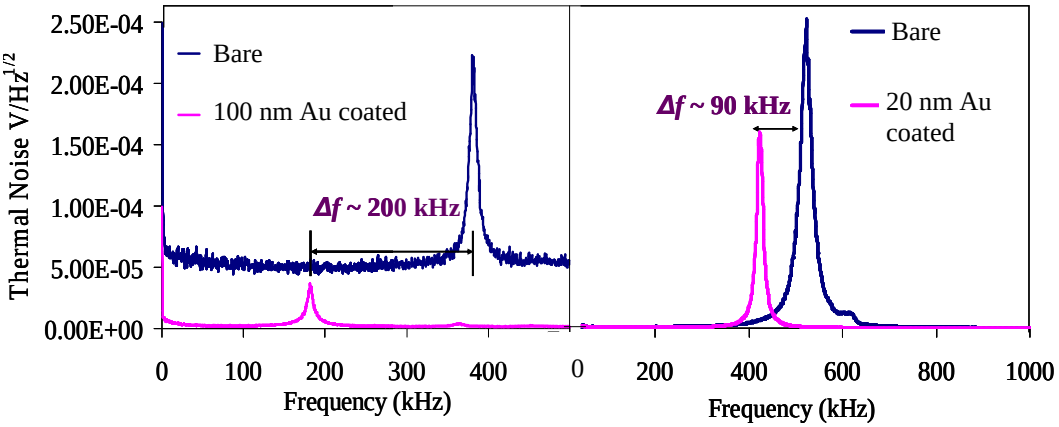

Figure 4.15.: Thermal noise spectra of small silicon cantilever (right) and large silicon cantilever (left) before and after a deposition of 20 nm and 100 nm gold coatings respectively.

powerful sensors of analytes in various environments. Their response, however, is a convolution of mass, rigidity and nano-scale heterogeneity of adsorbates. A paper by R. Gruter et al [82] was aimed to demonstrate a procedure to disentangle this complex sensor response, by simultaneously measuring both mass and elastic properties of nm thick samples. A part of this investigation was to study the change in the resonance frequency of a cantilever depending on the mass and Young's modulus of the adsorbate layer. The interferometer was used to take accurate readings of the cantilevers resonance frequency and quality factors before and after adding a layer of gold coating via E-beam evaporation. This data was then used to make calculations related to the rigidity and elasticity of nanosensors before and after the addition of an adsorbate and are further elaborated in Gruter et al [82]. Figure 4.15 shows an example of the resulting thermal noise spectra of cantilevers of varying size, before and after addition of adsorbate. It can be seen that the resonance frequency of the 'large' silicon cantilevers (dimensions 500 μm × 100 μm × 940 nm (l x w x t)) reduced by 50% after a 100 nm gold coating. The small silicon cantilever (dimensions 25 μm × 4.0 μm × 280 nm) had a 17% reduction in its resonance frequency after a 20 nm gold coating. Since the thermal noise spectra of large cantilevers could easily be measured on a conventional AFM, only the small cantilever thermal noise measurements were

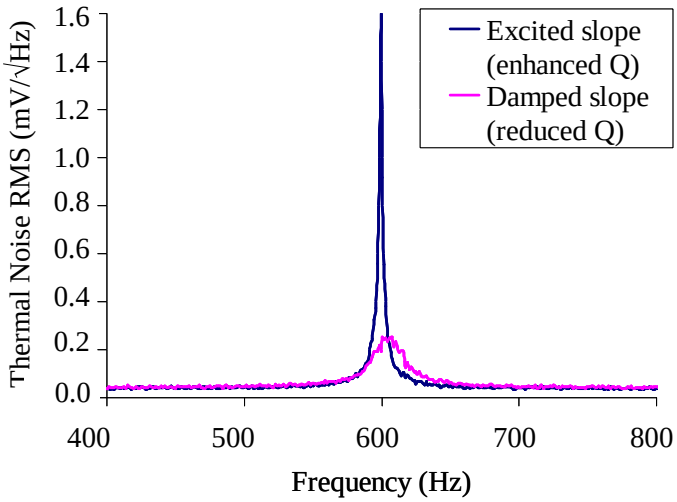

Figure 4.16.: Thermal noise spectrum of a small gold coated silicon cantilever (dimensions 25 x 4 x 0.2 μm, $f_0 = 605$ kHz) with set-points on either the excited (blue) or damped slope (purple).

carried out using the interferometer set-up.

4.5.2. Quality control and thermal heating effect

When measuring the thermal noise spectra of the gold coated cantilevers, the resulting Q's were affected by whether the set-point was selected on the positive or negative gradient of the interference pattern. This was caused by the cantilever becoming heated by the laser over time. Heat on the gold-coated side of the cantilever caused it to expand and bend downward. This resulted in enhanced oscillations. Since silicon possess a lower thermal expansion coefficient than gold, the bare-side expanded far less and counteracted this bending. Therefore, the oscillations on the silicon side were damped. Upon focusing the average light intensity on the slope that corresponded to the excited response from the cantilever, the resulting thermal noise peak possessed an enhanced quality factor (shown in Figure 4.16 by blue curve). Similarly, by choosing a set-point on the damped slope, this produced a thermal noise peak of low Q (shown in Figure 4.16 by purple curve).

To reduce this effect, the laser was defocused from the focal point, until similar Q factors were found on both slopes. Figure 4.17 depicts an example of how defocusing affected the Q of the thermal noise spectra of these small gold coated cantilevers.

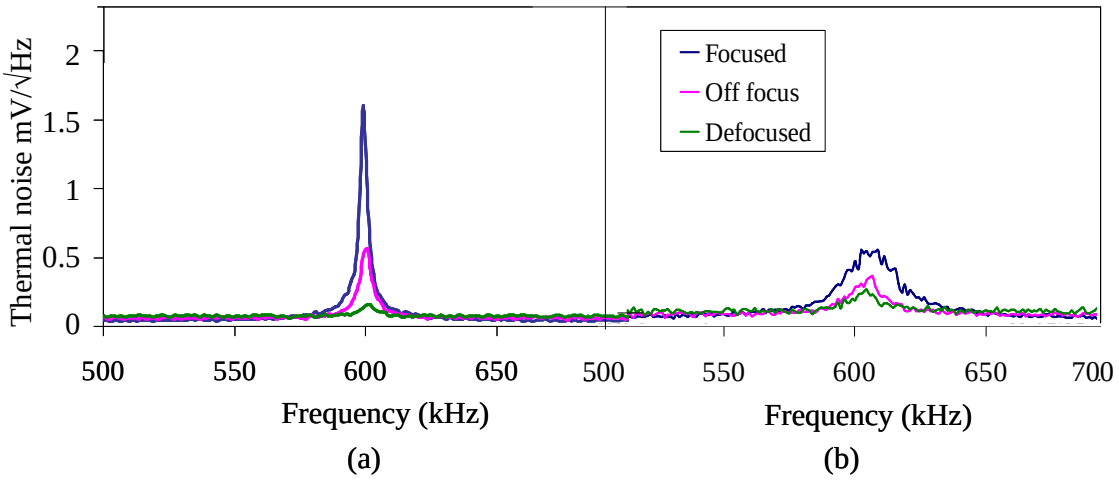

Figure 4.17.: Thermal noise spectra of a small gold coated silicon cantilever (f_0 = 600 kHz), showing the effect of defocusing laser optics on Q. Thermal noise spectra with set-point on the (a) excited and (b) damped slope.

4.6. Conclusion

In conclusion, varying temperature and current settings of the interferometric cantilever detector set-up were tested and optimised to ensure laser optics were stabilised. Noise contributions from laser diode and optical fibres were suppressed through the use of stable temperature control and rf modulation (10 MHz at 2 $V_{pk\text{-}pk}$). The set-up was effectively insulated from external noise sources > 10 Hz through the use of an acoustic chamber, insulation pad and air table. Preliminary tests using the interferometer to measure the thermal noise of small cantilevers also showed that the properties of the interferometer laser light intensity can affect the quality factor of the cantilever's thermal noise spectra.

Part II.

Results and Discussion

5. Imaging a flat surface at Atomic Resolution in Aqueous Solution

5.1. Introduction

To demonstrate the performance of our FM AFM in combination with the interferometric cantilever detector, the set-up was first used to image the surface of muscovite mica at atomic resolution in aqueous solution. Muscovite mica is an ideal surface since it is atomically flat and comprised of a well known regular atomic lattice structure. It consists of thin silicate layers that can be cleaved with ease, creating a flat and clean hydrophilic surface [83, 84, 85] without the need for complicated surface treatment. For this reason, mica is commonly used as a substrate for adsorbing biological samples and it is also used for high resolution AFM piezo calibration [86]. The following chapter describes how atomic resolution images were obtained using this FM AFM and the results are described.

5.2. Obtaining true atomic resolution on muscovite mica

The crystal structure [$KAl_2(Si_3Al)O_{10}(OH)_2$] of mica is comprised of several layers of aluminosilicate and each layer is separated by K^+ ions [84]. Mica is easily

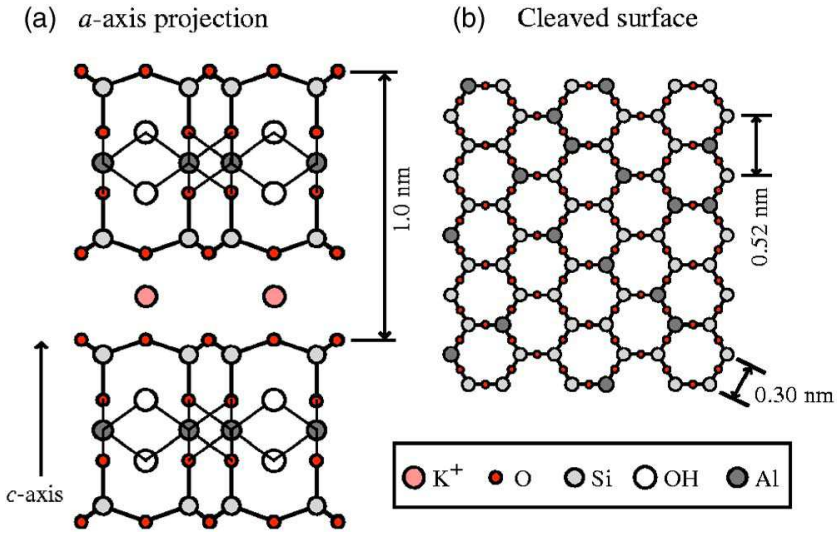

Figure 5.1.: The atomic structure of muscovite mica (side view) (b) Top view of the cleaved surface of mica, consisting of hexagonal unit cells. [15].

cleaved because of the weak bonds between the potassium ions and the adjacent aluminosilicate layers. The cleaved surface is hydrophilic and negatively charged in pure water. As shown by Figure 5.1, the surface of the crystal structure consists of hexagonal unit cells with an intermolecular distance of 0.52 nm. These units form a periodic hexagonal lattice made up of oxygen, silicon and aluminium atoms [15].

Contact mode AFM has been used to image of the crystal lattice of mica, (referred to as lattice resolution) in both air [87, 88, 89, 90, 91] and liquid [8, 15, 16, 65, 92, 93, 94]. The resulting image consists of periodic and symmetrical units that correspond to the lattice structure. However, this pattern can also be the product of induced frictional forces between the tip and surface. This was demonstrated by Erlandsson et al [87], who investigated the frictional forces between mica and a tungsten tip, by imaging the $Si0_4$ units that form the cleavage plane of mica. The image contained a faultless symmetric, uniform lateral periodicity that corresponded to mica's hexagonal units.

An indication of 'true' atomic resolution is the presence of atomic defects in the lattice. Ohnesorge et al [42] used contact mode AFM to obtain true atomic

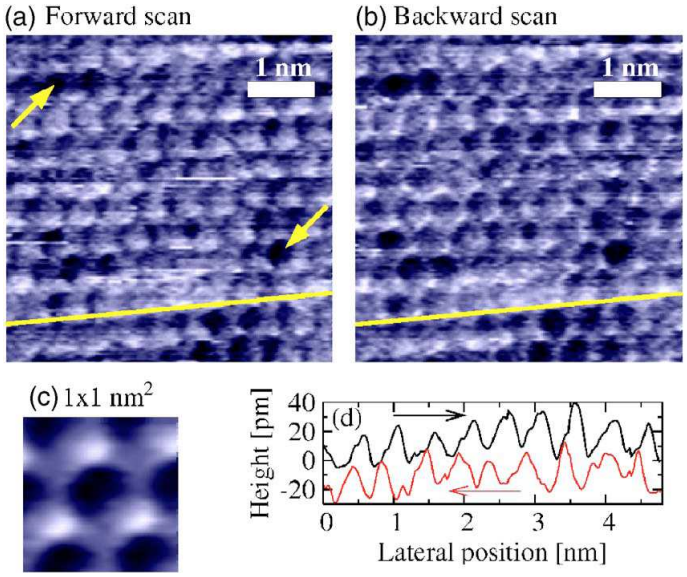

Figure 5.2.: FM AFM image of the cleaved surface of muscovite mica in liquid, as presented by B. Hoogenboom et al [16]. Imaged in buffer solution, with constant frequency shift $f = 110$ Hz and constant amplitude $A = 0.64$ nm. (a) Forward and (b) backward scan fast scan axis: horizontal. Vertical scale black to white is 70 pm. The arrows point at two examples of atomic-scale defects. (c) Correlation-averaged image of unit cell (vertical scale: 40 pm). (d) Line sections along the yellow lines in a and b. The arrows indicate the fast scan direction forward/backward for both curves.

resolution of the (1014) cleavage plane of calcite in water. The images contained well defined point-like defects, referred to as atomic-scale kinks, which strongly suggests that the image topography was indeed that of individual atoms and not merely the periodic pattern produced by tip-surface frictional forces.

Although contact mode AFM has been used to achieve atomic resolution, the technique is prone to producing high frictional forces during scanning [95]. FM AFM has proved to be a promising technique for obtaining atomic resolution. Using a low-noise optical beam cantilever deflection sensor, Fukuma et al [15] produced images with the presence of atomic-scale defects, suggesting true atomic resolution. Hoogenboom et al [16] also demonstrated the ability of FM AFM to image mica in liquid at true atomic resolution (see Figure 5.2). The images depict 0.5 nm intermolecular length hexagonal units that correspond to the lattice

structure of mica, as well as atomic-scale defects. More recently, Rasool et al [8], who employed a similar set-up to that described in this thesis, also obtained atomic resolution of mica. In all these examples, the purpose of the images was to demonstrate the high resolution ability of that particular AFM set-up.

5.3. Experimental method

The interferometric cantilever detector was mounted on an 'A scanner' (Bruker nano Santa Barbara, USA) with vertical z-range 704 nm and lateral scan size 1 µm. A conventionally sized silicon gold coated Nanosensors PPP-NCH cantilever, of dimensions (l x w x t) 225 µm x 43 µm x 4.0 µm and $k = 42$ N/m, was glued to the fluid cell using silver paint (Agar).

The interferometer optics were aligned to the cantilever and the resulting interference pattern was used to select a set-point to track the cantilevers position. The sample of mica was cleaved and 50 µl of imaging buffer (20 mM Tris-HCl, 150 mM KCl, pH 7) was applied onto its surface. Imaging buffer was also pipetted into the fluid cell to submerge the cantilever and sample in liquid. The thermal noise spectra of the cantilever was measured as $f_0 = 300$ kHz in air and $f_0 = 158$ kHz in liquid. 158 kHz was inputted as the centre frequency and self-excitation mode was established. The cantilever was then oscillated with a constant amplitude of 0.6 nm. Next, the cantilever was lowered towards the sample in ~10 µm steps using a step-motor control switch located on the AFM base. As it was lowered, the cantilever resonance frequency gradually decreased due to hydrodynamic interactions between the sample and cantilever [96]. This could be monitored on a LabVIEW interface which displays the frequency shift in Hz. When the frequency shift decreased sharply this indicated that the cantilever was in close proximity to the sample. Next, the Bruker AXS Multimode software (Nanoscope version VI) was used to make steps of 26 nm towards the surface. At the point of contact, a sharp upturn in frequency was expected, which occurs due to short-range repulsions between the tip and sample [65]. Therefore, to prevent a 'tip-crash', a trigger threshold was used to instruct the software to stop approaching when the frequency shift became greater then 200 Hz. All scanning was carried out using

minimal forces and the results are shown below.

5.4. Results

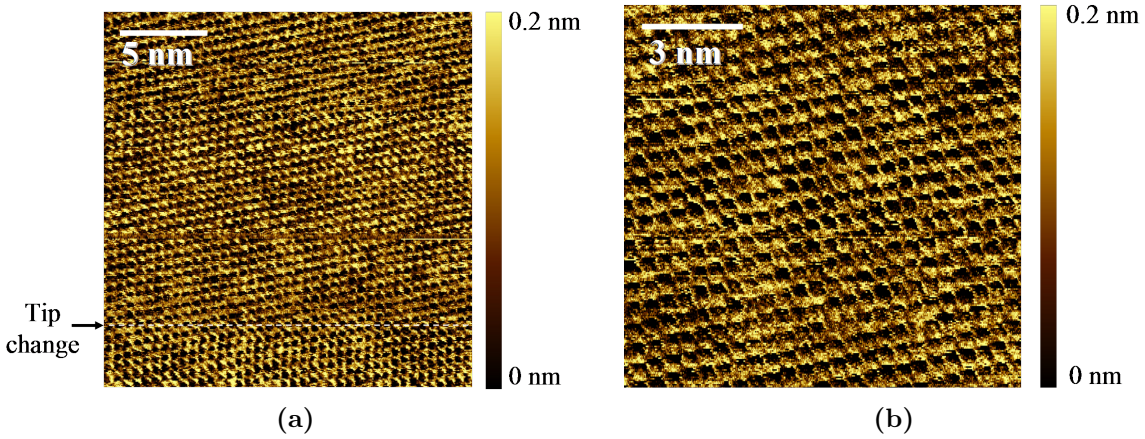

Figure 5.3.: FM AFM image of a cleaved surface of muscovite mica in an imaging buffer of 20 mM Tris-HCl 150 mM KCl pH 7, with constant amplitude of 0.6 nm. (a) 20 nm forward scan, with a tip velocity of 60 nm/s (b) 10 nm forward scan, with a tip velocity of 120 nm/s. Drift due to the non-linearity and hysteresis of the x-y piezo scanners caused some disruption and partial obscuring of the hexagonal lattices.

The atomic resolution images of muscovite mica obtained using FM AFM in a buffer solution (20 mM Tris-HCl 150 mM KCl pH 7) are shown in Figure 5.3 and Figure 5.4. The crystal lattice of its surface structure is clearly visible. Images shown in Figure 5.3 were taken at varying scan speeds to verify that the unit cells remained the same size and that the features were not merely tip artefacts. In Figure 5.3 (a) there is evidence of a tip-change after the scan line indicated, where the lattice periodicity appears to change contrast and shift position from the previous scan line. Due to drift caused by the x and y piezos, the hexagonal lattice also appears to be slightly skewed making the hexagons appear almost square. Other than slight distortions due to drift, upon changing scan speeds the size of unit cells remained the same.

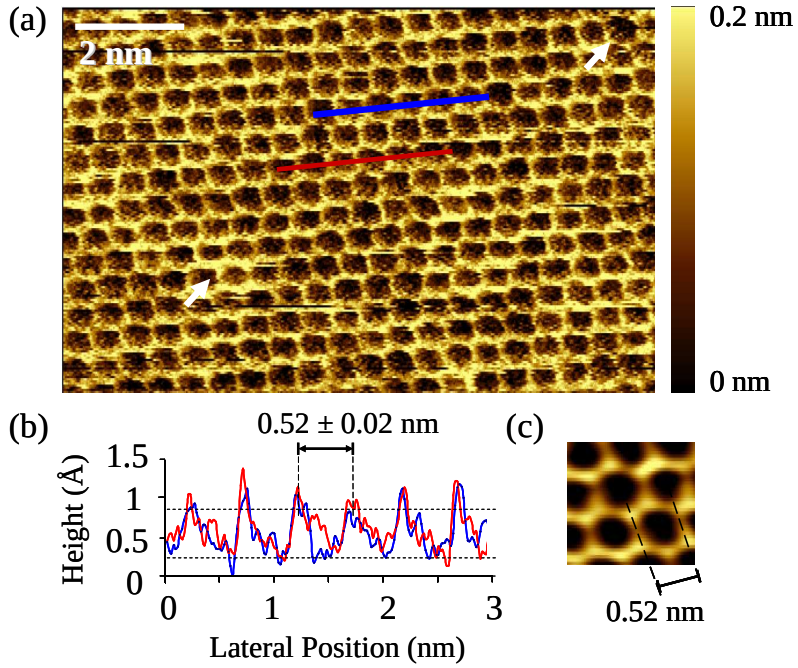

Figure 5.4.: (a) Atomic resolution of the surface of muscovite mica using FM AFM in an imaging buffer of 20 mM Tris-HCl 150 mM KCl pH 7. Imaged with a Nanosensors PPP-NCH cantilever with spring constant 42 N/m at a constant amplitude of 0.6 nm, tip velocity 61 nm/s and at a constant frequency shift of 100 Hz with respect to its resonance of 158 kHz away from the surface. The arrow indicates a possible atomic defect in lattice. X and y axes were adjusted (~ 5%) to correct for x-y piezo drift, otherwise the image is untreated. (b) A line-scan across unit cells as indicated in (a) showing a 0.52 ± 0.02 nm separation between unit cells. (c) A correlation average of unit cells showing 6 pointed hexagonal honey-comb structure.

Figure 5.4 is an atomic resolution image of mica over a scan area of 11 nm. A line-scan across the lattice (shown in Figure 5.4 (b)) indicates the average size of a unit cell to be 0.52 ± 0.02 nm, as was expected. Furthermore, the average height of corrugation was measured to be 1.0 ± 0.2 Å. A correlation average was also taken over the entire image and a section is shown in Figure 5.4 (c). In this image, the four unit cells and the six hexagonal points of the Si and Al atoms making up the hexagonal units cells, are well defined. Some height variations between different unit cells suggest the presence of atomic-scale defects (indicated by an arrow). In this image, the scaling of the x and y axes were adjusted (~ 5%) to

correct for drift caused by non-linearity of the x - y piezos, but no further image processing was applied [12].

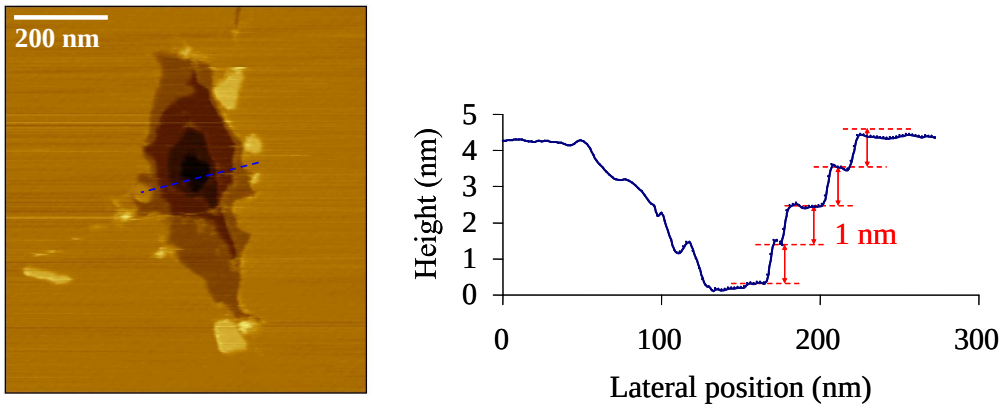

Figure 5.5.: (a) AFM image of a hole in muscovite mica in which multiple layers can be seen. (b) A line-scan across the hole depicting that the layers have a height of 1.0 ± 0.2 nm.

Figure 5.5 is an image of a large area scan at a hole in the mica's surface, that may have possibly been caused by the tip of the cantilever crashing into the surface. It may also be a defect or crack on the surface [95]. A line-scan across the hole (shown in Figure 5.5 b) clearly depicts the several layers of the crystal structure of mica. Each layer is 1.0 ± 0.2 nm in height, as expected from the known lattice structure (Figure 5.1).

5.5. Conclusion

These results demonstrate the ability of this FM AFM to image the flat surface of mica at atomic resolution. The resulting images clearly depict the honeycomb structure of mica's crystal lattice, with unit cell periodicity of 0.52 ± 0.02 nm. The six points of the hexagonal unit cells are also well defined. Furthermore, images were captured of the 1.0 ± 0.2 nm layers of the crystal structure.

6. Imaging a model Biological Specimen: Molecular Chaperone GroEL

6.1. Introduction

Found in the cytoplasm of the cell, GroEL is a molecular chaperone protein responsible for capturing newly synthesized polypeptides (chain of amino acids which define the protein) to assist them in folding into their native three-dimensional structures. Once captured in the chaperone protein's cavity, GroEL undergoes complex configurational changes during the protein folding process. The structural changes and how the chaperone is able to arrange the protein into the correct, complex arrangement is an ongoing subject of research [97]. To further understand this mechanism, we require an imaging technique which can allow the features on this 15 nm molecule to be visualised in detail, whilst it is still functional. Although there are several imaging techniques available which are able to define the structure of GroEL, such as EM and X-ray crystallography, they have the disadvantage of denaturing the protein during sample preparation procedures. The following chapter describes how FM AFM can be used to image this model biological sample in a physiological environment, where it can remain functional.

Since GroEL is commercially available (Sigma-Aldrich Corp), easily adsorbs on mica and its structure is well established, it is an appropriate sample for benchmarking in AFM technology. The aim was to image the characteristic seven-fold

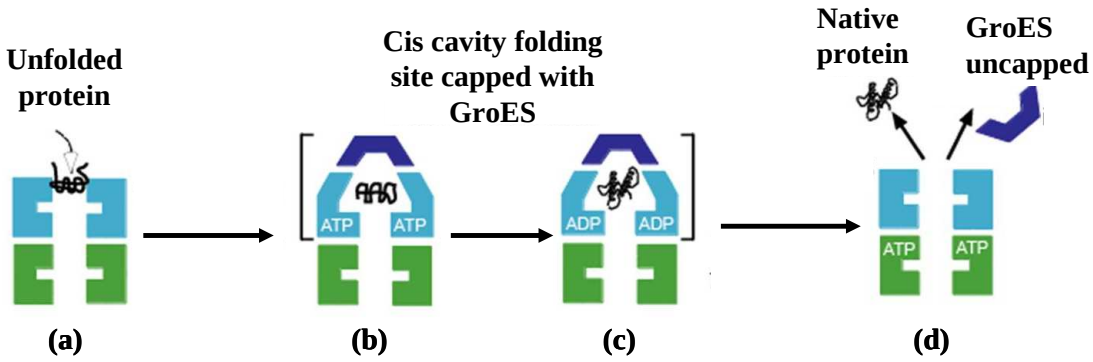

Figure 6.1.: Mechanism of GroEL & GroES chaperonin system for the folding of unfolded proteins. (a) Unfolded substrate bound to the cis cavity of GroEL's hydrophobic binding sites in the apical domain (blue). (b) GroEL is capped by GroES, trapping the unfolded protein. (c) Complex structural changes occur to fold substrate into its native state. (d) GroES lid is uncapped and the native protein released. (Image adapted from [17]).

symmetry of its uppermost ring structure, along with the cavity in its centre. The following chapter begins with an outline of the known function and structure of GroEL. Following this is a literature review which describes various AFM techniques that have been used to image the structure of these molecular machines. Next is a description of the experimental method used for preparing monolayers of GroEL on mica. Finally, the images obtained of GroEL using our FM AFM are presented and described.

6.2. Role and function of GroEL

For any biological molecule to function correctly, its structure must be in the correct three dimensional configuration. Whilst many proteins are able to fold spontaneously into their specific conformations, some require help to achieve this. Molecular chaperone protein GroEL ensures quality control in the cell by assisting the folding of unfolded polypeptides or misfolded proteins in the cell. As shown by Figure 6.1, the unfolded protein is recognised by its exposed hydrophobic surfaces, which are captured at hydrophobic binding sites inside GroEL's 4.5 nm cavity. Once captured, a second co-chaperone protein named GroES also

binds to the cavity which acts as a lid. The entire structure then undergoes complex configurational changes which folds the captured polypeptide chain into the correct configuration. Once folded, the GroES cap is triggered to detach and the protein is released [98, 99].

GroEL also targets misfolded proteins to either refold or denature them before they are able to transform into aggregated proteins. Aggregated proteins are associated with the development of critical diseases such as Alzheimer's, Huntington's and Parkinson's disease. The causes for defective protein folding and the study of chaperonins, such as GroEL, is a subject of research.

GroEL are also classified as heat-shock proteins (HSP60), which maintain cell function by protecting the tertiary structure of a protein in cases of cellular stress caused by temperature changes.

6.2.1. Structure of GroEL

GroEL is comprised of two rings referred to the 'cis' and 'trans' ring. Each ring is approximately 7.3 nm high and 13.7 nm wide resulting in a total height of 14.6 nm [100]. The cis and trans rings are each made up of seven identical subunits, making a 57 kDa subunit structure, which stack together to form a barrel-like complex. As shown by Figure 6.2 (a), the seven subunits are arranged with a distinct seven-fold symmetry that resembles the petals on a flower, forming a 4.5 nm diameter cavity in the barrel centre.

Each subunit is composed of three distinct domains; an apical, intermediate and equatorial domain. As shown Figure 6.2 (b), the apical domain is located at both ends of the two-ring barrel structure. It is composed of hydrophobic binding sites for unfolded polypeptides or the co-chaperone protein GroES. Only misfolded or unfolded polypeptide chains will bind to this site because, on their correct conformation, the hydrophobic domains are usually folded inside the structure and tucked away from the aqueous solution. The apical domains have some flexibility since they are attached to a pivot-like structure called the intermediate domain. The intermediate domain serves as a molecular hinge which connects the apical domain with the equatorial domain. Its main function is the transmission of signals which induce conformational changes between both domains. Both

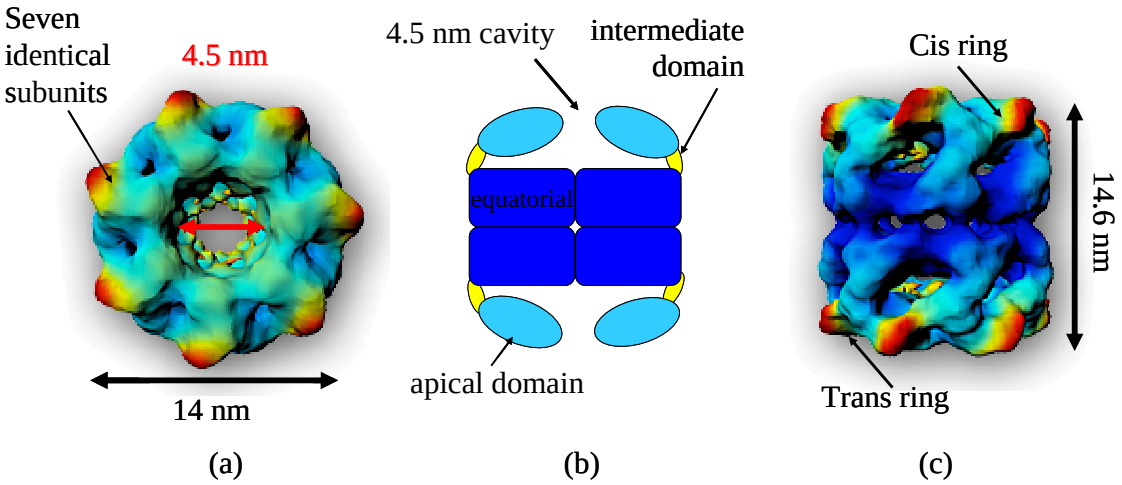

Figure 6.2.: Structure of GroEL based on EM data. (a) Top view of GroEL's cis ring, composed of 7 subunits forming its distinct sevenfold symmetry, with a 4.5 nm cavity in its centre. (b) Cross-section through GroEL barrel showing apical, equatorial and intermediate domains. (c) Side view of cis and trans rings forming GroEL's barrel like structure, with a total height of 14.6 nm. (Images (a) and (c) are adapted from Ludtke et al [18], who created these models using a particle analysis software package named EMAN).

heptameric rings are stacked back to back via the equatorial domains. This domain is comprised of α helices which form a well ordered structure, providing a solid foundation around the waist of the assembly.

6.3. Literature Review: Imaging GroEL

6.3.1. Deciphering the structure of GroEL

The first images of GroEL were obtained by Hendrix et al [101] using electron microscopy, where it was shown to be composed of a ring-like structure with a central cavity. Over a decade later, the first high resolution image of the structure of GroEL was captured using X-ray crystallography. Its distinctive barrel-like structure consisting of two rings stacked back to back, was first deduced at 2.8 Å resolution [100]. More recently, advances in cryo-EM [102] and NMR [103, 104] have allowed a more detailed observation of its structure. The extensions and

rotation of domains during the folding process have been imaged [97, 99, 105] and models have been constructed of substrates captured within GroEL's cavity [106, 107].

6.3.2. Imaging GroEL with atomic force microscopy

Although X-ray crystallography, cryo-EM and NMR have been able to deduce the structure of GroEL at atomic resolution, there is still the drawback that these techniques image the protein whilst it is no longer functional. AFM has the advantage of being able to image the protein in its native physiological environment, hence complex biological processes, like protein folding, may be imaged in real time.

High resolution of GroEL using AFM thus far, has been difficult to achieve. This is because the soft two-barrel complex can be very easily bisected or distorted by the high load force applied by the cantilever tip due to its weak inter-ring contacts. This has led researchers to use methods such as chemical fixation of the sample to help stabilise its structure for AFM imaging or else finding a technique which would ensure the force being applied is minimal. Next is a description of how GroEL has been imaged using AFM in liquids in past research using techniques or alterations to achieve the desired resolution, whilst attempting to retain its functionality.

6.3.2.1. Imaging GroEL in contact mode

Increasing structural stability for increased resolution

GroEL has been imaged in aqueous solution at sub-molecular resolution using contact mode AFM by Mou et al [19]. This was achieved by using chemical fixation of the sample. The authors describe that GroEL was adsorbed on mica with the addition of 2% glutaraldehyde to increase its rigidity. When imaged without chemical fixation, the sample was damaged, unstable and even dissected by the probe tip, as would be expected because of the non-negligible drag forces applied

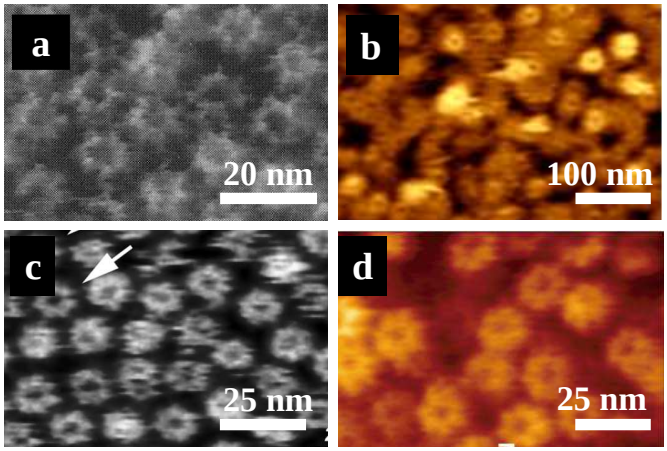

Figure 6.3.: AFM images of GroEL using varying techniques. (a) GroEL chemically fixed to mica and imaged using contact mode AFM by Mou et al [19] (b) GroEL monolayer imaged using contact mode AFM by Leung et al [20] (c) GroEL-SR1 single ring mutant imaged by Schiener et al [21] using tapping mode (d) FM AFM image of GroEL in liquid buffer as presented by Yamada et al [22].

in contact AFM. As shown by Figure 6.3 (a), the added sample stability allowed the sevenfold symmetry to be imaged in detail. However, the authors found that the cavities appeared larger than that reported by X-ray crystallography, EM and AFM imaging. This suggested that the addition of glutaraldehyde induced structural alterations to the protein, hence altered its function. This is an undesirable effect if the aim is to image the protein folding process.

In order to increase the stability of the GroEL ring without chemical fixation, the proteins can be adsorbed as a densely packed monolayer. As a monolayer, the lateral interactions of neighbouring proteins should supply sufficient stability during scanning. C. Leung et al [20] demonstrated this by imaging GroEL using contact mode in liquid. When a low concentration of GroEL was deposited on the surface of mica, the tip would strip the proteins off the surface despite the fact that minimal forces were applied. This also indicates the how weak the interactions between protein and mica substrate are. Upon increasing the concentration of proteins adsorbed, the authors showed that the resulting monolayer provided enough stability to be imaged repeatedly. As shown by Figure 6.3 (b), this yielded images of GroEL with dimensions close to that reported in X-ray

crystallography data. The authors also investigated the structural alterations that occur when GroEL is adsorbed on various substrates. The protein's structure was reported to have become distorted on both the gold and hydrophobic graphite and the protein's cavities were no longer visible. GroEL only retained its native conformation on hydrophilic mica where its cavities could be clearly resolved. For this reason, mica is the preferred surface for protein adsorption, since the immobilising forces are low enough to allow for uninfluenced conformational changes to take place.

Although contact mode has been used to produce images of GroEL whilst functional, the resolution obtained did not define the seven-fold symmetry of the cis ring. This is not surprising, since high-load forces involved in contact mode make it prone to causing damage to the protein structure.

6.3.2.2. Imaging GroEL in tapping mode

Tapping mode AFM reduces the contact time with the sample thus reduces the possibility of sample damage. This was demonstrated by Valle et al [108], where GroEL was imaged without chemical fixation. The importance of using the correct sample adsorption was also demonstrated. The author used buffers of increasing ionic concentration to obtain a stronger sample-substrate adsorption to ensure the chaperone was stable. By simply imaging more gently via the tapping technique, it was established that the sample could be imaged without the use of chemical fixation, thereby maintaining its structure and function.

Fast scanning

M.B. Viani et al [109] used tapping mode in combination with small cantilevers, for imaging the dynamics of individual proteins at a single molecular level. The author investigated how GroES binds and disassociates with GroEL by imaging with reduced dimension cantilever (10 μm x 5 μm x 75 nm) to allow for more sensitive force measurements. In addition, the use of small cantilevers allowed for

faster scanning speeds where the author aimed to make real time measurements on length scales associated with protein activity. The cantilever used had resonant frequencies between 130 - 200 kHz in liquid and oscillation amplitudes between 10 - 20 nm. Images were scanned at 10.2 Hz but due to the limited bandwidth of the feedback electronics, scanning speeds were limited to 20 µm/s .

Yokokawa et al [110] also used tapping mode to visualise and analyse individual GroEL–GroES complexes associating and dissociating in the presence of ATP. In addition, the ATP/ADP dependent conformational changes of GroEL without GroES at the single molecule level were imaged in real time. The literature demonstrated the ability of a prototype fast-scanning AFM [111] for imaging single molecules in real time and stated it as being >100 times faster than conventional AFM. Small cantilevers (10 µm x 2 µm x 0.1 µm) were used, which had spring constants of 0.1 – 0.2 N/m and 600 Hz resonant frequencies in water. Imaging was carried out at 1 – 4 frames per second and cantilever oscillation amplitudes of 1.2 – 2.0 nm. GroEL was adsorbed in a highly packed monolayer to ensure maximum lateral stability. It is also observed that when the density of the GroEL molecules on a mica surface was low, GroEL could randomly diffuse on mica's surface. Therefore, whilst imaging GroEL at conventional imaging speeds, it is crucial to ensure a high packing density to avoid this diffusional effect from causing further instabilities.

Preventing bisection and compression

Schiener et al [21] also published images of GroEL with its cavity clearly defined and seven-fold symmetry resolved (see Figure 6.3 (c)). This was achieved by imaging a single ring of the GroEL (named mutant SR1) which eliminated the effects of bisection. In addition, the surface topography was decreased to a height of 7 nm, reducing the effects of tip convolution. It was also shown that depending on whether the surface was hydrophobic or hydrophilic, the protein could be made to bind on either its equatorial or apical domains. To achieve high resolution images, a single ring chaperone mutant was used to cater for higher forces being used. This is viable for imaging GroEL's structure in detail though not a suited

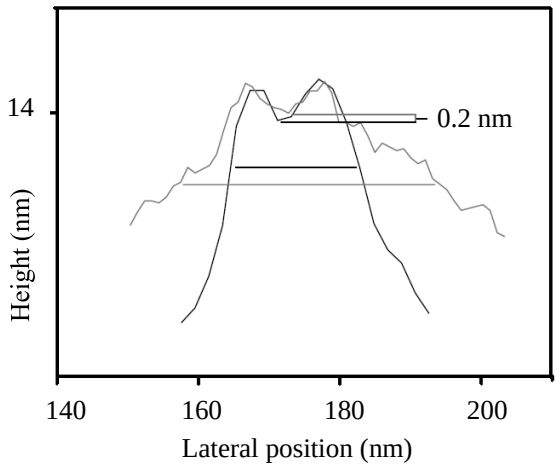

Figure 6.4.: The effect of tip radius on the depth of GroEL cavity, as shown by Valle et al [23]. Two profiles of GroEL are shown, which were imaged with cantilevers of varying tip radii. As the line-scan shows, upon using a broad tip, a larger lateral convolution correlates with a shallower penetration into the cavity.

technique for analysing its functionality.

Valle et al [23] also utilised tapping mode imaging on GroEL with the purpose of using GroEL's characteristic barrel like structure as a 'living' calibration sample. By measuring the depth of tip penetration in the cavity, the cantilever's tip shape could be determined, which is difficult to achieve with a commercial calibration sample. Since the GroEL cavity is 4.5 nm, the probe used to scan the surface of its structure must be sharp enough to probe within it. Tip convolution will most certainly occur if it is of the same order of magnitude as the feature being imaged. Figure 6.4 depicts how, by the use of two tip radii, one larger than the other (unspecified), the cavity appears shallower and deeper respectively. When using a larger tip radius, a bigger lateral convolution correlates with a shallower penetration into the cavity. The author also showed that during imaging, the cis rings becoming displaced by the tip, leaving single rings on the surface. Again, this demonstrates the importance of using minimal forces when scanning soft biomolecules.

Another example of the use of tapping mode (AM AFM) to image GroEL, was shown by Abdelhady et al [112] and co-authors. Imaging parameters such as

scan size, scan speed, set-point amplitude, proportional and integral feedback gains were individually varied and the authors describe the effect on the height and diameter of GroEL. Images were shown of GroEL localized on mica, where the height of the protein appeared as 2.40 ± 0.20 nm instead of 14.6 ± 0.05 Å, as measured by X-ray crystallography. The full height of the protein was not imaged because the tip was not tracing down to the substrate surface. However, the author mentions that the reduced height could also be partly due to compression. Compression is more likely to occur when imaging individual GroEL and where this effect can be reduced by using arrays of the protein.

Abdelhady et al [112] also showed the effect of increasing force on the measured diameters of GroEL and DNA using AM AFM. As the tapping 'strength' of the cantilever was reduced, the cavity diameter increased but the overall external diameter of the GroEL decreased. This was because, as the tip-sample interaction became reduced, effects of compression also reduced, thus making the diameter appear narrower. Also, by reducing the force exerted on the sample, the surface morphology was not tracked well, causing an apparent increase in diameter. Next, scan speeds were increased and the effect on the imaged height and width of GroEL and DNA observed. It was found that fast scanning increased the imaged height and width of the DNA, however the dimensions of GroEL were not significantly altered. This is not surprising, since AM AFM is prone to overshooting features due to limited feedback speeds. By increasing the scan rate, the feedback loop controlling the amplitude of the cantilever would be slow in responding to a sudden change in feature heights. Therefore, this delay in response would make the measured height or width of the DNA appear broader than it actually was. Since GroEL is relatively smoother than the strands of DNA, this effect was not as apparent. Finally, the effect of scan-size was shown not to cause any change to the image height of the GroEL, although it did increase the appearance of its diameter. This could be explained simply by reduction in resolution due to increase in pixel size as scan size increases. For example, the pixel size of a 0.5 μm 512 × 512 image was 1 nm but it increases to 6 nm at scan-size of 3 μm.

High resolution of imaging GroEL using frequency modulation AFM & low-noise cantilever detectors

Yamada et al [22] demonstrated the effect of reducing deflection sensor noise on the imaging resolution, using FM AFM operated in liquid and the applicability of this technique to biological molecules. Yamada et al [22] describes the development of a low-noise optical beam detector (OBD), possessing a low noise floor of 45 fm/√Hz. To achieve high resolution images of GroEL (shown in Figure 6.3 (d)), forces of less than 100 pN were applied and the cantilever was oscillated at amplitudes between 0.5 - 0.8 nm. On applying a higher load force, GroEL was bisected and the exposed equatorial domain of the GroEL was imaged to reveal the star-like seven-fold symmetry of the trans-ring. Once again, this demonstrates the importance of controlling the cantilever load force to avoid damaging or bisecting the sample. With the combination of high SNR in liquid and having the advantage of FM AFMs ability to measure and control the force exerted on the sample, the resulting GroEL images obtained were of higher resolution than that of previous studies.

6.4. Experimental method

To avoid lateral frictional forces dragging (or bisecting) GroEL off of the substrate, it was important to produce a protocol that would adsorb the proteins as a uniform monolayer on the surface of mica, with a high packing density. Therefore, during scanning, each neighbouring GroEL would laterally stabilise each other, reducing the chance of bisection. Furthermore, by adsorbing GroEL as a monolayer, the uniformity of the surface would resemble a flat surface with small features, which in principle should help to resolve detailed resolution. In order to adsorb a monolayer of GroEL, the correct concentration, adsorption buffer and substrate was required. Several published protocols for preparing monolayers were attempted and the resulting sample coverages were imaged. The experimental protocol adopted was that proposed by Viani et al [109], which produced the most reproducible monolayer of GroEL, although the protein concentration used for adsorption was altered.

6.4.1. Protocol for producing a monolayer of densely packed GroEL on mica

GroEL (purified from over-expression in *E. coli*) and was obtained from in the form of lyophilised powder (i.e. the sample was dehydrated through freeze-drying in UHV) from Sigma-Aldrich Corp. It was reconstituted in water making a concentration of 1 mg/ml. 10 µl of the stock solution was diluted with 490 µl of adsorption buffer 50 mM Tris, 150 mM KCl, 10 mM $MgCl_2$, 1 mM dithiothreitol (DTT), pH 7.5, to make a final concentration of 0.01 mg/ml [109]. GroEL remains biologically functional at pH 7 - 7.5 with K^+ and Mg^{2+} within its environment, therefore buffers containing KCl, $MgCl_2$ were used. Mica was chosen as the substrate for adsorbing GroEL, since it is a negatively charged and GroEL apical domain has as an affinity to bind to its hydrophilic surface. In addition, it is atomically flat, and as reported by C. Leung [20], GroEL retains its native conformation on its surface.

A small disk of mica was glued to a metal sample plate covered with a layer of Teflon. Since Teflon is hydrophobic, this would confine the liquid to the mica disk and prevent aqueous solution transferring onto the microscope scanner. The mica was then cleaved to leave a clean surface for the proteins to be adsorbed on to. 50 µl of the sample was deposited on freshly cleaved mica for 1 hour. A large amount was deposited on the mica plate simply to accommodate to the size of the sample disk. The sample was then gently rinsed three times, with 100 µl of buffer 50 mM HEPES, 50 mM KCL, 10 mM $MgCl_2$, pH 7.5, to remove loose or unbound proteins. The same buffer was used as the imaging buffer, as used by Viani et al [74].

Imaging and image processing

The cantilever was brought into contact with the sample using the same procedure described in the experimental methods in section 5.3. To obtain the optimum resolution, small amplitudes (specified in figure captions) and minimal forces were applied throughout imaging. The resulting images have not been filtered nor processed (unless otherwise stated) and have only undergone the 2nd order

plane subtraction flattening command using the Nanoscope software to nullify tilt in the image [113].

6.5. Results

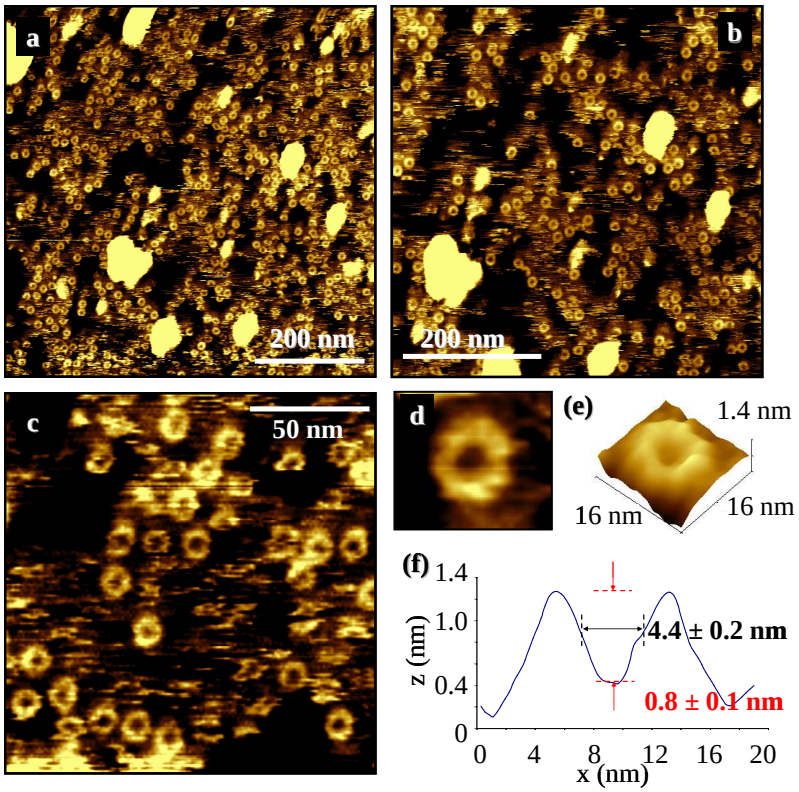

Figure 6.5.: FM AFM image of molecular chaperone protein GroEL in buffer: 50 mM HEPES pH 7.5, 50 mM KCl and 10 mM $MgCl_2$. (a) and (b) are large scan areas of GroEL dispersed over the surface of mica. (c) A 150 nm area scan of GroEL with features resembling the seven-fold symmetry of GroEL cis ring. (d) and (e) are digitally zoomed images of a single GroEL protein, in which the sevenfold symmetry of the apical domains can be seen around a 4.4 ± 0.2 nm cavity. (f) A line-scan across a single GroEL shown in (d). The cavity has a depth of 0.8 ± 0.1 nm and width 4.4 ± 0.2 nm. Imaged with PPP-NCH cantilevers with f_{liq}: 134kHz, amplitude: 3nm, z-limit : 1µm and scan rate: 1 Hz.

Figure 6.5 shows the resulting image of molecular chaperone protein GroEL using our FM AFM. The cavities within the protein's centre are clearly resolved and are visible even in large area scans. Figure 6.5 (d) is a zoom in of a single GroEL protein where features of GroEL's sevenfold symmetry can be seen. A line-scan across the protein cis-ring measures the cavity diameter as 4.4 ± 0.2 nm, which is close to that reported by X-ray crystallography measurements of 45 ± 0.5 Å. A line-scan across the protein's surface measures a diameter of 15.3 ± 0.2 nm. X-ray data has shown GroEL to have a diameter of 137 ± 0.5 Å [100]. In these AFM images the diameters appear broader which could be a consequence of tip compression. Moreover, since the protein surface is irregular and since the AFM image resolution is not very high, the exact dimensions are difficult to measure with these images alone.

The use of minimal forces allowed the surface topography of the upper most cis ring to be imaged. For this reason, the total 14.7 nm height of the protein could not be traced. The flat base within the cavity suggests that the cantilever tip was not extremely sharp or else it would have appeared more pointed due to the effect of tip convolution. The line-scan within the cavity could also be an indication of the cantilever tip's true dimensions, in which case, it appears to be quite broad and rounded.

The diameter of the proteins appear to be a nanometre wider then 14 nm reported by X-ray crystallography. This could be due to the tip not being very sharp, making the features appear broader. The image also contains large aggregates, that may be unbound proteins. Although they did not greatly affect the imaging of GroEL's features, large aggregates can be a hindrance and can be the reason for the tip becoming blunt or contaminated. To avoid this, more rigorous and thorough rinsing was implemented before imaging the sample.

Next, the concentration of GroEL was increased to 0.016 mg/ml in attempt to increase the packing density of the monolayer. Figure 6.6 is an image of the resulting monolayer. In comparison to Figure 6.5, the protein are adsorbed as a more dense and uniform monolayer. Although the cavities cannot be seen clearly, the seven-fold symmetry is still vaguely discernible. The line-scan measures shallow cavities with diameters between 2.3 to 4.3 ± 0.2 nm. This variation in diam-

eters suggests that the cantilever tip was not very sharp. Some aggregates are again present, although there are less aggregates than amount present in the first images, since sample rinsing was more thorough.

GroEL was next imaged using high scanning speeds of 10.5 Hz. The aim was to reduce the force applied on the surface per scan line over time. The resulting

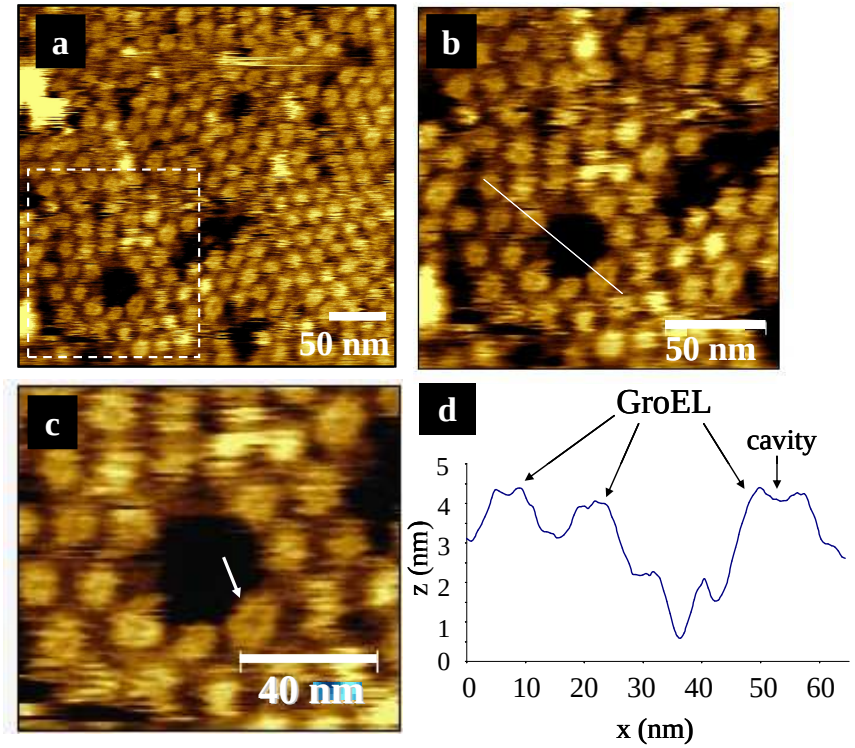

Figure 6.6.: FM AFM image of a densely packed monolayer of GroEL in imaging buffer: 50 mM HEPES pH 7.5, 50 mM KCl, 10 mM $MgCl_2$. Imaged with a cantilever with f_{liq} = 136 kHz and oscillation amplitude = 3 nm. Z-limit = 400 nm and scan rate = 1 Hz. (a) and (b) are images of large area scans depicting the dense packing of the GroEL monolayer. (c) Image of a 90 nm area shown in (a), where suggestible features of seven-fold symmetry are indicated by arrow. (d) A line-scan across three GroEL proteins shown in by line in (b). Shallow cavities with widths between 2.1 to 4.3 ± 0.2 nm are measured.

image is shown in Figure 6.7. Some features of GroEL's seven-fold symmetry are visible, although the cavities are again not clear. The high scan speeds caused prominent streak lines causing distortion to surface features. The cause for this

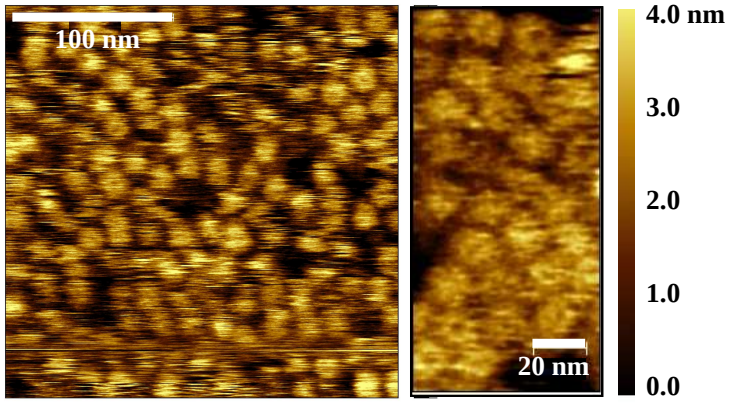

Figure 6.7.: Fast scan (line frequency 10.5 Hz,) image of GroEL in buffer: 50 mM HEPES pH 7.5, 50 mM KCl, 10 mM $MgCl_2$. Imaged using PPP-NCH cantilever with f_{liq} = 138 kHz, amplitude = 2 nm, z-limit = 400 nm scan rate = 10.5 Hz. (a) A large 220 nm area scan of densely packed GroEL monolayer on mica. (b) A 50 nm area scan of GroEL. This image has been flattened and scan lines erased to help discern finer features. Cavities and features of seven-fold symmetry are almost visible.

may have either been a blunt tip or else, despite trying to keep forces minimal, they may have been too high. The imaging buffer solution may have also been issue. If the Debye length had been reduced too thoroughly, attractive tip-sample forces may have been high.

A low salt buffer concentration of 20 mM Tris–HCl, pH 8.0, 2 mM KCl, and 2 mM $MgCl_2$ was also used to image GroEL (not shown). This is the same buffer used by J. Schiener et al [21] who produced high resolution images of GroEL's single ring mutant. However, using this buffer, the GroEL cavities became even further difficult to resolve. This could be because Debye lengths became longer, since electrostatic repulsions were not being sufficiently reduced. Therefore, the cantilever would 'hover' over the sample and not be affected by short-range interactions. Therefore, by using a low salt concentration buffer, although tip-sample dragging was reduced, finer features, such as the cavities, were not imaged at all.

6.6. Conclusion

FM AFM was used to image the features of molecular chaperone GroEL in liquid, without additional fixation to the substrate. By the application of minimal forces, the surface topography was imaged without much evidence of distortion to the proteins. Since the aim was to image the seven-fold symmetry of the protein's uppermost ring, minimal forces were used which prevented the tip from tracing down to the mica surface. As a result, the protein height was not measured at 14.6 nm. However, 4.4 $\pm$ 0.2 nm cavities were resolved and and features of the seven-fold symmetry could be seen.

7. Imaging Pore Forming Protein Pneumolysin

7.1. Introduction

Pneumolysin (PLY) is a pore forming protein (PFP) and part of the cholesterol-dependent cytolysin family (CDC) which attacks membranes containing cholesterol by the formation of pores [114]. PLY is released as a bacterial toxin by the bacterium streptococcus pneumoniae which is known to cause pneumonia. The initial stages of pore-formation are not completely understood, nor is the mechanism through which the membrane is punctured. To further understand these processes, pore forming proteins have been imaged using EM and X-ray crystallography. Although these techniques can resolve the structure of the protein in solution, the protein is not imaged whilst functional. Therefore, these techniques fail to follow the pore assembly process in real time. AFM is a technique which can be applied in liquids, therefore it has the potential to track the pore forming process of PFPs in physiological solution. Contact mode AFM has been used to image PFP perfringolysin-O [115] and PFP staphyloccal hemolysin [116]. However, in these experiments the PFPs were first incubated on the surface of a membrane prior to AFM imaging. Presented in this chapter are the first AFM images of PLY proteins oligomerising on the surface of a supported lipid bilayer (SLB). The PLY pores, which are of few tens of nanometres in size, were imaged as well as the sub-structure of the protein rings. The initial stages of pore-formation were tracked by comparing the height of the protein, immediately after adsorption, to the height of the protein after pore-formation.

This chapter begins with a description of the structure and function of PLY. Fol-

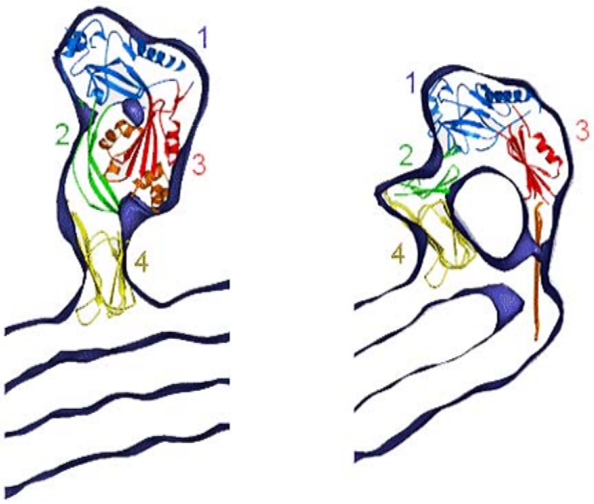

(a) **(b)**

Figure 7.1.: The structure of a single PLY monomer derived from the structure of PFO using cryo-EM. All four of the domains consist of beta sheets, with the exception of domain 3 which also contains alpha helices. (a) A single PLY monomer attached to a membrane. (b) The structure of a PLY protein during the formation of a pore into a membrane surface [24].

lowing this is an explanation of the protocol used to create cholesterol-containing supported lipid bilayers, onto which the protein would bind. Finally, the FM AFM images of the PLY are presented alongside a description of the image features.

7.2. Structure and function of PLY

The exact atomic structure of PLY has not yet been confirmed, however it is known to be very similar to that of PFP Perfringolysin-O (PFO). PFO is a bacterium responsible for gas gangrene [24], whose crystal structure has been characterised using X-ray crystallography [117] as well as electron microscopy [118]. PLY is a 52.7 kDa protein containing 471 amino acids and shares 60% amino acid sequence similarity with PFO and 48% sequence identity [119]. PLY's overall ring structure was first imaged using electron microscopy [120, 121], where its ring was found to be made up of individual monomers. These monomers were

described as asymmetric and slightly curved molecules consisting of four domains (shown in Figure 7.1). More recently, cryo-EM has been used to create models of these domains [24, 122, 121, 123] by fitting images of PFO's crystal structure into the electron density envelope of PLY. As shown by Figure 7.1, each of the domains is made up of beta sheets, packed into an elongated shape of dimensions 110 x 50 x 30 Å. Along with beta sheets, the 1st and 3rd domain also contains alpha helices which play an important part in pore-formation. PLY monomers have been found to oligomerise in the form of rings made up of approximately 50 subunits and are able to form pores of approximately 25 - 30 nm in diameter.

7.2.1. Pore-formation

Pneumolysin is initially released from the bacterium as water soluble monomers. The monomers seek cholesterol in the membrane of a cell, which acts as a receptor and allows them to associate with the membrane. They are known to oligomerise into arcs and rings on the surface. Hairpin-like structures (called β-barrels) insert themselves into the membrane surface, classing PLY as a β-pore forming protein, in contrast to α-pore forming proteins that insert α-helices. Studies on PLY pore-formation have shown that conformational changes occur in the monomers structure as they extend down into the membrane. Part of the protein extends into the membrane [124, 123], effectively punching a hole and mediating cell death.

It is suggested that the pore forming process varies between members of the CDC family [125]. There are two proposed models that describe the pore-formation and are illustrated in Figure 7.2. Model (A) suggests that the individual monomers initially bind to the membrane surface and oligomerise into a '*pre-pore*'. Once oligomerised as a ring, they then insert β-barrels into the membrane to perforate the membrane. The second model suggests the protein monomers immediately insert into the membrane and gradually assemble into a pore ring (Figure 7.2 (B)) [120, 126].

EM [118, 120] and cryo-EM [24, 122, 123] have been used to further understand the mechanism of pore-formation for PLY. These studies have shown that PFO

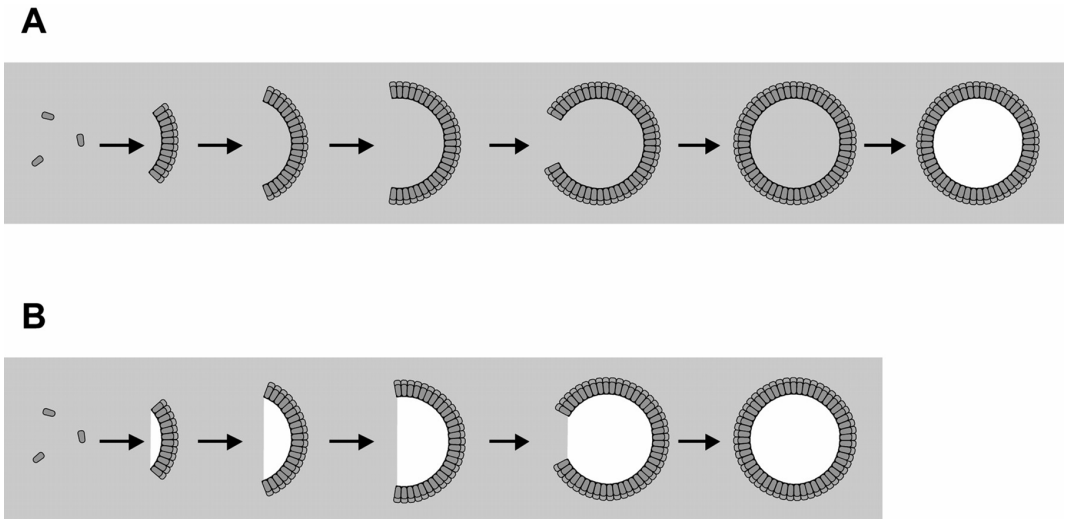

Figure 7.2.: Schematic of the two possible models of pore-formation of CDCs, as proposed by [25]. (A) Oligomerisation of individual monomers which initially form a ring (pre-pore) and then pore. (B) Pore forms gradually as the monomers oligomerise into ring formation.

and PLY follow model A, since they have been found to oligomerise on the surface as a pre-pores, then go on to form a pore (see Figure 7.3). Heuck et al [25] also showed that PFO and PFP streptolysin-O (SFO) follow the same mechanism of pore-formation.

Recently, cryo-EM has been used to carry out structural analysis of PLY in the pre-pore and pore states using electron density maps [24]. These studies have shown that in the pre-pore state, monomers sit far above the membrane surface and have structures much like the soluble monomers. During pore-formation, the beta sheets in domain 2 bend and separate into two parts allowing the structure to collapse downwards. This reduces the protein's overall height, bringing it 30 Å closer to the membrane surface (Figure 7.4). During this stage, the alpha helix in domain 3 unfolds into extended beta sheets. These beta sheets, which can be described as hairpin-like structures, then penetrate the membrane. As illustrated in Figure 7.3, each monomer in the ring extends its beta sheet to form an array of hairpins (called a beta-barrel) into the liposome. This forms a large (25 - 30 nm) diameter pore in the surface of the membrane. PFO and PLY are amongst the rare PFPs which switch to a secondary structure through the unraveling of alpha

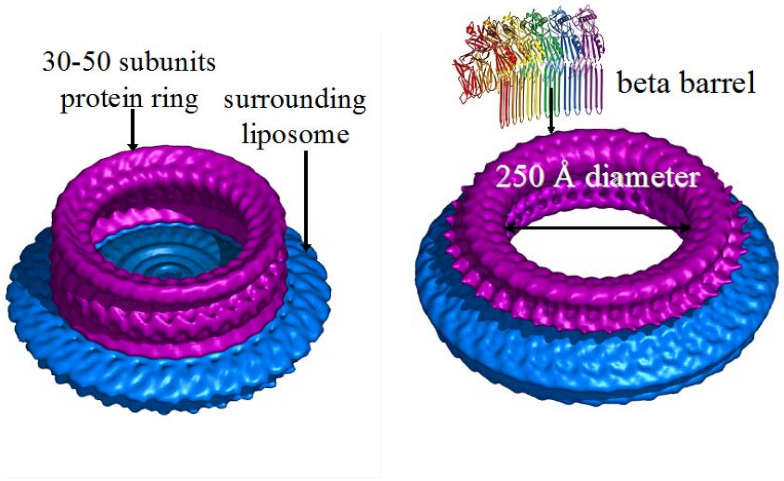

(a) Pre-pore **(b)** Pore

Figure 7.3.: (a) PLY in pre-pore stage (purple) on the surface of a liposome (blue). (b) PLY in pore stage, where height of the structure becomes reduced as the beta-barrel penetrates liposome surface. Image adapted from [24]

helices into beta sheets. pre-pore and pore stages of PFO have also been imaged using EM [127, 128] and the results are in agreement with the stages observed in cryo-EM.

7.2.2. Oligomerisation of monomers

It is known that PLY forms a pre-pore complex (Figure 7.4) prior to forming a pore into the membrane. However, it is unknown if the pre-pore forms arcs/rings through the oligomerisation of sequential monomers on the membrane surface, or whether the monomers form an arc/ring in solution and settle on the membrane. For example, Rossjohn et al [126] used electron microscopy data to construct a model of the steps in pore-formation of PFO. The authors suggest that the PFO monomers concentrate at the liposome and individually bind to the cholesterol receptor. These monomers then gradually oligomerise to form an arc or complete ring. The cholesterol activates the PFO monomers, causing a configurational change in their structure, where domain 2 collapses and allows the alpha helices

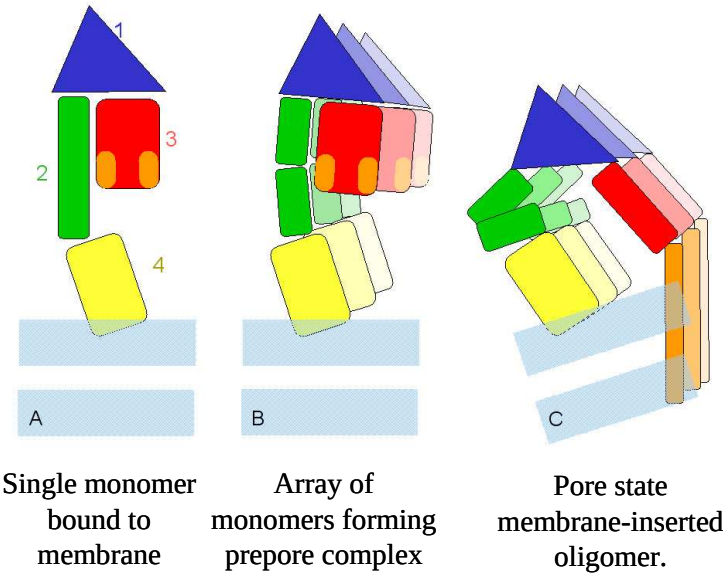

Figure 7.4.: A schematic model depicting the stages of pore-formation of Perfringolysin-O from monomer to pre-pore to pore [24].

to unravel near to the membrane surface. Finally, the beta sheets insert into the membrane creating the pore.

Pneumolysin is amongst the PFPs suspected of being able to prematurely oligomerise into rings in solution before interacting with the membrane [129]. However, this is a topic under investigation since the concentration of PLY in solution may play a role in whether or not this occurs.

To answer whether PLY undergoes the model proposed for PFO, it would be ideal to image the gradual evolution monomers forming arcs and rings over time. This would require the protein to be imaged whilst functional, making AFM in liquid a favourable technique. Furthermore, the images would need to be at nanometre resolution in order to image the single monomers assembling onto the liposome.

7.2.3. Height reduction during pre-pore to pore transition

It is debated whether these CDCs need to be in *complete* ring formation in order to form a pore, or whether they can form a pore and perforate the membrane even in arc-formation. PLY and PFO are amongst those PFPs which have been found

to form both rings and arcs. Pore formation of PFO has been investigated using contact mode AFM by Czajkowsky et al [115]. The authors used a commercial Nanoscope II AFM (Bruker AXS) in contact mode to image the vertical collapse of PFO from the pre-pore to pore stage. They began by preparing membranes and incubating perfringolysin-O mutant $PFO^{S190C\text{-}G57C}$ onto their surface. This was then placed on a substrate for AFM imaging. These PFO were prepared such that the beta-barrels did not extend into the pore state. Through the addition of dithiothreitol (DTT), the proteins were triggered to undergo the transition into the pore stage and images were taken in real time. The prepore height of PFO was reported to be 113 ±5 Å, which reduced to 73 ±5 Å in the pore stage. This resulted in a 40 Å (or 35%) reduction in height after transition. This value also corresponded to the length of the unravelled alpha sheets in domain 2, which extend into beta sheets during prepore-to-pore transition. The overall height reduction was seen to occur to even the incomplete rings and arcs. This suggested that pores were still able to form when the protein was in arc form. These contact mode AFM images were also able to capture details of the individual monomers making up the ring structure.

EM and cryo-EM studies have also shown that the height of the PLY pre-pore ring becomes reduced as it transfers into the pore state. Furthermore, these studies also observe PLY forming pores whilst in arc formation. However, although these findings have been reported by several authors, the stages of pore-formation of PFPs are still a topic of debate. For example, it was suggested by Gonzalez et al [130] that the mechanism of pore-formation whilst in arc form may just be a consequence of the sample preparation involved in EM imaging.

7.3. Experimental methods

7.3.1. Supported lipid bilayers for CDCs

Imaging the pore forming process of CDC PLY requires a cholesterol-containing membrane for it to adsorb on to. As illustrated by Figure 7.5, the cell membrane is composed of a lipid bilayer which consists of two chains of phospholipid molecules.

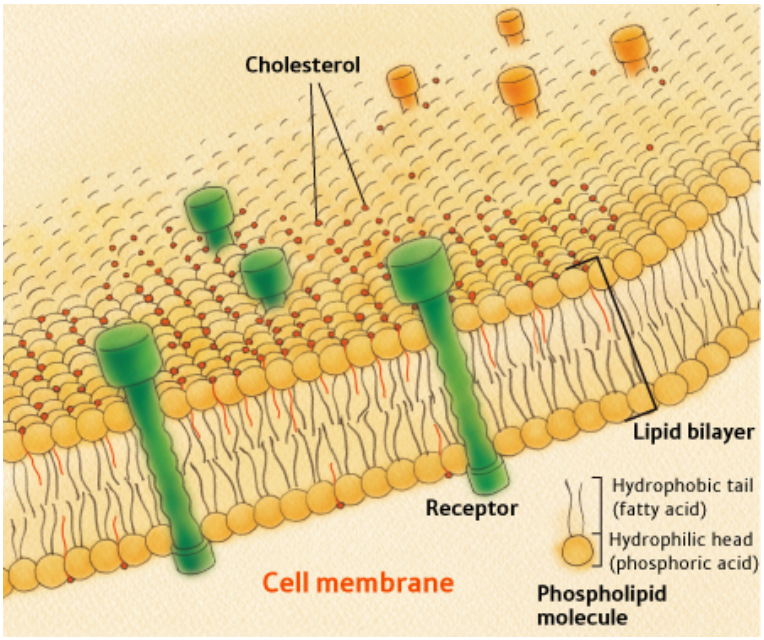

Figure 7.5.: Composition of a cell membrane [26].

The head of the molecule is made up of negatively charged hydrophillic (water soluble) phosphate and the tails are made up of lipids which are hydrophobic (water repelling) and uncharged. The two lipid chains are positioned such that the hydrophobic tails are tucked away from the aqueous environment and the hydrophilic heads face the outer and internal parts of the cell, both of which contain water. Cholesterol molecules are present throughout the membrane making up approximately 40% of its composition. Cholesterol fits in and around any gaps in the phospholipid. This adds fluidity to the membrane and reduces the membrane permeability [26, 131]. In the case of CDCs, the cholesterol in the membrane acts as a receptor. It is thought that the cholesterol may also play a part in the pre-pore to pore conversion, by assisting the bending of the protein [132, 133]. However, the interaction between the protein and membrane is still not completely understood.

Since the sample is not functional when imaged using electron microscopy, PFPs are deposited on liposomes solution prior to imaging. This involves drying the lipid mixture under a nitrogen stream, dissolving the dried lipids in buffer, then

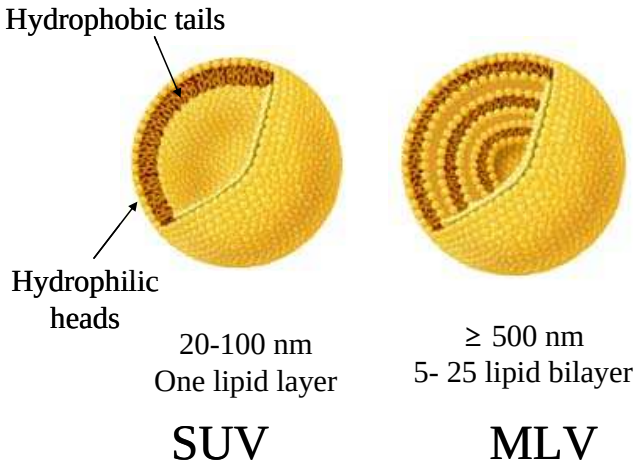

Figure 7.6.: Structures of small unilamella vesicles (SUV) and multilamellar vesicles (MLV) . SUV consist of a single lipid bilayer with diameters of 20 - 100 nm. MLV consists of several layers of lipid bilayers, with diameters from 500 nm up to 5000 nm. Image adapted from [27].

sonicating and filtering the solution. The protein is then added to the liposome and incubated. Similarly, in cryo-EM, after incubation the sample is then vitrified before imaging. Since atomic force microscopy allows imaging in real time, liposomes can be prepared (and imaged) prior to the addition of PFPs. Liposomes are prepared in the form of supported lipid bilayers (SLBs). Supported lipid bilayers are two opposing uniform layers of lipids adsorbed on a substrate such as mica [134], which resemble the structure of a cell membrane. They are widely used as model systems to study the properties or processes in the cell membrane.

One method of producing a SLB is by the fusion of lipid vesicles (FVM) [134, 135]. In this method, the lipids begin as single bilayer vesicles in solution, referred to as small unilamellar vesicles (SUV). These spheres are formed of two opposing layers of lipids and are shown in Figure 7.6. When SUVs come into contact with the negatively-charged mica surface, they rupture, causing the sphere to unravel into a flat layer (illustrated in Figure 7.7). Several SUVs rupture and fuse to form a continuous lipid bilayer.

However, lipids in suspension have a tendency to form of multilamellar vesicles

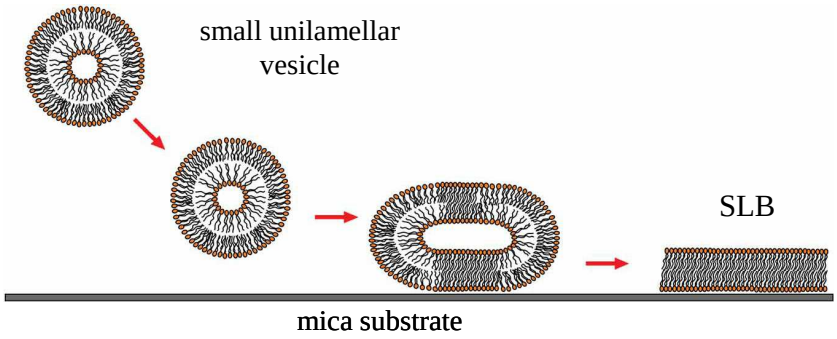

Figure 7.7.: Schematic of the fusion of lipid vesicles on a mica substrate. Small unilamellar vesicles come in contact with negatively charged mica and rupture to form supported lipid bilayers (SLBs). Image adapted from [134].

(MLV). As shown in Figure 7.6, multilamellar vesicles consist of several layers (or shells) of lipids that much resemble the shells of an onion. The hydrophobic tails are tucked away from the aqueous environment and the hydrophilic heads are exposed to water in between each lipid bilayer. In order to produce a single SLB on mica, the lipid shells making up the MLV need to separated into SUVs. Sonication can be used to achieve this. A sonication probe is placed within the suspension and through the addition of high sonic energy, the vesicles are reduced in size. During sonication, large titanium particles from the titanium sonication probe may also transfer into the solution. Therefore, once sonicated, the solution is filtered to remove these particles. Extrusion may also be used to form a solution of SUVs. Extrusion is a process where the lipid suspension is passed through a filter/membrane of a specific pore size, allowing only lipids with diameters equal to, or smaller than the pore size, to pass through [136]. Once in SUV form, a few microlitres of the suspension can be added to a cleaved surface of mica to fuse into SLBs.

7.3.2. Preparation of supported lipid bilayers (SLB)

7.3.2.1. Lipid preparation

Based on preliminary work, the lipid composition chosen was a 1:1:1 ratio of phosphatidylcholine (Egg PC), dimethyldioctadeclammonium (DDAB) and choles-

terol. PC (known to form a bilayer height of 5.0 ± 0.2 nm [137]) is a phospholipid naturally found in membranes and forms the basis of the SLB. Cholesterol was used to act as a receptor for CDC PLY. Furthermore, the presence of cholesterol added fluidity to the lipids and promoted mixing between them [131]. DDAB is a synthetic lipid (known to form a monolayer height of 2.8 nm [138]) which was added to the assist the SLB adsorption to the mica substrate. Since PC, cholesterol and mica are all negatively charged, this positively-charged lipid facilitated the adsorption of the SLB to the mica surface.

All PLY and lipids samples were prepared at Birkbeck University in the Biosciences division for all the experiments described. The lipids were purchased in powder form (which allowed them to be stored for longer) and mixed to an equimolar composition of cholesterol, PC (natural, egg) and DDAB with a final concentration of 2 mg/ml. Hydration was carried out using solutions at room temperature and vortexed for 30 mins. Sonication in a sonication bath was repeated 3 times at 30 - 40 ^{o}C for 10 - 20 mins. They were then frozen in liquid nitrogen which provided a reproducible recovery of different lipid mixtures and prepared them for extrusion. An Avanti extruder with 100 nm pore membrane was then used for extrusion. Since liposomes have a tendency to fuse to form multilamellar vesicles, the liposomes were frozen on the day of preparation and stored at -20 ^{o}C.

7.3.2.2. Adsorbing SLBs on mica

Preliminary work

Prior to the results presented in this chapter, preliminary work was carried out to observe the general behavior of pneumolysin on PC:Cholesterol:DDAB SLBs. 50 µl of 2 mg/ml concentration of PC:DDAB:cholesterol liposomes were defrosted then adsorbed directly onto cleaved mica for 15 minutes in a buffer of 50 mM NaCl, 10 mM $CaCl_2$, 20 mM HEPES pH 8. To remove any unbound lipids, the sample was rinsed 3 times with 100 µl of the same buffer. This method resulted in the adsorption of island-like patches of supported lipid bilayers scattered over the surface of mica (see Figure 7.8). Upon adding PLY, it was found that the

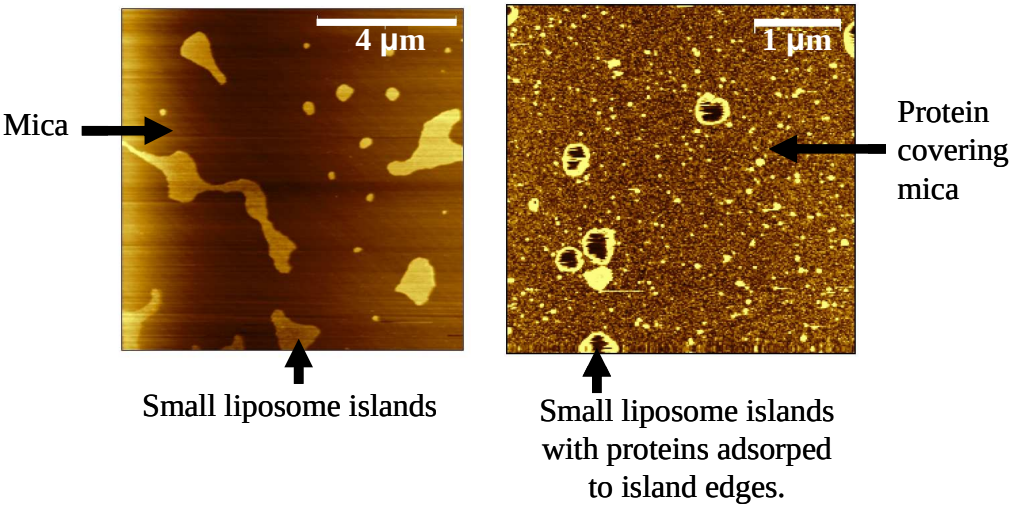

Figure 7.8.: Preliminary work on PLY. Left: FM AFM image of lipid bilayer islands consisting of PC : DDAB : Cholesterol, adsorbed on mica in a buffer of 50mM NaCl, 10mM $CaCl_2$, 20mM HEPES pH 8. Right: After insertion of PLY, protein can be seen to adsorb on the mica surface and on the edges of supported lipid bilayers.

protein had an affinity to adhere to the negatively charged mica. In addition, these results also showed that the proteins had a preference to adsorb on the edges of the lipid islands. This has also been observed in EM studies [118] when liposome patches were used. Since membranes do not naturally occur in island-form, this method would not have been a realistic reproduction of a membrane surface on which to image the pore-formation process. Also, using this protocol, excessive protein was wasted on the mica. Therefore, a more suitable protocol was required in which the SLBs could adsorb as one uniform layer across the surface of the mica. This would allow smaller amounts of protein to be used and eliminate the need to search for SLB islands during imaging.

FVM and preparation for AFM imaging

The lipid solution was sonicated using a Soniprep Sonicator 5 times, at 49 µm (peak-to-peak) probe oscillation amplitude, with 1 minute rest intervals. The

sample was immersed in an ice bath during sonication to avoid over-heating and subsequent lipid degradation. Sonication also ensured that the 3 lipids were mixed thoroughly and when adsorbed would remain well mixed. To avoid titanium contamination from the sonication probe, the sample was filtered using a 0.22 μm cellulose acetate spin filter in a centrifuge for 1 minute at room temperature. 50 μl of lipid sample was adsorbed onto freshly cleaved mica for 15 mins, then rinsed three times to remove unbound lipids with 100 μl imaging buffer (150 mM NaCl, 10 mM $CaCl_2$, 20 mM, HEPES pH 8) [1]. The presence of calcium ions in the buffer favored vesicle adsorption and SLB formation [134]. Pneumolysin was added to the 50 μl buffer volume on the SLB in a 0.5 μl volume containing 0.49 mg/ml PLY.

7.3.2.3. Imaging and image processing

Prior to adding PLY, the adsorbed SLB was imaged to confirm that a uniform layer had been adsorbed. To track the pore forming process of PLY, images of the protein were captured immediately after they were deposited onto the SLB. After a short period, the proteins were imaged again with the expectation of observing a reduction in height, whilst pores were formed. Furthermore, it was aimed to image lipids being displaced within the PLY pore as well as to capture details of the individual subunits making up the protein ring.

All AFM images presented in the results in this chapter have undergone the 2nd order plane subtraction flattening command using the Nanoscope software to nullify any tilt in the image [113]. Other than this, the displayed images were unfiltered and unprocessed. PPP-NCH-Au cantilevers of f_{liquid} from 128 - 135 kHz were used and oscillation amplitudes are specified within image captions. Imaging was carried out in a buffer solution containing 50 mM NaCl, 10 mM $CaCl_2$, 20 mM HEPES pH 8. Frequency shifts were typically between 50 - 100 Hz which corresponds to forces of <100 pN.

[1] Several variations in the protocol were made and tested which resulted in various coverages of SLBs on mica. The above protocol was based on that presented in [134] and was found to provide the most suitable uniform coverage of SLB on mica.

7.4. Results and discussions

7.4.1. Adsorption of uniform SLBs on mica

Figure 7.9 shows the image of the cholesterol-containing SLB prepared using the fused vesicle method. Most of the mica substrate appears covered in a uniform layer of lipids, though some patches of exposed mica are still visible.

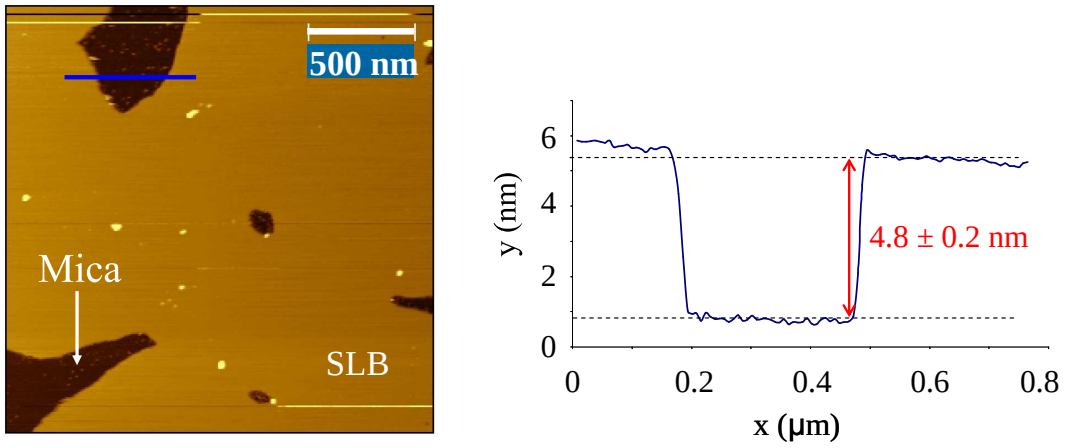

(a) (b)

Figure 7.9.: (a) FM AFM image of a supported lipid bilayer consisting of PC:DDAB:Cholesterol, adsorbed on freshly cleaved mica in buffer of 50 mM NaCl, 10 mM $CaCl_2$, 20 mM HEPES pH 8. Imaged using PPP-NCH-Au cantilevers, f_{liquid}: 135 kHz, at oscillation amplitude: 2 nm. Some areas of mica are exposed but the majority of the sample is covered in a uniform layer. (b) A line-scan across the blue line indicated in (a) shows a height difference of 4.8 ± 0.2 nm between mica and the SLB.

A line-scan, shown in Figure 7.9, measures a 4.8 ± 0.2 nm height difference between the SLB and mica surface. Since a single bilayer of lipids has a known height of 5 nm [138, 137], this strongly suggests that the surface is a single bilayer and these gaps are most likely exposed mica. There are also some particles on the SLB surface which may be unfiltered large vesicles.

7.4.2. Tracking the pore forming process of PLY

Presented here are the first images of PFP pneumolysin using AFM in liquid.

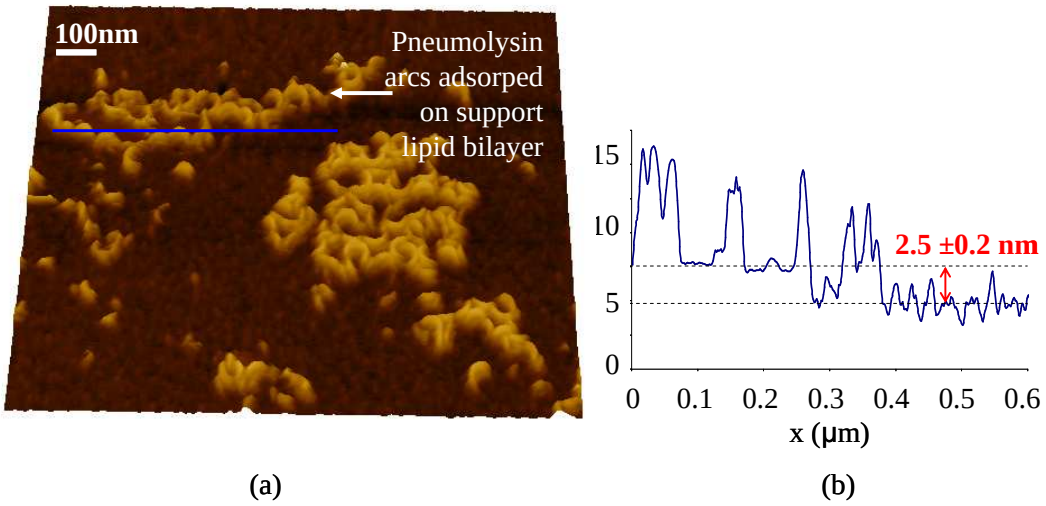

Figure 7.10.: (a) FM AFM image of PLY in arc-formation approximately 10 mins after insertion on supported lipid bilayers made up of equal amounts of PC:DDAB:Cholesterol. Arcs can be seen to adsorb only on the cholesterol-containing SLB. (b) A line scan across line indicated in (a). SLB height against background height measures at 2.5 ± 0.2 nm. The background appears to be mica covered in protein that do not assemble into arcs or rings. Imaged using PPP-NCH-Au cantilever, f_{liquid} = 128 kHz , amplitude = 2 nm, scan rate = 1.49 Hz in buffer 50 mM NaCl, 10 mM $CaCl_2$, 20 mM HEPES pH 8.

Figure 7.10 shows the image of pneumolysin approximately 10 minutes after protein insertion. The protein have oligomerised in arc-formation, with diameters ranging from 29 to 33 ± 0.2 nm. A flat area covered in protein arcs can be observed in the top-left corner of the image, which much resembles a SLB. A line-scan (Figure 7.10) across this feature shows that this area consists of flat plateaus with protein upon it. Below these plateaus there are also features with irregular heights.

Based on the images taken of bare SLB, the plateaus are most likely to be cholesterol-containing SLB patches onto which the PLY has adsorbed. The layer below these patches appears to be 2.5 ± 0.2 nm lower than the plateaus. Since

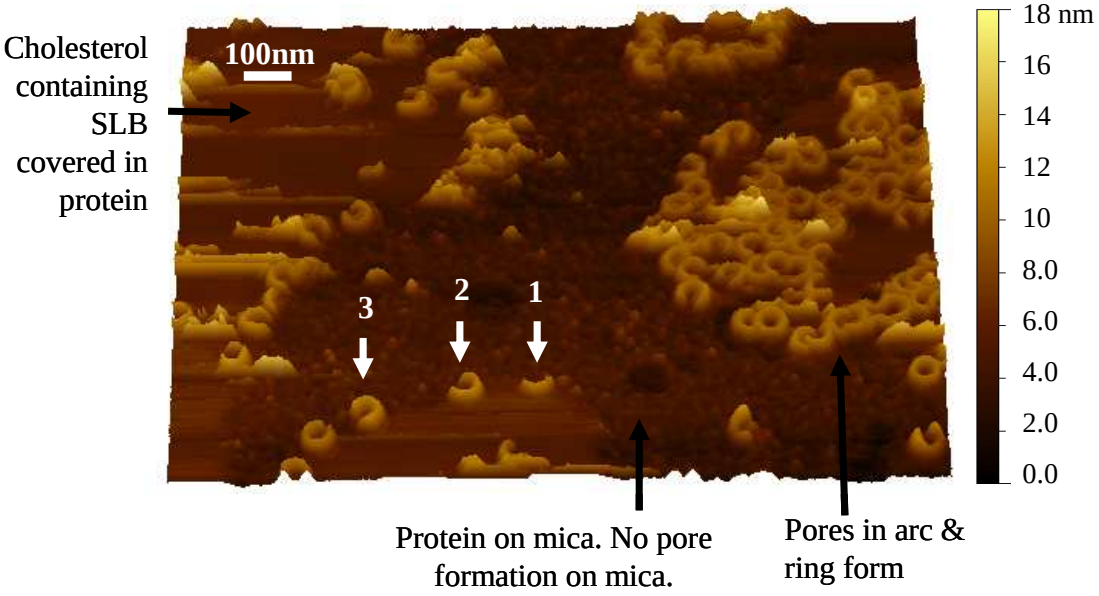

Figure 7.11.: FM AFM image of PLY in pore stage on a cholesterol-containing SLB taken ≈ 2 hours after initial protein insertion. Both arcs and rings are visible. Imaged using PPP-NCH-Au cantilever, f_{liquid} = 128 kHz , amplitude = 2 nm, scan rate = 1.49 Hz in buffer 50 mM NaCl, 10mM $CaCl_2$, 20 mM HEPES pH 8.

the SLB is expected to have a height of 5 nm, it is unlikely that this lower area is exposed mica. Furthermore, the surface is too irregular to be the flat surface of a SLB or mica. Since these proteins do not form arcs and remain static, this also suggests that the surface is indeed protein on mica.

If the initial image of the SLB is compared to this image, the SLB coverage appears much less uniform. It is possible that the lipids have been removed by PLY or else this particular 500 nm area of the sample, was not as well covered by SLBs.

The average height of the protein arcs was calculated from a statistical analysis of the image shown in Figure 7.10. To reduce error, an average cross-sectional height of each protein complex was calculated by measuring three lines-scans at varying planes across the centre of the pore[2]. Repeating this process, the protein is found to protrude 8.10 ± 0.22 nm above the surface (n = 24; the error corresponds to

[2]Line scans were performed using an AFM image analysis software named Gwyddion.

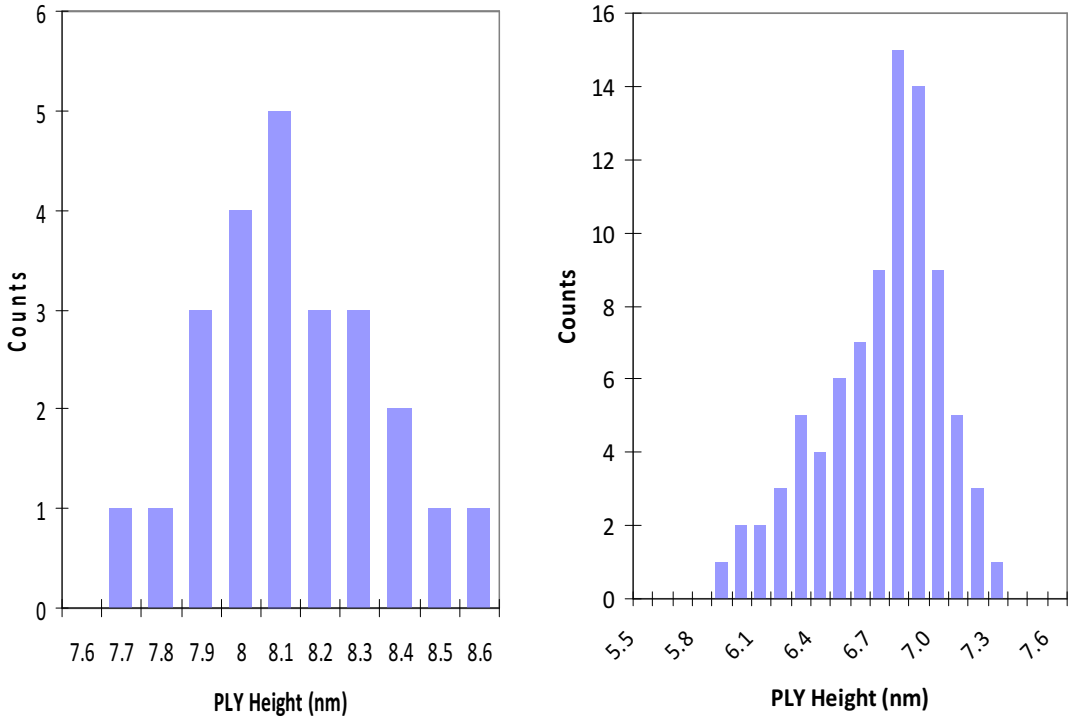

(a) (b)

Figure 7.12.: Histograms showing the height distribution of PLY proteins on SLBs in (a) suggested pre-pore state at t = 0 (as shown in Figure 7.10), (b) pore state after 2 hours of adsorption (as shown in Figure 7.11).

the standard deviation). Figure 7.12 (a) shows the distribution of the measured heights. EM and cryo-EM data have shown the height of PLY in pre-pore stage to be 11.30 ± 0.50 nm (and 7.30 ± 0.50 nm in pore stage) [24, 115, 118]. Since the protein arcs appear 3.20 ± 0.55 nm lower than this reported value, this suggests that the protein arcs may have already begun penetrating the SLB. Either this, or the reduced height could possibly be an artefact caused by tip compression.

Figure 7.11 is an image that was taken approximately 2 hours after Figure 7.10 and taken on different area of the same sample[3]. The image depicts PLY protein

[3]After the 1st image was captured, the cantilever tip became blunt from continuous imaging. This required the cantilever to be replaced and therefore a new area 500 nm of sample to

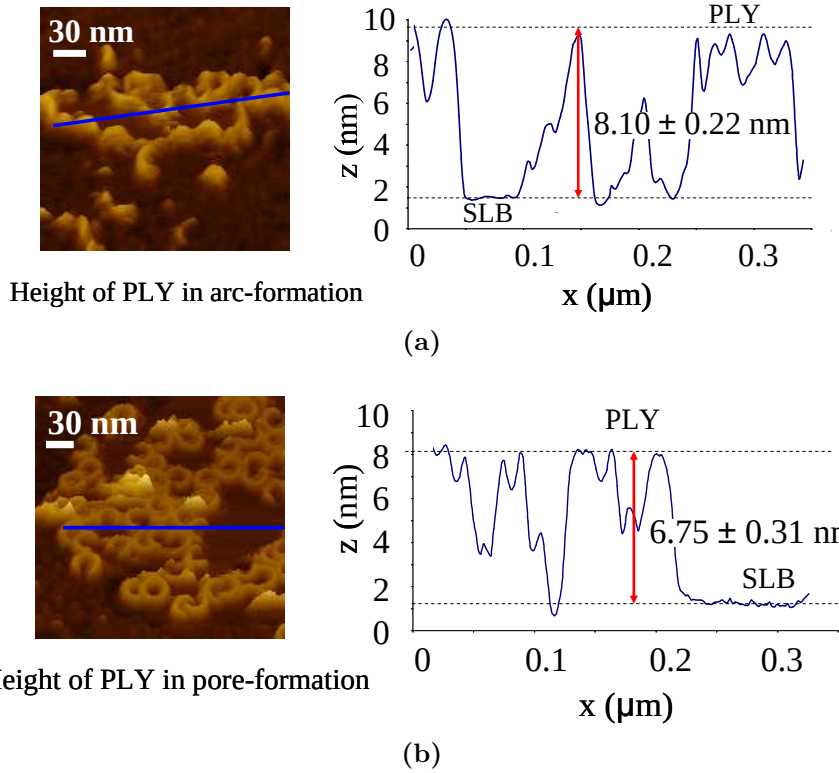

Figure 7.13.: Height profiles of PLY in arc and ring states showing a 1.35 ± 0.38 nm reduction in height after transition. (a) A line-scan measuring the average height of PLY as 8.10 ± 0.22 nm. (b) A line-scan measuring the average height of PLY rings as 6.75 ± 0.31 nm.

formed as rings and arcs over flat supported lipid bilayers. In addition, the centre of the image shows an area of irregular heights, similar to the first image. For reasons explained in the discussion of Figure 7.10, it is more than likely that the smooth plateaus in this image are SLBs and the area at a lower height is protein covered mica. The proteins only adsorb on the cholesterol-containing SLB and again do not form arcs/rings on the mica substrate. Moreover, in this image the protein arcs appear to have evolved into rings or near complete rings. The rings were measured to have diameters ranging between 29 to 34 ± 0.2 nm. The diameters of these rings are similar to the diameters measured of the arcs in Figure 7.10.

be imaged.

A statistical analysis of Figure 7.11 was used to calculate the average height of the proteins after 2 hours of adsorption, yielding 6.75 ± 0.31 nm (n = 86). Figure 7.12 (b) shows the corresponding distribution, which appears to be left skewed. This could be explained by the non-linearity of the force applied to the sample, where the protein may have become compressed if the tip-load force was high. Hence, a majority the protein heights appear lower than their expected 7.30 ± 0.50 nm pore height as reported by EM and cryo-EM data [24, 115, 118].

As described in subsection 7.2.3, once the beta-barrel has penetrated the SLB, a 4 nm (36 %) reduction in the pre-pore height is expected. The mean height of the arcs were 8.10 ± 0.22 nm which reduced to 6.75 ± 0.31 nm after pore-formation, resulting in a 17% height reduction of 1.35 ± 0.38 nm. Although smaller in value than the expected 4 nm reduction, these results show some degree of height change.

Furthermore, the arcs and rings in this image have the same height, suggesting that the protein can form pores whilst in arc form. At the very bottom of the image, three PLY arcs (labelled 1-3) can be seen, each with varying arc lengths. This suggests that the arcs grow whilst on the SLB surface in a chain-like manner, though this is difficult to confirm with these images alone.

7.4.3. Inside the pore

Figure 7.14 is an image of a new area of the same sample, approximately 2 hours and 30 minutes after the initial insertion the protein. PLY rings and arcs can be observed over the surface of the SLB. Arrows 1, 2 and 3 indicate areas within the centre of PLY pores where a puncture within the cholesterol-containing membrane can be seen.

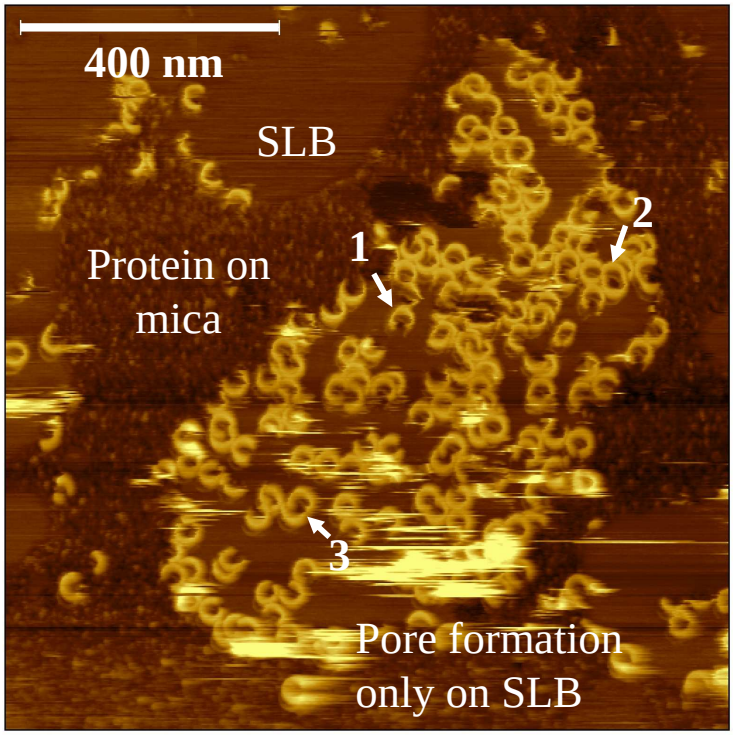

(a)

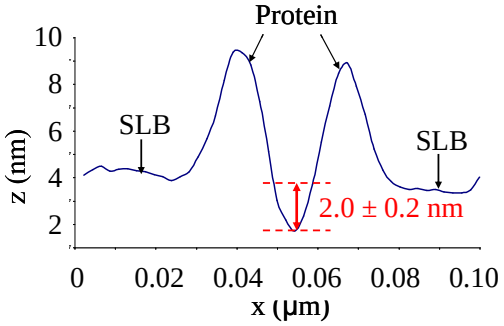

(b)

Figure 7.14.: (a) FM AFM image of PLY in pore-state on cholesterol containing supported lipid bilayers, approximately 2 hours and 30 minutes after initial protein insertion. The arrows point to protein rings/arcs which have formed pores within the SLB. (b) A line-scan across point 1 showing a 2.0 ± 0.2 nm puncture into the SLB surface. Imaged using PPP-NCH-Au cantilever, f_{liquid} = 128 kHz , amplitude = 2 nm, scan rate = 1.49 Hz in 50 mM NaCl, 10mM $CaCl_2$, 20 mM HEPES pH 8 buffer.

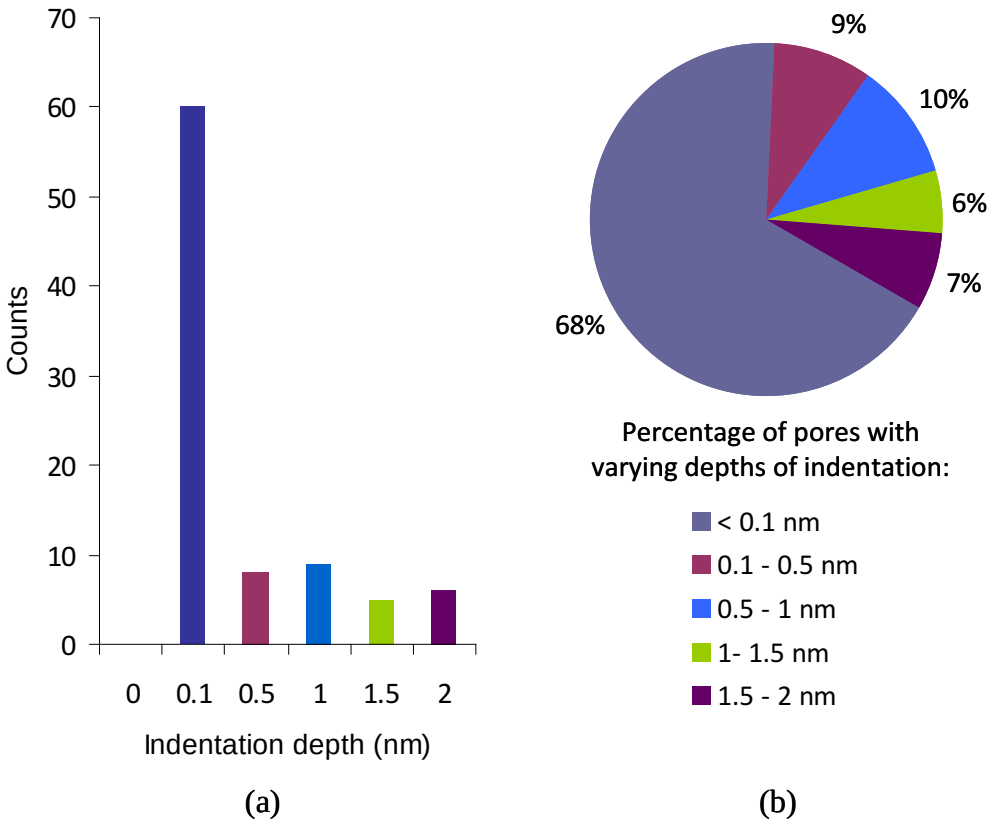

Figure 7.15.: (a) A histogram of the varying depths of indentation within the pores shown in Figure 7.14. (b) Percentage of proteins with varying depths of indentation. In these measurements 68% of protein do not have a well defined (< 0.1 nm) indentation depth within their pores. Only 13% of pores appear to have a indentations within the membrane with a depth > 1 nm (see text).

A statistical analysis of this image was used to measure the depths of the indentations, as well as to determine the number of proteins that had created an indentation within the SLB surface. Line scans were taken across each protein complex in the image. To reduce errors three cross sections were measured to calculate the average depth. An example of a line-scan is shown in Figure 7.14, where the centre of a pore appears to be 2.0 ± 0.2 nm lower than the SLB surface indicating that the PLY has punctured the lipid bilayer. (It should also be noted that the proteins have not oligomerised in a complete pore, implying that smaller oligomers can already perforate the membrane).

A histogram of the all measured indentation depths is shown in Figure 7.15. As shown by the figure, only 13% of the protein were measured to have an indentation of > 1 nm, 19% between 0.2 to 1 nm, where as 68% of the protein have indentations < 0.1 nm. The resulting histogram does not show a normal distribution nor a common depth size (therefore further statistical analysis was not possible). The actual depth of the indentations were difficult to measure using these set of results alone. This is due to several systematic errors which are outlined in detail below:

1) Tip geometry – size of tip in comparison to pore

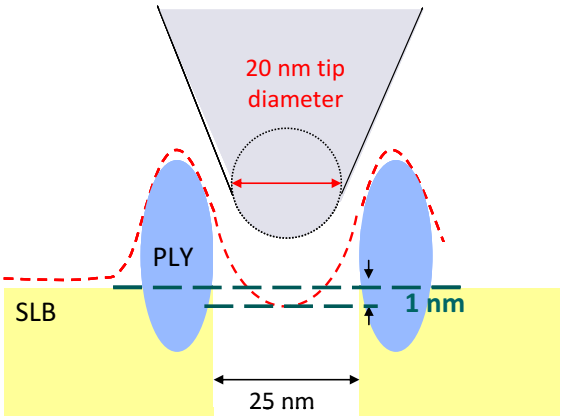

Figure 7.16.: A schematic of the cantilever tip with 20 nm diameter tracing the depth of a 25 nm width pore. As shown, the dimensions of the tip restricts the measurable depth of the indentation causing the topography to appear only 1 nm deep.

Imaging was carried out using PPP-NCH cantilevers, which have an average tip diameter of 20 nm. X-ray and cryo-EM data have shown PLY to have an internal pore diameter of 25 ± 0.5 nm [24, 126]. PLY height measurements, discussed in subsection 7.4.2, demonstrate that this tip size is sufficient for tracing the (6 - 8 nm) height of protein above the SLB surface. However, it is difficult to accurately trace a hole within the pore using a tip of similar dimensions. As illustrated by Figure 7.16, a 20 nm diameter tip can only penetrate as far as its dimensions

allow. This is also why the trough of the cross-section of the indentation always appeared pointed and not flat. Since the precise depth is limited by the tip shape, super sharp silicon (SSS) tips with radii of 2 – 5 nm would be more suitable tips to trace deeper within the pore.

2) 10° tip tilt with respect to arc orientation

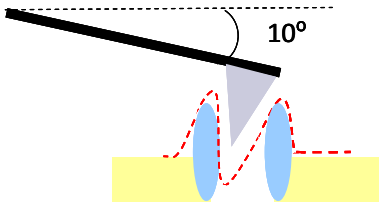

Figure 7.17.: An illustration of the 10° tilt of the cantilever and tip with respect to a pore in the SLB surface.

When the cantilever is mounted in the fluid cell, it has a 10° tilt with respect to the sample. As illustrated in Figure 7.17, this systematic asymmetry of the tip implies that even with a perfectly symmetrical tip, it can only trace so far within the pore and would not reach the full depth . Moreover, if tracing the depth of an indentation within the centre of an arc, the orientation of the arc will also affect how far within the centre the tip is able to reach (explained further in 3). A solution to this would be to use tilt-compensated tips.

3) Tip asymmetry – Double tip feature

In principle the tip of a cantilever is rotationally symmetrical across its axis. However, as explained in Chapter 2, tips are prone to picking up aggregates, becoming blunt or double ended during interaction with the sample. In the images shown in Figure 7.14 and Figure 7.18 every protein arc and ring appears to have a shadow caused by a double ended tip. This undesirable feature creates artificial artefacts over the image and constitutes a major error in determining the true depth within the pore. This has been emphasised in Figure 7.18. Arrow 1 points to a protein in full ring formation. Due to the double tip, a shadowing

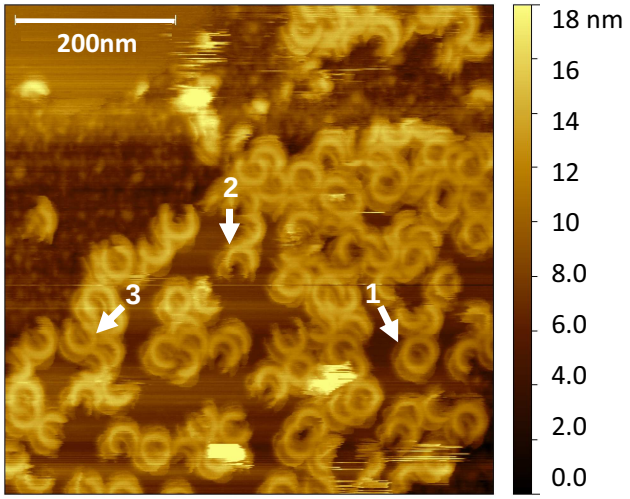

Figure 7.18.: 500 nm area scan FM AFM image of PLY rings and arcs adsorbed on SLB after 2 hours and 30 mins of initial protein addition. Image appears obscured by a double tip feature. Imaged using PPP-NCH-Au cantilever, f_{liquid} = 130 kHz , amplitude = 2 nm, scan rate = 1.49 Hz in buffer 50 mM NaCl, 10mM $CaCl_2$, 20 mM HEPES pH 8.

affect occurs within the centre of pore affecting its apparent depth. Arrow 2 points to a protein arc orientated downwards. Here the indentation within the pore is measurable, although a second arc is also apparent resembling a shadow. Arrow 3 points to an arc facing upwards. In this case, the double tip causes a shadowing affect on its outer edge and due to the tilt of the tip, the centre of the pore has not been traced. This is likely to be the main source of error which prevented the true indentation depth of the pores to be measured[4].

4) Position of protein on SLB

Figure 7.14 depicts an area of the sample where proteins are absorbed on a SLB which is not uniform but more like an island. As result, some proteins have settled on the edge of the bilayer. Upon performing a line scan analysis, these proteins appear to have deeper indentations within their centers than those on the flat surface of the SLB. This can be explained by the fact that the 20 nm

[4]Once this AFM tip became double ended the cantilever had to be exchanged.

diameter tip is able to trace down to the edge of the SLB in comparison to being confined by a closed ring or arc. This is another factor which creates a variation in the measurement of the true depth of indentation.

In summary, the image depicts some indication of the pores puncturing the surface of the lipid bilayer. However, in these images alone there are several systematic errors which prevented the accurate measure the depths of the indentations and further measurements would be required (see chapter 8).

7.4.4. Imaging monomers

Finally, the FM AFM set-up was used to image the 30 - 50 subunits or monomers of PLY and are presented in Figure 7.19. Although the measurement is obviously affected by convolution with a double tip, the corrugation on the rings suggests the presence of periodic subunits. Figure 7.19 (b) is a zoom-in over the same area where the colour of height profile has been adjusted in an attempt to further resolve the features on the protein.

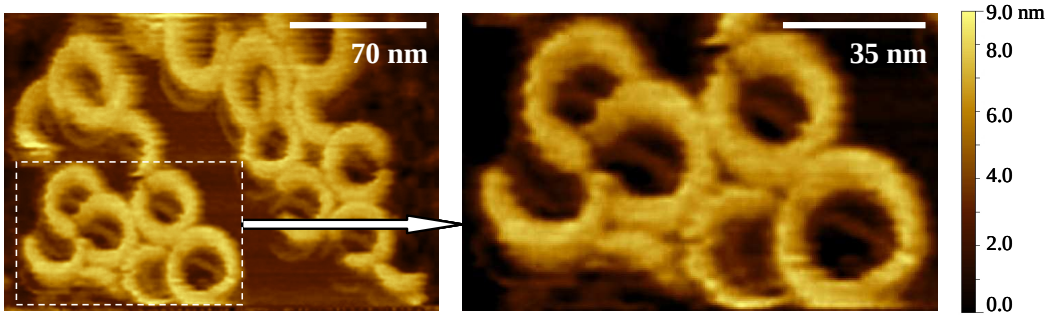

Figure 7.19.: FM AFM images of PLY in arc/ring formation containing a corrugation that resembles periodic monomers. Image (b) is a zoom-in of the lower left area of image (a) where the height scale has been adjusted to help define the protein's height of 6.75 ± 0.31 nm. Images were taken using PPP-NCH-Au cantilever, f_{liquid} = 131 kHz , amplitude = 2 nm, scan rate = 1.49 Hz in buffer 50 mM NaCl, 10 mM $CaCl_2$, 20 mM HEPES pH 8.

7.5. Conclusion

The FM AFM set-up was used to image PLY in liquid, producing images of the protein in arc formation and in ring/pore-state. Furthermore, images of PLY included periodic features that resembled its monomers.

After a statistical analysis, the proteins were measured to have an average height of 8.10 ± 0.22 nm upon first adsorption on the SLB. After 2 hours the average protein height reduced to 6.75 ± 0.31 nm.. This measured pore height is close to the pore height stated by cryo-EM data (7.3 ± 0.50 nm) [24], although tip compression may have caused it to appear lower. As a result, a 1.35 ± 0.38 nm height reduction was measured over time. EM and cryo-EM findings have shown a 4.0 ± 0.50 nm height reduction during the transition to pore stage [24, 118]. Hence, AFM clearly compresses the protein, but there is an observable difference in height that may correspond to prepore-to-pore transition.

Suspected pre-pores were found to only form arcs on the cholesterol containing SLB and did not self-assemble into rings on mica. The uniform height of the arcs and rings in the pore stage suggested that the SLB may be have been perforated whilst PLY was in arc-formation. In addition, since the sample preparation used for AFM should not affect the structure of the protein, and since the sample is immersed in a liquid imitating its physiological environment, these results suggests that arc-formation is a natural occurrence and not induced.

An image of individual PLY monomers was captured, similar to the image of PFO monomers acquired by Czajkowsky et al [115]. It is important to note that the results presented in this thesis depict PLY attaching to a cholesterol-containing SLB and then undergoing pore-formation in real time. In the AFM images presented in [115], the author began with a membrane with PFO already attached to its surface prior to imaging. Although this procedure yields a cleaner surface preparation and allows height changes to be imaged during pore-formation, it misses the assembly of the protein on the membrane.

If the images captured of PLY arcs in pore-state are compared to the length of the arcs when they had first adsorbed, the protein seems to have grown in size. This may be an indication that PLY arcs grow into rings through the sequential

addition of monomers, however, further tests are required to confirm this.

The images also contained some features that resemble the indentations within the SLB, demonstrating the FM AFM's resolution ability and its potential to be used to image within the pore. However, although perforation was visible, the true depths of the indentations could not be measured due to systematic errors. First and foremost, the images show that the tip was double ended creating features to appear doubled throughout the image. This masked the centre of the pores and created artificial artefacts. The indentation depth is also tip geometry dependent. Since a tip with a 20 nm radius was used, the depth was restricted by the dimensions of the tip. The varying arc orientations and 10^{o} tilt of the tip also affected how well the tip was able to trace within the pore. Hence, these images demonstrate how AFM can be used to measure the height of biomolecules (as long as tip-sample force is well controlled). However, it also demonstrates the limitations of AFM, where the measured depth of a hole in a surface is largely dependent on the tip geometry.

8. Conclusions and Further work

In conclusion, the FM AFM was optimised for stable imaging and used to image flat surfaces as well as biomolecules in a liquid environment at nano and sub-nanometre resolution.

Stabilisation and tests:

Noise in the interferometric cantilever detector, which originated from the laser diode and optical fibres, was suppressed through the use of rf modulation (10 MHz at 2 $V_{pk\text{-}pk}$). In addition, stable LD temperature and current settings were established to reduce the effects of mode hopping. Furthermore, an acoustic chamber was used to effectively isolate the set-up from acoustic noise > 10 Hz.

Tests on the frequency detector demonstrated its ability to detect frequencies 40 kHz to 15 MHz, where the upper-range is limited by the maximum output frequency of function generator. Moreover, tests on the frequency detector's response time to offsets proved it to be considerably faster (13 μs) than commercial AFM frequency detectors (e.g. 600 μs) [77] .

Imaging:

The first imaging experiment was implemented on the flat surface of muscovite mica in buffer. The image acquired clearly shows the hexagonal lattice with 0.52 ± 0.02 nm unit cell periodicity, which is in agreement with X-ray measurements.

Next, the molecular chaperone GroEL was imaged in buffer solution. Prior to imaging, a protocol for adsorbing a monolayer of protein was established. The resulting images depict 4.4 ± 0.2 nm cavities in the centre of GroEL's cis-ring.

In addition, the topography of the protein surface contained features which resembled the characteristic seven-fold symmetry of GroEL's apical domain.

Finally, the pore-formation process of pore forming protein pneumolysin was imaged in buffer solution. To achieve this, a protocol was established to produce a monolayer of cholesterol-containing supported lipid bilayers. Upon adding the protein to the SLBs, it was found that the protein only adsorbed on the cholesterol containing SLB and did not self-assemble into rings on mica[1]. Next, the heights of PLY arcs, before (8.10 $\pm$ 0.22 nm) and after (6.75 $\pm$ 0.31 nm) a time lapse of two hours, were compared. It was found that the overall protein height became reduced by 1.35 $\pm$ 0.38 nm. Although a height difference was observed, the magnitude of reduction was smaller than the 4 nm height reduction reported by cryo-EM, EM and contact AFM results [24, 115, 118]. It is possible that the protein beta-barrels penetrated the SLBs very quickly, therefore a small height change was captured at the final stage of penetration. It was also found that the reduction in height occurred even when the protein was in arc form. This suggests that PLY could perforate the SLB without being in full ring formation. The images also include some features which indicate indentations in the SLB within the centre of pores suggesting that lipids had been removed by the protein. Finally, a periodic symmetry resembling monomers was observed on the protein ring surface demonstrating resolution ability of the FM AFM.

Overall these results presented in this thesis demonstrate that FM AFM can be used to facilitate the structural analysis of proteins and the study of their complex biological mechanisms. Rather than a stand alone technique, AFM is complementary to X-ray crystallography, cryo-EM or NMR imaging, in which one can be used to image the structure in three-dimension and one to further understand the structural changes in real time.

[1]Further control tests carried out by Dr Carl Leung in our group, confirm that the proteins do not oligomerise into arc or ring form on the mica substrate.

Further work

Refining the image resolution of GroEL

A protocol to produce a monolayer of GroEL on mica was established, which allowed the 4.4 ± 0.2 nm cavities of GroEL to be imaged. However, the seven-fold symmetry lacked in definition. The resolution can be improved by reducing the aggregates on the adsorbed monolayer surface. This could be achieved by testing sample rinsing techniques to find one rigorous enough to clear the surface of aggregates but without striping the monolayer from the substrate. Less aggregates would reduce the chance of the tip becoming contaminated and thus increase spatial resolution. In addition, it would be beneficial to carry out further tests with varying electrolyte concentrations in the imaging buffer. This could test if insufficient electrostatic shielding was the cause for the lack of clarity.

Furthermore, as demonstrated by [23], it would be plausible to next observe the effects of super sharp silicon tips on the resolution of GroEL. However, sharper tips could also cause damage to the protein structure. Therefore, whilst imaging with SSS tips it would be essential to ensure the protein was adsorbed as a densely packed monolayer to increase rigidity and that the forces applied were minimal.

Imaging monomers and tracking PLY monomer assembly.

The FM AFM was used to image the absorption of PFP PLY on SLBs and the images contained details of the monomers making up the protein ring structure. This demonstrates that our FM AFM has the potential to be used to image the initial stages of monomer assembly. However, difficulties may be encountered. To observe the oligomerisation of monomers over time, this would require repeatedly imaging on the same area of sample for long periods of time. As found by the experiments carried out over the course of this research, this would inevitably cause the cantilever tip became blunt and resolution would become impaired. Due to limitations of the set-up it is impossible to exchange the cantilever and return to the same sample area to view how it has evolved. This could resolved by imaging the same area in short 10 - 20 minute time intervals. The cantilever

could be retracted to maintain its sharpness whilst the protein assembles, then re-approached to image after a given amount of time.

In addition, although the monomers could be seen, there were several factors which prevented optimum resolution. For example, when repeatedly imaging over the same area, it was difficult to maintain a sharp cantilever tip. Also, if a sample area did not contain a uniform patch of protein, this inevitably caused aggregates to become attached to the tip end or created a double-ended tip. However, it was found that if the tip could be gently approached on a uniform protein surface, the very first images acquired, whilst the tip is sharpest, created images of high resolution.

To further resolve the periodic monomers, several images of the surface of PLY protein rings could be measured, superimposed and averaged. A DNA trace software could then be used to do a line trace cross the surface of the protein to measure height variations. This could then be used to create a model of the periodic subunits making up the pneumolysin ring. This would require several AFM images of the protein rings surfaces in the high resolution.

Furthermore, it would be prudent to investigate how the concentration of PLY in solution affects the oligomerisation of monomers. It is possible that a high protein concentration may have been causing monomers to oligomerise into arcs/rings in solution. These pre-formed arcs would then settle onto the SLB, which would explain why the initial images of the protein obtained in this research were always in arc form. To test whether the protein concentration affects the PLY arc length, the initial stage of oligomerisation could be imaged using various concentrations of PLY. The resulting images could depict monomers individually binding to the SLB or else forming smaller arcs then that already found. These could then be imaged to observe if and how PLY grow into larger arcs and then rings over time.

Measuring lipid displacement depth within the pore

Based on the difficulties encountered in these measurements, to look further into the pore it would be sensible to use super-sharp-silicon tilt compensated tips (SSS-NCH). SSS-NCH cantilevers have tip radii between 2 - 5 nm, in comparison to the

10 nm tip radius PPP-NCH cantilevers that were used in these experiments. They are tilt compensated which will eliminate the errors caused by the asymmetry of the PPP-NCH tilted cantilevers. However, it should be noted that SSS-NCH tips are also prone to double tip affects, therefore tip-sample forces would need to be carefully controlled. In addition, the protein should be absorbed on a flat and uniform SLB to avoid edges. Arc orientation also caused inaccuracies in the measured indentation depths. Therefore, ideally, several measurements should be made on a surface abundant in protein rings.

Long term- Future work: Small cantilevers

In the near future, it would be logical to implement imaging with small cantilevers for higher imaging sensitivity. Since the interferometer is designed for the detection of small cantilevers and the frequency detector is able to detect high resonant frequencies, this would be the ideal step to enhance the resolution ability of this set-up. Since piezo-actuation involves mechanically driving the back end of the cantilever chip, it has the disadvantage of inducing several other oscillations, which obscure the thermal spectra of the cantilever. In addition the small cantilevers would be oscillated at small amplitudes (< 1 nm), therefore optical or magnetic actuation could be more suitable means of efficiently actuating them. Optical actuation has already been implemented within a similar FM AFM[2] set-up in our lab [65]. This technique involves a second laser with a wavelength different to that of the detection laser, which is focused directly on the cantilever end. The effects of bi-metallic heating is utilised to cause excitation of the cantilever. The second laser can be implemented in the set-up through the use of a wavelength multiplexer, which allows both laser wavelengths to pass to the cantilever but then splits them when they are reflected back to be measured. Magnetic actuation could also be an option for small cantilever actuation. This involves coating the cantilever with a magnetic material which can then be driven by an external AC magnetic field, produced from a current carrying coil. Since

[2]Construction of part of the lens system and fibre optics of this 2nd interferometric detector was carried out by me and my supervisor at EMPA, Materials Science & Technology, Dübendorf, Switzerland.

this can be constructed below the sample it would not require alteration of the current interferometer head. In both of these techniques, the end of the cantilever is driven directly and would reduce the spurious resonances around the cantilever resonance.

Overall, combining this FM AFM with small cantilevers has the prospects to further increase spatial resolution of biomolecules in liquid.

Bibliography

[1] C. Roduit. AFM figures. `http://www.freesbi.ch`, Creative Commons Attribution. 2010.

[2] K. D. Jandt. Atomic force microscopy of biomaterials surfaces and interfaces. *Surface Science*, 49:302–332, 2001.

[3] R. A. Wilson and Northen Kentucky University. KY 41099 H. A. Bullen, Department of Chemistry. *Introduction to Scanning Probe Microscopy. Basic Theory AFM*, 2007.

[4] D. J. Muller, D. Fotiadis, S. Scheuring, S. A. Muller, and A. Engel. Electrostatically balanced subnanometer imaging of biological specimens by atomic force microscope. *Biophysical Journal*, 76(2):1101 – 1111, 1999.

[5] S. P. Jarvis, T. Uchihashi, T. Ishida, H. Tokumoto, and Y. Nakayama. Local solvation shell measurement in water using a carbon nanotube probe. *The Journal of Physical Chemistry B*, 104(26):6091–6094, 2000.

[6] M. J. Higgin, M. Polcik, T. Fukuma, J. E. Sader, Y. Nakayama, and S. P. Jarvis. Structured water layers adjacent to biological membranes. *Biophysical Journal*, 91(7):2532–2542, 2006.

[7] T. Fukuma, K. Kobayashi, K. Matsushige, and H. Yamada. True atomic resolution in liquid by frequency-modulation atomic force microscopy. *Applied Physics Letters*, 87(3):034101, 2005.

[8] H. I. Rasool, P. R. Wilkinson, A. Z. Stieg, and J. K. Gimzewski. A low noise all-fiber interferometer for high resolution frequency modulated atomic force microscopy imaging in liquids. *Review of Scientific Instruments*, 81(2):023703, 2010.

[9] J. L. Yang, M. Despont, U. Drechsler, B. W. Hoogenboom, P. L. T. M. Frederix, S. Martin, A. Engel, P. Vettiger, and H. J. Hug. Miniaturized single-crystal silicon cantilevers for scanning force microscopy. *Applied Physics Letters*, 86(13):134101, 2005.

[10] Perkin-Elmer Instruments. What is a lock-in amplifier. `http://electron9.phys.utk.edu/optics507/modules/m10/tn1000.pdf`, 2000.

[11] atis. ATIS telecome glossary 2012. `http://www.atis.org/glossary/definition.aspx?id=2014`, 2012.

[12] Z. Khan, C. Leung, B. A. Tahir, and B. W. Hoogenboom. Digitally tunable, wide-band amplitude, phase, and frequency detection for atomic-resolution scanning force microscopy. *Review of Scientific Instruments*, 81(7):073704, 2010.

[13] B. Bircher. Interferometric detection of ultra-small cantilevers, Master Thesis. University of Basel, Switzerland, 2008.

[14] B. W. Hoogenboom, P. L. T. M. Frederix, J. L. Yang, S. Martin, Y. Pellmont, M. Steinacher, S. Zach, E. Langenbach, H. J. Heimbeck, A. Engel, and H. J. Hug. A Fabry-Perot interferometer for micrometer-sized cantilevers. *Applied Physics Letters*, 86(7):074101, 2005.

[15] T. Fukuma, K. Kobayashi, K. Matsushige, and H. Yamada. True atomic resolution in liquid by frequency-modulation atomic force microscopy. 87(3):034101, 2005.

[16] B. W. Hoogenboom, H. J. Hug, Y. Pellmont, S. Martin, P. L. T. M. Frederix, D. Fotiadis, and A. Engel. Quantitative dynamic-mode scanning force microscopy in liquid. *Applied Physics Letters*, 88(19):193109, 2006.

[17] Y. C. Tang, H. C. Chang, A. Roeben, D. Wischnewski, N. Wischnewski, M. J. Kerner, F. U Hartl, and M. Hayer-Hartl. Structural features of the GroEL-GroES nano-cage required for rapid folding of encapsulated protein. *Cell*, 125(5):903–14, 2006.

[18] S. J. Ludtke, J. Jakana, J. L. Song, D. T. Chuang, and W. Chiu. A 11.5 a single particle reconstruction of GroEL using EMAN. *Journal of Molecular Biology*, 314(2):253 – 262, 2001.

[19] J. Mou, S. Sheng, R. Ho, and Z. Shao. Chaperonins GroEL and GroES: views from atomic force microscopy. *Biophysical Journal*, 71(4):2213 – 2221, 1996.

[20] C. Leung and R. E. Palmer. Adsorption of a model protein, the GroEL chaperonin, on surfaces. *Journal of Physics: Condensed Matter*, 20(35):353001, 2008.

[21] J. Schiener, S. Witt, M. Hayer-Hartl, and R. Guckenberger. How to orient the functional GroEL-SR1 mutant for atomic force microscopy investigations. *Biochemical and Biophysical Research Communications*, 328(2):477 – 483, 2005.

[22] H. Yamada, K. Kobayashi, T. Fukuma, Y. Hirata, T. Kajita, and K. Matsushige. Molecular resolution imaging of protein molecules in liquid using frequency modulation atomic force microscopy. *Applied Physics Express*, 2(9):095007, 2009.

[23] F. Valle, J. A. DeRose, G. Dietler, M. Kawe, A. Pluckthun, and G. Semenza. AFM structural study of the molecular chaperone GroEL and its two-dimensional crystals: an ideal living calibration sample. *Ultramicroscopy*, 93(1):83 – 89, 2002.

[24] S. J. Tilley, E. V. Orlova, R. J.C. Gilbert, P. W. Andrew, and H. R. Saibil. Structural basis of pore formation by the bacterial toxin pneumolysin. *Cell*, 121(2):247 – 256, 2005.

[25] A.P. Heuck, R. K. Tweten, and A. E. Johnson. Assembly and topography of the prepore complex in cholesterol-dependent cytolysins. *Journal of Biological Chemistry*, 278(33):31218–31225, 2003.

[26] S. Seneff. Statins and myoglobin. `http://people.csail.mit.edu/seneff/statins_muscle_damage_heart_failure.html/`, Jan 2010.

[27] Encapsula NanoSciences. Plain liposomes as artificial cell models or as control. `http://www.encapsula.com/products_01.html/`, 2012.

[28] S. Boutet, L.Lomb, G. I. William, T. R. Barends, A. Aquila, R. B. Doak, U.Weierstall, D. P. DePonte, and I. Schlichting. High-resolution protein

structure determination by serial femtosecond crystallography. *Science*, 337(6092):362–364, 2012.

[29] H. Iwai and S. Z. Ger. Protein ligation applications in NMR studies of proteins. *Biotechnology and Genetic Engineering Review*, 24:129–146, 2007.

[30] G. Binnig., C. F. Quate, and Ch. Gerber. Atomic force microscope. *Phys. Rev. Lett.*, 56:930–933, Mar 1986.

[31] J. A. Stroscio and D. M. Eigler. Atomic and molecular manipulation with the scanning tunneling microscope. *Science*, 254(5036):1319–1326, 1991.

[32] D. J. Muller and A. Engel. Atomic force microscopy and spectroscopy of native membrane proteins. *Nature Protocols*, 2:2191–2197, 2007.

[33] S. Thalhammer, R. W. Stark, S. Muller, J. Wienberg, and W. M. Heckl. The atomic force microscope as a new microdissecting tool for the generation of genetic probes. *Journal of Structural Biology*, 119(2):232 – 237, 1997.

[34] R. Garcia and R. Perez. Dynamic atomic force microscopy methods. *Surface Science Reports*, 47(6-8):197–301, 2002.

[35] B. Gotsmann, C. Seidel, B. Anczykowski, and H. Fuchs. Conservative and dissipative tip-sample interaction forces probed with dynamic AFM. *Phys. Rev. B*, 60:11051–11061, Oct 1999.

[36] B. W. Hoogenboom. *Encyclopedia of Nanotechnology. AFM in Liquids.* Springer Science, 2012.

[37] S. Scheuring, D.l Levy, and J. L. Rigaud. Watching the components of photosynthetic bacterial membranes and their in situ organisation by atomic force microscopy. *Biochimica et Biophysica Acta (BBA) - Biomembranes*, 1712(2):109 – 127, 2005.

[38] J. E. Sader and S. P. Jarvis. Accurate formulas for interaction force and energy in frequency modulation force spectroscopy. *Applied Physics Letters*, 84(10):1801–1803, 2004.

[39] J. Sadar and S. P. Jarvis. Interpretation of frequency modulation atomic force microscopy in terms of fractional calculus. *Physical Review*, 70:012303, 2004.

[40] Digitial Instruments Veeco Metrology Group. *Support Note 331 Revision A: Biological Sample Preparation*, 2001.

[41] N. Starostina and P. West. *Sample Preparation for AFM Particle Characterization.* Pacific Nanotechnology Inc, Santa Clara, CA 95054, 2001.

[42] F. Ohnesorge and G. Binnig. True atomic resolution by atomic force microscopy through repulsive and attractive forces. *Science*, 260(5113):1451–1456, 1993.

[43] T. R. Albrecht, P. Grutter, D. Horne, and D. Rugar. Frequency modulation detection using high-Q cantilevers for enhanced force microscope sensitivity. *Journal of Applied Physics*, 69(2):668–673, 1991.

[44] H. Fukui, H. Onishi, and Y. Iwasawa. Atom-resolved image of the tio2 (110) surface by noncontact atomic force microscopy. *Phys. Rev. Lett.*, 79:4202–4205, Nov 1997.

[45] S. Orisaka, T. Minobe, T. Uchihashi, Y. Sugawara, and S. Morita. The atomic resolution imaging of metallic Ag(111) surface by noncontact atomic force microscope. *Applied Surface Science*, 140(3-4):243 – 246, 1999.

[46] S. Kitamura and M. Iwatsuki. Observation of 7x7 reconstructed structure on the silicon (111) surface using ultrahigh vacuum noncontact atomic force microscopy. *Japanese Journal of Applied Physics*, 34(Part 2, No. 1B):L145–L148, 1995.

[47] C. Loppacher, M. Bammerlin, M. Guggisberg, F. Battiston, R. Bennewitz, S. Rast, A. Baratoff, E. Meyer, and H.J. Guntherodt. Phase variation experiments in non-contact dynamic force microscopy using phase locked loop techniques. *Applied Surface Science*, 140(3-4):287 – 292, 1999.

[48] M. Bammerlin, R. Luthi, E. Meyer, A. Baratoff, J. Lu, M. Guggisberg, C. Loppacher, C. Gerber, and H. J. Guntherodt. Dynamic sfm with true atomic resolution on alkali halide surfaces. *Applied Physics A: Materials Science and Processing*, 66:S293–S294, 1998. 10.1007/s003390051148.

[49] K.i Fukui, H. Onishi, and Y. Iwasawa. Imaging of individual formate ions adsorbed on TiO2(110) surface by non-contact atomic force microscopy. *Chemical Physics Letters*, 280(3-4):296 – 301, 1997.

[50] F. J. Giessibl. Atomic resolution of the silicon (111) - (7x7) surface by atomic force microscopy. *Science*, 267(5194):68–71, 1995.

[51] U. Durig, H. R. Steinauer, and N. Blanc. Dynamic force microscopy by means of the phase-controlled oscillator method. *Journal of Applied Physics*, 82(8):3641–3651, 1997.

[52] S. P. Jarvis, T. Ishida, T. Uchihashi, Y. Nakayama, and H. Tokumoto. Frequency modulation detection atomic force microscopy in the liquid environment. *Applied Physics A, Materials Science and Processing*, 72:S129–S132, 2001. 10.1007/s003390100647.

[53] K. Kobayashi, H. Yamada, and K. Matsushige. Dynamic force microscopy using FM detection in various environments. *Applied Surface Science*, 188(3-4):430 – 434, 2002. Proceedings of the 4th International Conference on Noncontact Atomic Microscopy.

[54] T. Okajima, H. Sekiguchi, H. Arakawa, and A. Ikai. Self-oscillation technique for AFM in liquids. *Applied Surface Science*, 210(1-2):68 – 72, 2003. 5th International Conference on non-contact AFM in Montreal, Canada.

[55] H. Sekiguchi, T. Okajima, H. Arakawa, S. Maeda, A. Takashima, and A. Ikai. Frequency shift feedback imaging in liquid for biological molecules. *Applied Surface Science*, 210(1-2):61 – 67, 2003. 5th International Conference on non-contact AFM in Montreal, Canada.

[56] T. Fukuma, M. Kimura, K. Kobayashi, K. Matsushige, and H. Yamada. Development of low noise cantilever deflection sensor for multienvironment frequency-modulation atomic force microscopy. *Review of Scientific Instruments*, 76(5):053704, 2005.

[57] T. Fukuma. Wideband low-noise optical beam deflection sensor with photothermal excitation for liquid-environment atomic force microscopy. *Review of Scientific Instruments*, 80(2):023707, 2009.

[58] T. Fukuma and S. P. Jarvis. Development of liquid-environment frequency modulation atomic force microscope with low noise deflection sensor for cantilevers of various dimensions. *Review of Scientific Instruments*, 77(4):043701, 2006.

[59] T. Fukuma. Subnanometer-resolution frequency modulation atomic force microscopy in liquid for biological applications. *Japanese Journal of Applied Physics*, 48(8):08JA01, 2009.

[60] H.i Yamada, K. Kobayashi, T. Fukuma, Y. Hirata, T. Kajita, and K. Matsushige. Molecular resolution imaging of protein molecules in liquid using frequency modulation atomic force microscopy. *Applied Physics Express*, 2(9):095007, 2009.

[61] T. Fukuma, A. S. Mostaert, L. C. Serpell, and S. P. Jarvis. Revealing molecular-level surface structure of amyloid fibrils in liquid by means of frequency modulation atomic force microscopy. *Nanotechnology*, 19(38):384010, 2008.

[62] T. Fukuma, M. J. Higgins, and S. P. Jarvis. Direct imaging of lipid-ion network formation under physiological conditions by frequency modulation atomic force microscopy. *Phys. Rev. Lett.*, 98:106101, Mar 2007.

[63] T. Fukuma, M. J. Higgins, and S. P. Jarvis. Direct imaging of individual intrinsic hydration layers on lipid bilayers at angstrom resolution. *Biophysical Journal*, 92(10):3603 – 3609, 2007.

[64] Bart W. Hoogenboom, Kitaru Suda, Andreas Engel, and Dimitrios Fotiadis. The supramolecular assemblies of voltage-dependent anion channels in the native membrane. *Journal of Molecular Biology*, 370(2):246 – 255, 2007.

[65] C. Leung, A. Bestembayeva, R. Thorogate, J. Stinson, A. Pyne, C. Marcovich, J. Yang, U. Drechsler, M. Despont, T. Jankowski, M. Tschope, and B. W. Hoogenboom. Atomic force microscopy with nanoscale cantilevers resolves different structural conformations of the DNA double helix. *Nano Letters*, 12(7):3846–3850, 2012.

[66] S. Kawai, D. Kobayashi, S. Kitamura, S. Meguro, and H. Kawakatsu. An ultrahigh vacuum dynamic force microscope for high resonance frequency cantilevers. *Review of Scientific Instruments*, 76(8):083703, 2005.

[67] S. Nishida, D. Kobayashi, T. Sakurada, T. Nakazawa, Y. Hoshi, and H. Kawakatsu. Photothermal excitation and laser doppler velocimetry of

higher cantilever vibration modes for dynamic atomic force microscopy in liquid. *Review of Scientific Instruments*, 79(12):123703, 2008.

[68] D. Yamamoto, T. Uchihashi, N. Kodera, H. Yamashita, S. Nishikori, T. Ogura, M. Shibata, and T. Ando. High-speed atomic force microscopy techniques for observing dynamic biomolecular processes. In Nils G. Walter, editor, *Single Molecule Tools, Part B:Super-Resolution, Particle Tracking, Multiparameter, and Force Based Methods*, volume 475 of *Methods in Enzymology*, pages 541 – 564. Academic Press, 2010.

[69] T. Ando, N. Kodera, E. Takai, D. Maruyama, K. Saito, and A. Toda. A high-speed atomic force microscope for studying biological macromolecules. *Proceedings of the National Academy of Sciences*, 98(22):12468–12472, 2001.

[70] D. A. Walters, J. P. Cleveland, N. H. Thomson, P. K. Hansma, M. A. Wendman, G. Gurley, and V. Elings. Short cantilevers for atomic force microscopy. *Review of Scientific Instruments*, 67(10):3583 –3590, oct 1996.

[71] A. Chand, M. B. Viani, T. E. Schaffer, and P. K. Hansma. Microfabricated small metal cantilevers with silicon tip for atomic force microscopy. *Microelectromechanical Systems, Journal of*, 9(1):112 –116, march 2000.

[72] M. B. Viani, T. E. Schaffer, A. Chand, M. Rief, H. E. Gaub, and P. K. Hansma. Small cantilevers for force spectroscopy of single molecules. *Journal of Applied Physics*, 86(4):2258–2262, 1999.

[73] M. B. Viani, T. E. Schaffer, G. T. Paloczi, L. I. Pietrasanta, B. L. Smith, J. B. Thompson, M. Richter, M. Rief, H. E. Gaub, K. W. Plaxco, A. N. Cleland, H. G. Hansma, and P. K. Hansma. Fast imaging and fast force spectroscopy of single biopolymers with a new atomic force microscope designed for small cantilevers. *Review of Scientific Instruments*, 70(11):4300 –4303, nov 1999.

[74] M. B. Viani, L. I. Pietrasanta, J. B. Thompson, I. C. Gebeshuber, J. H. Kindt, M. Richter, H. G. Hansma, and P. K. Hansma. Probing protein-protein interactions in real time. *Nat. Struct. Bio.*, 7:644–7, Aug 2000.

[75] F. J. Giessibl. Advances in atomic force microscopy. *Rev. Mod. Phys.*, 75:949–983, Jul 2003.

[76] T. Fukuma, K. Onishi, N. Kobayashi, A. Matsuki, and H. Asakawa. Atomic-resolution imaging in liquid by frequency modulation atomic force microscopy using small cantilevers with megahertz-order resonance frequencies. *Nanotechnology*, 23(13):135706, 2012.

[77] B. Tahir. Fast frequency detection for AFM on biomolecules. Master Thesis. University College London, 2008.

[78] M. J. Higgins, C. K. Riener, T. Uchihashi, J. E. Sader, R. McKendry, and S. P. Jarvis. Frequency modulation atomic force microscopy: a dynamic measurement technique for biological systems. *Nanotechnology*, 16(3):S85, 2005.

[79] R. Best. *Phase Locked Loops: Design, Simulation, and Applications*. 6th edition. McGraw-Hill Books. New York, US, 6th edition, 2007.

[80] B. W. Hoogenboom, P. L. T. M. Frederix, D. Fotiadis, H. J. Hug, and A. Engel. Potential of interferometric cantilever detection and its application for SFM/AFM in liquids. *Nanotechnology*, 19(38):384019, 2008.

[81] D. Rugar, H. J. Mamin, and P. Guethner. Improved fiber-optic interferometer for atomic force microscopy. *Applied Physics Letters*, 55(25):2588–2590, 1989.

[82] R. R. Gruter, Z. Khan, R. Paxman, J. W. Ndieyira, B. Dueck, B. A. Bircher, J. L. Yang, U. Drechsler, M. Despont, R. A. McKendry, and B. W. Hoogenboom. Disentangling mechanical and mass effects on nanomechanical resonators. *Applied Physics Letters*, 96(2):023113, 2010.

[83] F. Ostendorf, C. Schmitz, S. Hirth, A. Kohnle, J. J. Kolodziej, and M. Reichling. How flat is an air-cleaved mica surface? *Nanotechnology*, 19(30):305705, 2008.

[84] H. Poppa and A. G. Elliot. The surface composition of mica substrates. *Surface Science*, 24(1):149 – 163, 1971.

[85] K. Muller and C.C. Chang. Electric dipoles on clean mica surfaces. *Surface Science*, 14(1):39 – 51, 1969.

[86] Ortiz Nanomechanics Laboratory@MIT F01. Procedures for imaging of standards at atomic-scale resolution using the digital instruments multimode AFM. `web.mit.edu/cortiz/www/AtomicScaleImaging.doc/`, 2012.

[87] R. Erlandsson, G. Hadziioannou, C. M. Mate, G. M. McClelland, and S. Chiang. Atomic scale friction between the muscovite mica cleavage plane and a tungsten tip. 89(8):5190–5193, 1988.

[88] M. Baba, S. Kakitani, H. Ishii, and T. Okuno. Fine atomic image of mica cleavage planes obtained with an atomic force microscope and a novel procedure for image processing. *Chemical Physics*, 221(1-2):23 – 31, 1997.

[89] T. G. Sharp, P. I. Oden, and P. R. Buseck. Lattice-scale imaging of mica and clay (001) surfaces by atomic force microscopy using net attractive forces. *Surface Science*, 284(1-2):L405 – L410, 1993.

[90] F. J. Wicks, G. S. Henderson, and G. A. Vrdoljak. Atomic and molecular scale imaging of layered and other mineral structures. *The Clay Minerals Society*, 7(4):92–138, 1994.

[91] T. Sugita and I. Yoshida. Studies of cleaved surfaces of layered semi-metals, graphite and phyllosilicates (in japanese). *J Surf Sci Soc Jpn*, (16):664–672, 1996.

[92] Y. Kuwahara. Comparison of the surface structure of the tetrahedral sheets of muscovite and phlogopite by AFM. *Physics and Chemistry of Minerals*, 28:1–8, 2001. 10.1007/s002690000126.

[93] Y. Kuwahara. Muscovite surface structure imaged by fluid contact mode AFM. *Physics and Chemistry of Minerals*, 26:198–205, 1999. 10.1007/s002690050177.

[94] T. Fukuma, J. I. Kilpatrick, and S. P. Jarvis. Phase modulation atomic force microscope with true atomic resolution. 77(12):123703, 2006.

[95] Y. Gan, W. Chu, and L. Qiao. Imaging atomically sharp crack tips in mica

by contact mode AFM under ambient conditions. *The European Physical Journal - Applied Physics*, 31(01):37–44, 2005.

[96] C. P. Green and J. E. Sader. Frequency response of cantilever beams immersed in viscous fluids near a solid surface with applications to the atomic force microscope. *Journal of Applied Physics*, 98(11):114913, 2005.

[97] D. K. Clare, D. Vasishtan, S. Stagg, J. Quispe, M. Topf G. W. Farr, A. L. Horwich, and H. R. Saibil. ATP-triggered conformational changes delineate substrate-binding and folding mechanics of the GroEL chaperonin. *Cell*, 149:113–123, 2012.

[98] A. L. Horwich, G. W. Farr, and W. A. Fenton. GroEL- GroES mediated protein folding. *Chemical Reviews*, 106(5):1917–1930, 2006.

[99] N.A. Ranson, D.K. Clare, G.W. Farr, D. Houldershaw, A.L. Horwich, and H.R. Saibil. Allosteric signalling of atp hydrolysis in GroEL-GroES complexes. *Nature Struct. Mol. Biol.*, pages 47–152, 2006.

[100] K. Braig, Z. Otwinowski, R. Hegde, D.C. Boisvert, A. Joachimiak, A. L. Horwich, and P. B. Sigler. The crystal structure of the bacterial chaperonln GroEL at 2.8 angstrom. *Nature*, 371(6498):578 – 586, 1994.

[101] R. W. Hendrix. Purification and properties of GroEL, a host protein involved in bacteriophage assembly. *Journal of Molecular Biology*, 129(3):375 – 392, 1979.

[102] N. Elad, G. W. Farr, D. K. Clare, E. V. Orlova, A. L. Horwich, and H. R. Saibil. Topologies of a substrate protein bound to the chaperonin GroEL. *Molecular Cell*, 26(3):415 – 426, 2007.

[103] E. Koculi, R. Horst, A. L Horwich, and K. Wuthrich. Nuclear magnetic resonance spectroscopy with the stringent substrate rhodanese bound to the single-ring variant sr1 of the E. coli chaperonin GroEL. *Protein Sci*, 20(8):1380 – 1386, 2011.

[104] R. Horst, E. B. Bertelsen, J. Fiaux, G. Wider, A. L. Horwich, and K. Wuthrich. Direct NMR observation of a substrate protein bound to the chaperonin GroEL. *Proc Natl Acad Sci USA*, 120(36):12748 – 12753, 2005.

[105] D. K. Clare, P.J. Bakkes, H. van Heerikhuizen, S. M. van der Vies, and H. R. Saibil. An expanded protein folding cage in the GroEL-gp31 complex. *Journal of Molecular Biology*, 358(3):905 – 911, 2006.

[106] D. K Clare, P. J. Bakkes, H. van Heerikhuizen, S. M. van der Vies, and H. R. Saibil. Chaperonin complex with a newly folded substrate protein encapsulated in the folding chamber. *Nature*, 457:107–111, 2009.

[107] N. Elad, G. W. Farr, D. Clare, E. V. Orlov, A. L. Horwich, and H. R. Saibil. Toplogies of a substrate protein bound to the chaperonin GroEL. *Mol. Cell*, 26:415–426, 2007.

[108] F. Valle, J. A. Derose, G. Dietler, M. Kawe, A. Pluckthun, and G. Semenza. Imaging the native structure of the chaperone protein GroEL without fixation using atomic force microscopy. *Journal of Microscopy*, 203(2):195 – 198, 2000.

[109] M. B. Viani, L I. Pietrasanta, J. B. Thompson, A. Chand, I. C. Gebeshuber, J. H. Kindt, M. Richter, H. G. Hansma, and P. K. Hansma. Probing protein-protein interactions in real time. *Nat. Struct. Bio*, 7(8):644 – 647, 2000.

[110] M. Yokokawa, C. Wada, T. Ando, N. Sakaki, A. Yagi, S. H Yoshimura, and K. Takeyasu. Fast-scanning atomic force microscopy reveals the ATP/ADP-dependent conformational changes of GroEL. *The EMBO Journal*, 25:4567 – 4576, 2006.

[111] T. Ando, N. Kodera, E. Takai, D. Maruyama, K. Saito, and A. Toda. A high-speed atomic force microscope for studying biological macromolecules. *Proc. Natl. Acad. Sci USA*, 98(22):12468 – 12472, 2001.

[112] H. G. Abdelhady, S. Allen, S. J. Ebbens, C. Madden, N. Patel, C. J. Roberts, and J. Zhang. Towards nanoscale metrology for biomolecular imaging by atomic force microscopy. *Nanotechnology*, 16(6):966, 2005.

[113] Veeco Instruments Inc. *Nanoscope Software 6.13 User Guide*, 2004.

[114] R. J. C. Gilbert. Pore-forming toxins. *Cellular and Molecular Life Sciences*, 59:832–844, 2002. 10.1007/s00018-002-8471-1.

[115] D. M. Czajkowsky, E. M. Hotze, Z. Shao, and R. K. Tweten. Vertical collapse of a cytolysin prepore moves its transmembrane beta-hairpins to the membrane. *EMBO J.*, 23(16):3206 – 3215, 2004.

[116] D. M Czajkowsky, Sitong Sheng, and Zhifeng Shao. Staphylococcal alpha-hemolysin can form hexamers in phospholipid bilayers. *Journal of Molecular Biology*, 276(2):325 – 330, 1998.

[117] J. Rossjohn, S. C. Feil, W. J McKinstry, R. K. Tweten, and M. W. Parker. Structure of a cholesterol-binding, thiol-activated cytolysin and a model of its membrane form. *Cell*, 89(5):685 – 692, 1997.

[118] T. X. Dang, E. M. Hotze, I. Rouiller, R. K. Tweten, and E. M.Wilson-Kubalek. Prepore to pore transition of a cholesterol-dependent cytolysin visualized by electron microscopy. *Journal of Structural Biology*, 150(1):100 – 108, 2005.

[119] A. S. Solovyova, M. Nollmann, T.J. Mitchell, and O. Byron. The solution structure and oligomerization behavior of two bacterial toxins: Pneumolysin and perfringolysin O. *Biolphysical Journal*, 87(1):540 – 552, 2004.

[120] P. J. Morgan, S. C. Hyman, O. Byron, P. W. Andrew, T. J. Mitchell, and A. J. Rowe. Modeling the bacterial protein toxin, pneumolysin, in its monomeric and oligomeric form. *Journal of Biological Chemistry*, 269(41):25315–20, 1994.

[121] P. J. Morgan, S. C. Hyman, A. J. Rowe, T. J. Mitchell, P. W. Andrew, and H. R. Saibil. Subunit organisation and symmetry of pore-forming, oligomeric pneumolysin. *FEBS Letters*, 371(1):77 – 80, 1995.

[122] R. J. C. Gilbert, J. L. Jimenez, S. Chen, I. J. Tickle, J. Rossjohn, M. Parker, P. W. Andrew, and H. R Saibil. Two structural transitions in membrane pore formation by pneumolysin, the pore-forming toxin of streptococcus pneumoniae. *Cell*, 97(5):647 – 655, 1999.

[123] S. J. Tilley and H. R. Saibil. The mechanism of pore formation by bacterial toxins. *Current Opinion in Structural Biology*, 16(2):230 – 236, 2006.

[124] I. Iacovache, M. Bischofberger, and F. Gisou van der Goot. Structure and assembly of pore-forming proteins. *Current Opinion in Structural Biology*,

20(2):241 – 246, 2010. Theory and simulation / Macromolecular assemblages.

[125] C. Lesieur, B. Vecsey-Semjen, L. Abrami, M. Fivaz, and F. Gisou van der Goot. Membrane insertion: The strategies of toxins (review). *Molecular Membrane Biology*, 14(2):45–64, 1997.

[126] J. Rossjohn, S. C. Feil, W. J. McKinstry, R. K. Tweten, and M. W. Parker. Structure of a cholesterol-binding, thiol-activated cytolysin and a model of its membrane form. *Cell*, 89(5):685 – 692, 1997.

[127] T. X. Dang, E. M. Hotze, I. Rouiller, R. K. Tweten, and E. M. Wilson-Kubalek. Prepore to pore transition of a cholesterol-dependent cytolysin visualized by electron microscopy. *Journal of Structural Biology*, 150(1):100 – 108, 2005.

[128] E. M. Hotze, E. Wilson-Kubalek, A. J. Farrand, L. Bentsen, M. W. Parker, A. E. Johnson, and R. K. Tweten. Monomer-monomer interactions propagate structural transitions necessary for pore formation by the cholesterol-dependent cytolysins. *Journal of Biological Chemistry*, 287(29):24534–24543, 2012.

[129] R. J. C. Gilbert. Pore-forming toxins. *Cellular and Molecular Life Sciences*, 59:832–844, 2002. 10.1007/s00018-002-8471-1.

[130] M. Gonzalez, M. Bischofberger, L. Pernot, F. van der Goot, and B. FrÃªche. Bacterial pore-forming toxins: The (w)hole story? *Cellular and Molecular Life Sciences*, 65:493–507, 2008. 10.1007/s00018-007-7434-y.

[131] N. Kucerka, D. Marquardt, T. A. Harroun, M. P. NieH, S. R. Wassall, and J. Katsaras. The functional significance of lipid diversity: Orientation of cholesterol in bilayers is determined by lipid species. *Journal of the American Chemical Society*, 131(45):16358–16359, 2009. PMID: 19902974.

[132] M. Nollmann, R. Gilbert, T. Mitchell, M. Sferrazza, and O. Byron. The role of cholesterol in the activity of pneumolysin, a bacterial protein toxin. *Biophysical Journal*, 86(5):3141 – 3151, 2004.

[133] A. F. P. Sonnen, A. J. Rowe, P. W. Andrew, and R. J.C. Gilbert. Oligomeri-

sation of pneumolysin on cholesterol crystals: Similarities to the behaviour of polyene antibiotics. *Toxicon*, 51(8):1554 – 1559, 2008.

[134] M. P. Mingeot-Leclercq, M. Deleq, R. Brasseur, and Y. F Dufrene. Atomic force microscopy of supported lipid bilayers. *Nature protocols*, 3:1654–1659, 2008.

[135] R. P. Richter, R. Berat, and A. R. Brisson. Formation of solid-supported lipid bilayers. an integrated view. *Langmuir*, 22(8):3497–3505, 2006. PMID: 16584220.

[136] Avanti Polar Lipids Inc. Preparation of liposomes. `http://www.avantilipids.com/index.php?option=com_content&view=article&id=1384&Itemid=372/`, 2012.

[137] X. V. Zhang, T. A. Kendall, and S. Martin. Physical structures of lipid layers on pyrite. *Environ. Sci. Technol*, 40:1511–1515, 2006.

[138] N. Gosvami, E. Parsons, C. Marcovich, M. L. Berkowitz, B. W. Hoogenboom, and S. Perkin. Resolving the structure of a model hydrophobic surface: DODAB monolayers on mica. *RSC Adv.*, 2:4181–4188, 2012.